Fabrication and Optimization of Magnetomotive Gravimetric MEMs Sensors

by

Breanna D. Cherkawski

A thesis submitted in partial fulfillment of the requirements for the degree of

Doctor of Philosophy

in

Microsystems and Nanodevices

Department of Electrical and Computer Engineering

University of Alberta

Abstract

Reducing device size in sensing technology allows for greater measurable responses, and easier integration into smaller testing environments. This work details the fabrication of high sensitivity magnetomotive gravimetric MEMS cantilevers for eventual use in gas detection. The devices are doubly clamped beams, and "U"-shaped variations of singly clamped resonant beams. When placed in a magnetic field, the current flowing through the devices generates a Lorentz force, driving the cantilevers into resonance. As analyte adsorbs to the surface of the device, the added mass will lead to a detectable shift in resonant frequency. Higher quality factor devices can be scaled down to the sub-micron scale. The dimension of the cantilever determines the resonant frequency, and cantilevers have been fabricated that range from 2.5 μm to 6.5 μm in length, but only 500 nm wide, and 174 nm thick. As size of the sensor decreases, the greater the effect adsorbed mass will have on the resonant frequency. Optimization of the fabrication process flow led to a substantial increase in yield of functional devices. Developments in vapour-phase HF etching to remove the sacrificial layer of the devices has eliminated stiction and also increased the yield. First measurements of these devices have shown resonant frequencies in expected ranges, agreeing reasonably well with mathematical modelling of both shapes of cantilever devices. This work also serves to prove the efficacy of the low-cost easy-to-use magnetomotive apparatus and balancing circuit developed by the Engineered Nanomaterials Laboratory. The configuration of these sensors, and ease of fabrication open the possibility for further func-

tionalization by other groups by using the low-cost apparatus demonstrated in this work.

I am among those who think that science has great beauty.

– Marie Curie

Acknowledgements

This journey through grad school has been an incredible one. Without the support of some very incredible people, it would not have been possible.

To my supervisor, Dr. Jeremy Sit, thank you. You saw potential in me that I didn't even know was there. Thank you for always supporting me, and creating such a great learning environment for me to grow. I will always cherish our weekly chats. Whether about where to go next with my work, or just about our weekend gardening plans, I enjoyed them thoroughly.

I would like to thank my supervisory committee Dr. Manisha Gupta and Dr. Xihua Wang for their advice and support.

Thank you to Stephanie Bozic. With your mentorship and guidance I found my passion for microfabrication and its education. Thank you for taking me under your wing.

To the nanoFAB staff who significantly helped make this project possible. Dr. Aaron Hryciw, for all your time with mask design and e-beam lithography, thank you. Thank you Scott Munro for all the hours spent around the VHF tool. Thank you Glenn Elaschuk for all your helpful advice whenever the broken things weren't working.

To the rest of the nanoFAB team, current and past: Eric, Melissa, Devin, Davor, Adam, Sofia, Gustavo, Tim, Aditi, Peng, Shiau-Yin, Shihong, Xuehai, Nas, and Nancy, thank you. Your support, kindness and dedication to maintaining and creating a lab space where a researcher like me is set up to succeed is appreciated. The time you spent with training and advising me will not be forgotten. Thank you for welcoming me into your ranks. And hopefully one day I will see my own name on the Acknowledgment page of another happy newly graduated student.

To my partner Adam, thank you. Grad school is not easy, and you supported and encouraged me the whole time to pursue my dreams. I couldn't have done it without you.

I would like to also thank the National Science and Engineering Research of Canada (NSERC) for the financial support that made this work possible.

Table of Contents

1 Introduction **1**

1.1 Gravimetric Sensors 3

1.2 Alternative Methods for Actuation 5

1.2.1 Piezoelectric Actuation and Detection 6

1.2.2 Optical Detection 7

1.2.3 Magnetomotive Actuation 7

1.3 Glancing Angle Deposition Thin Films 10

1.4 Outline 10

1.5 Impact Statement 11

2 Resonance of Devices **13**

2.1 Background 13

2.2 Euler Bernoulli Beam Theory 15

2.2.1 Doubly Clamped Beams 16

2.2.2 U-Shaped Cantilevers 17

2.2.3 Theoretical Resonance Tables 20

3 Fabrication **23**

3.1 Process Flow Background and Introduction 23

3.2 Summarized Process Flow 24

3.3 Substrate 30

3.4 Electron Beam Lithography 31

3.5 Reactive Ion Etching 40

3.6 Photolithography and Etching of Contact Pads 40

3.7 VHF Release and Process Development 45

3.8 Metalization 47
3.9 Summary 48

4 VHF Device Release Optimization 50
4.1 MEMS Device Release Background 50
4.2 VHF Release and Process Development 55

5 Device Testing and Magnetomotive Approach 74
5.1 Device Testing and Magnetomotive Setup 74
5.1.1 Network Analyzer 76
5.1.2 Balancing Circuit 77
5.1.3 Halbach Array 79
5.1.4 Chip Holder and Assembly 83
5.1.5 Vacuum Chamber 85
5.2 Operation 86

6 Results 91
6.1 Theoretical Resonances 91
6.2 Results and Plots 92
6.2.1 Doubly Clamped Cantilevers 93
6.2.2 "U" Shaped Cantilevers 98
6.3 Assumptions and Discussion 103

7 Conclusion and Future Works 108
7.1 Conclusion 108
7.2 Future Works 109
7.2.1 Further Functionalization with GLAD 110
7.2.2 Statistical Modeling 112
7.2.3 Metalization 112
7.2.4 Packaging, Scalability, and LOD 113
7.3 Concluding Remarks 114

List of Tables

2.1 Theoretical resonance of doubly clamped cantilevers 21
2.2 Theoretical resonance of "U"-shaped cantilevers 21

3.1 Electron Beam Lithography Parameters 35
3.2 Lithography Parameters 45
3.3 Process flow changes summary. Changes are highlighted in bold font. 48

4.1 Parameter Effects in VHF Processing 56
4.2 Test 1: VHF General Test 57
4.3 Test 2: VHF Pressure Test 57
4.4 Test 3: VHF Pressure Test 2 59
4.5 Test 4: VHF Water Test 65
4.6 Test 5: VHF Time Test 1 65
4.7 Test 6: VHF Time Test 2 69
4.8 Test 7: VHF Final Test 71

6.1 Measured resonances for doubly clamped cantilevers. Parameters denoted by * failed or lost the signal response shortly after testing and quality factor could not be determined. For speed of characterization Chip 2 did not have the quality factor recorded. Only the resonant frequency response was recorded. The most likely resonant mode based on the resonant frequency was included. 98

6.2 Measured resonances for the “U” shaped cantilevers. Chip 2 had a lithography error early in processing and had no resonators to test. As shown in later plots, devices from chip 1 although measurable had poor quality factors. The most likely resonant mode based on the resonant frequency was included. 99

List of Figures

1.1 Resonant frequency of an unloaded beam vs a beam loaded with a mass. The resonant frequency of the sensor is reduced by the added mass. If this frequency shift can be measured, the added mass can be mathematically determined. 4

2.1 The Lorentz force acting on a singly and doubly clamped resonator. 14

2.2 Resonance mode shapes for $n = 1$, 2, and 3 of a double clamped cantilever beam. The dotted red lines indicate the shape in resonant mode. Please note that the beam will also flex in the opposite direction as well. 17

2.3 Resonance mode shapes for n=1, n=2, and n=3 of a singly clamped cantilever beam. The dotted red lines indicate the shape in resonant mode. Please note that the beam will also flex in the opposite direction as well. 19

3.1 SEM Image of a doubly clamped MEMS cantilever 25

3.2 Process Flow Diagrams 29

3.3 Image of the .gds photomask design file showing the electrical traces that will connect the contacts with the cantilever devices. The top image shows the three square contact pads that will connect to the testing assembly. The electrical traces lead to an area highlighted by a red dotted square. The area indicated in the red square is shown in a magnified image below. In the magnified image, the final cantilever that will be separately pattered by EBL is shown with corresponding isolation trenches. The zoomed image is not to scale and proportions have been enlarged for readability. 33
3.4 Microscopy images of <5 μm long, 500 nm wide doubly-clamped cantilevers post EBL and RIE 36
3.5 Diagram of dimensions of double clamped cantilever beam. . . 37
3.6 Microscopy images of <5 μm long, 500 nm wide "U"-Shaped cantilevers post EBL and RIE 38
3.7 Diagram of dimensions of U-shaped cantilever beam. 39
3.8 Photomask designed by B. Cherkawski for the contact pads and electrical traces for cantilever MEMS of various configurations. 42
3.9 Photomask designed by B. Cherkawski. Microscope image of a single die on photomask. 43
3.10 Microscopy images of 4 μm doubly-clamped cantilevers post contact pad and trace patterning with photolithography and RIE 45
3.11 Microscopy images of 7 μm U-Shaped Cantilevers post contact pad and trace patterning with photolithography and RIE . . . 46

4.1 Carbon Dioxide Pressure-Temperature Phase Diagram Adapted from [1] and [2]. 53
4.2 Microscopy image of chip C.1. Severe contamination visible on the chip after VHF etching, not present before. Chip was piranha cleaned immediately before processing, meaning the residue was unlikely to be organic. 58

4.3 Microscopy image of chip C.4. Severe contamination visible on the chip after VHF etching, not present before. Chip was piranha cleaned immediately before processing, meaning the residue was unlikely to be organic. Compared to chip C.1, the residue on chip C.4 was reduced by lowering the pressure in the system during the etch. 60
4.4 SEM image of Chip C.4, VHF etched at 11 Torr, for 200 s, severe contamination observed over the surface of the chip. Limited charging of the residue on the surface of the chip could be indicative of a inorganic residue on the surface. 61
4.5 SEM image of Chip C.5, VHF etched at 10.5 Torr, for 200 s, reduced contamination observed compared to chips etched at 13 Torr, but not eliminated 62
4.6 SEM images comparing contamination during VHF tests performed at 10.5 Torr. Reduced contamination observed, but not eliminated at 10.5 Torr when compared to higher pressures. No appreciable difference in contamination between the two chips despite the difference in etch time. Magnification is shown as different between the two figures to demonstrate scale of residue. 63
4.7 SEM images comparing contamination during VHF tests performed at 10 Torr. Reduced contamination observed at 10 Torr compared to 10.5 Torr. No appreciable difference in contamination between the two chips despite the increase in etch time. 64
4.8 SEM image of Chip C.15, VHF etched at 10 Torr, for 175 s, 8 mgpm H_2O, contamination eliminated. 66
4.9 SEM image of Chip C.16, VHF etched at 10 Torr, for 175 s, 8 mgpm H_2O, approximate etch depth: 199 nm 67
4.10 SEM image of Chip C.17, VHF etched at 10 Torr, for 500 s, 8 mgpm H_2O, approximate etch depth: 217 nm. 68
4.11 Chip C.20, VHF etched at 10 Torr, for 1400 s, 8 mgpm H_2O, approximate etch depth: 490 nm. 70

4.12 Chip C.24, VHF etched at 10 Torr, for 1350 s, 8 mgpm H_2O, approximate etch depth: 479 nm. 72
4.13 Chip A.3, VHF etched to a comparable amount to C test chips. 73

5.1 Photograph of the entire testing assembly including vacuum chamber, network analyzer and balancing circuit. 75
5.2 Diagram showing the set up with the balancing circuit, network analyzer and on-chip bridge. 76
5.3 Balancing circuit as developed by the ENL group [3]. Each branch of the signal from the hybrid splitter enters the balancing circuit from the cables at the top of the diagram. From there, the signal passes through two mirrored phase and amplitude branches for manual balancing. The signal then exits the circuit through the two cables at the bottom of the diagram (labeled in purple) to be passed through the device. 78
5.4 A diagram depicting the signal recombination through the two branches of device. Anti-phase drive signals are introduced at the input ports, which should theoretically cancel each other out before reaching the output port. However, mismatch in the signal unavoidable in real world application leads to a detectable signal on the output port. 79
5.5 Diagram of Halbach array orientation of NdFeB magnets used during testing. The black arrows indicate the magnetic field direction for each magnet. The red arrow indicated the overall produced 1 T magnetic field in the center of the assembly. . . 81
5.6 Photograph of Halbach array implemented in vacuum chamber. The black arrows indicate the magnetic field direction for each magnet. The overlaid red arrow indicates the overall direction of the magnetic field. 83
5.7 Pin assembly to connect contact pads to circuit. For eight devices, a total of 24 connections are required, leaving one pin unused. 84

5.8 Chip holder used to connect to pins assembly that will be placed inside the Halbach array. A completed chip is shown inside the holder. 85
5.9 Plot of the response from the system with the balancing circuit not in use. 88
5.10 Plot of the response from the system with the balancing circuit balanced to 110 MHz. 88
5.11 Plot of a 4 μm long doubly clamped cantilever with a resonant response at 127 MHz. The device was measured both with and without the use of the balancing circuit, and the results were combined in this plot. 89
5.12 Plot of how the values were extracted from the resonance plot to determine quality factor. 90

6.1 Theoretical resonant frequencies of doubly clamped cantilevers of varying lengths at n=1, n=2, and n=3 92
6.2 Theoretical resonant frequencies of "U" shaped cantilevers of varying lengths at n=1, n=2, and n=3 92
6.3 Plot showing the resonance of a 3.5 μm long doubly clamped cantilever from chip 1 94
6.4 Plot showing the resonance of a 4 μm long doubly clamped cantilever from chip 1 95
6.5 Plot showing the resonance of a 5 μm long doubly clamped cantilever from chip 1 95
6.6 SEM image showing a 3.5 μm long doubly clamped cantilever from chip 2 96
6.7 SEM image showing a 5.5 μm long doubly clamped cantilever from chip 2 97
6.8 Plot showing the resonance of a 4.5 μm long "U" shaped cantilever from chip 1 100
6.9 Plot showing the resonance of a 6 μm long "U" shaped cantilever from chip 1 100

6.10 Plot showing the resonance of a 3 μm long "U" shaped cantilever from chip 3 101
6.11 Plot showing the resonance of a 3.5 μm long "U" shaped cantilever from chip 3 101
6.12 Plot showing the resonance of a 4 μm long "U" shaped cantilever from chip 3 102
6.13 SEM image showing a 3 μm long "U" shaped cantilever from chip 3 102
6.14 Plot showing the resonance of a 4 μm long "U" shaped cantilever from chip 3 103
6.15 Thickness variance of 10 nm in the theoretical frequency of the doubly clamped cantilevers. 104
6.16 Thickness variance of 10 nm in the theoretical frequency of the "U"-shaped cantilevers. 105
6.17 Length variance due to undercut of 0.5 μm in the theoretical frequency of the doubly clamped cantilevers. 106
6.18 Length variance due to undercut of 1 μm in the theoretical frequency of the doubly clamped cantilevers. 107
6.19 Length variance due to undercut of 0.5 μm in the theoretical frequency of the "U" shaped cantilevers. 107

7.1 A diagram depicting the initial nucleation stage of a GLAD film and the subsequent self-shadowing. 110
7.2 A diagram depicting the final structure of a GLAD film. . . . 111

Chapter 1

Introduction

Over the past 30 years, microfabrication and nanotechnology has seen a massive boom in innovation. Being able to scale down electronics has allowed engineers to fit more devices onto a single chip, allowing greater processing power and better energy efficiency. Many of our modern electronics are complex systems composed of many micro- and nano-devices. It is easy to take for granted the amount of innovation and technology that goes into the devices we have with us all day long. Although seemingly static, some of our devices, like cellphones have small parts that move that allow for interacting with the environment around them, familiar examples being speakers and microphones. Micro-electro-mechanical systems (MEMS) are devices on the micro-scale that either move mechanically due to an electrical input, or generate an electronic signal with mechanical force. In simpler terms: MEMS are an electric system that moves, and is smaller than 100 µm square.

Being able to generate a signal with an external stimulus opens up the ability to integrate sensors into devices. Optimization and application of MEMS is key to modern electronic devices. From accelerometers in cell phones, to emergency shut-off detectors in petrochemical plants, MEMS have a wide variety of uses. The smaller of MEMS that can be manufactured allows for easier integration into existing systems. As well, scaling down MEMS increases sensitivity to more minute stimulus.

The focus of this research is the optimization and functionalization of MEMS for application in gas sensing. Being able to detect minute concen-

trations of dangerous gases would be of great benefit to the safety of people working with these chemicals. As well, minute concentrations of other analyte molecules could be applied to other scientific applications; for example, medical testing. The challenge of manufacturing devices on the nano-scale is not a simple task. Unlike macro-scale-machining, we cannot see the devices we are trying to manufacture with the naked eye. In addition, there are few tools that are able to create the desired micro-devices in a direct manner. Practical micromachining involves building devices with a top-down approach, depositing thin layers of material on a substrate, and removing certain areas of that material in order to form the desired structure by pattern transfer. This cycle is repeated until a multi-layered functional device is created.

Engineers have created a variety of techniques to achieve these micro-devices, an example being photolithography; A viscous polymer with a photoactive compound (photoresist) is spun onto the surface of a substrate and baked to set it. When a high intensity light source is shone onto the surface either through a patterned mask, or through direct writing such as with a laser, the photoactive compound is activated. A developer will wash away either the exposed or unexposed areas (depending on the properties of the photoresist) to reveal the pattern from the light exposure. A positive tone resist will become more soluble in developer after exposure to specific wavelengths of light. A negative tone resist will become less soluble after exposure. These now-patterned areas can be used to protect the underlying film from etching, generally either by chemical or physical means, allowing a micro- or nano- patterned material layer in the desired shapes and configuration. [4].

The ENL group focuses on the development of magnetomotive, functionalizable, MEMS gravimetric sensors. These resonant MEMS cantilever devices show promise for use in low-pressure gas-sensing applications [5]. These sensors are placed in a strong magnetic field generated by permanent magnets and are driven into resonance by running a current through them. When material adsorbs to the surface of the resonator, the added mass leads to a detectable shift in the resonant frequency.

By increasing the surface area of the resonator, there will be greater mass-

loading of adsorbed analytes, improving their mass sensitivity. This can be done through design or through functionalization. Mass sensitivity is also improved by scaling down these sensors to the nano-scale. The molecules that one may be hoping to detect should be of a static size. A large resonator will be affected less than a smaller resonator by the same sized particle. As we cannot make the molecules larger, the practical way to improve the sensitivity is to scale down the resonator. The closer in overall mass of the analyte and they sensor, the higher the sensitivity of the sensor. Essentially: the smaller the sensor, the greater the effect an adsorbed mass will have on the resonant frequency [6]. This will be discussed further in Chapter 2.

This research will be beneficial to other researchers who hope to expand sensitivity of gas sensors in many different applications. By fitting experimental results for the resonance of different configurations and sizes of cantilevers to theoretical modeling for these devices, it is hoped to provide a strong foundation for other researchers to adapt these resonators for more specialized applications. The success of the system proposed in this thesis work is hoped to provide a good starting point to other researchers.

1.1 Gravimetric Sensors

Development in sensor technology in the past several years has provided advancements in a variety of fields. Sensors for detection of dangerous gases e.g. H_2S [7] has improved safety for workers who may be exposed to these chemicals. Advancements in the functionalization of sensors allows for precise detection of certain molecules for medical applications [8]. During the global COVID-19 pandemic, the benefits of detection technology have been brought to greater public awareness. Working to improve the limit of detection (LOD) and sensitivity across a diversity of sensing applications will be beneficial to research and development and eventually end users. This section will specifically focus on gravimetric sensors. These sensors are often cantilevers or nano-wires that undergo a downshift in their resonant frequency due to an adsorbed mass. The amount of mass with respect to the size (and mass) of the cantilever will have

a greater effect on the resonant frequency. If we compare two cantilevers, the smaller cantilever will be more greatly frequency shifted by the same amount of analyte mass. The smaller in overall mass that a sensor is, the smaller amount of analyte mass that can be ultimately detected.

Once the beam has been deflected past its equilibrium point, according to Newton's third law a force is created in the opposite direction. This restoring force drives the resonator to attempt to return to its equilibrium point. However, as the cantilever moves to return to equilibrium its momentum causes it to continue moving past equilibrium. This will continue in both directions until all kinetic energy is lost. The energy can be lost through air damping, thermoelastic damping, clamping losses, or losses due to device defects [9]. This concept is demonstrated in Fig. 1.1. Energy losses in a system occur in a multitude of ways. Some examples of energy losses include, but are not limited to heat or friction. However, when constantly driven with an applied force of sufficient magnitude, the beam will continue to resonate. Further explanation of the resonance of cantilevers based on the Euler Bernoulli Beam Theory is discussed further in Chapter 2.

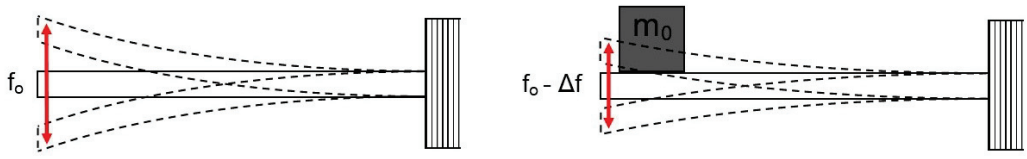

Figure 1.1: Resonant frequency of an unloaded beam vs a beam loaded with a mass. The resonant frequency of the sensor is reduced by the added mass. If this frequency shift can be measured, the added mass can be mathematically determined.

An example of a widely adopted mass-loading sensor would be a quartz crystal microbalance (QCM), used to monitor thin film growth during physical vapor deposition (PVD) [10]. As film grows on the surface of the QCM, adding mass to the sensor, there is a shift in the resonant frequency, allowing for approximation of the thickness of the growing thin film. Although practical for the measurement on the scale of nanograms, further fine-tuning for lower LOD is desirable for gas detection (as a monolayer of adsorbed gas molecules weighs substantially less than several nm of solid film material).

1.2 Alternative Methods for Actuation

Gravimetric sensor technology has several different strategies and techniques that have been shown successful in literature. One needs a way to not only drive the sensors into resonance, but also a way to measure the shift in resonant frequency due to the added mass. Three common techniques have been observed for driving and sensing these types of MEMS/NEMS. Piezoelectric actuation and measurement is currently one of the most common techniques [10–12]. Magnetomotive actuation can be used to drive the sensors into resonance, with balancing techniques used to electrically measure the change in resonant frequency [9–11, 13]. Other researchers have opted to use piezoelectric means to drive the sensors into resonance, but measure the changes optically [10, 11, 14]. In early work [9], it was shown that doubly clamped NEMS SiC nanowires can have a sensitivity down to 2.5 x 10 $^{-18}$ g. All of these devices are capable of operating in the mega- to gigahertz range for their resonant frequency (which is determined by device size and mass). However, this high-sensitivity precision work has primarily been performed under vacuum, to reduce air-damping effects. All three of the mentioned methods required constant sampling, dynamic sampling, to measure ongoing shifts in resonant frequency. These sampling methods means that data must be collected in real-time, with new data points constantly being collected and analyzed.

1.2.1 Piezoelectric Actuation and Detection

A piezoelectric material contains asymmetrically oriented positive and negative ions within its crystal lattice [10]. When strained due to an applied stress, electric dipoles are created, leading to a surface charge, which generates a small electric field; measurable as a voltage difference [10]. The inverse is also applicable, where an applied electric field, (or rather a voltage) to a piezoelectric material causes a deformation. Common piezoelectric materials include but are not limited to: lead zirconate-titanate (PZT), zinc oxide, and quartz [10, 15]. The ability to integrate both the driving force for the device and measurement onto the chip level is a huge advantage for device scaling. Piezoelectric actuation can be done on the chip itself, or outside in a driving assembly [14, 16, 17]. A problem observed with piezoelectric methods is that piezoelectric devices have an intrinsically high resistance, which can range from 5 - 100 kΩ [18]. This high resistance can behave as a low-pass filter (LPF), swamping out smaller signals, limiting the practical range over which these devices can be used [18]. High resistances in the circuit have the potential to increase thermal noise, also swamping out smaller signals and reducing device quality factors [13, 18]. If operating near the LPF cutoff frequency, there is a chance valuable data could be lost. It should also be considered that the addition of any additional material to the resonator (such as the piezoelectric thin film), will affect the mass, which will affect the resonant frequency of the device.

The LOD of piezoelectric gravimetric sensors is on the scale of 10^{-19}g, with quality factors ranging from the 100's to 1000's [9,11,16,17,19]. One technique that has improved the limit of detection of these piezoelectric devices is large NEMS arrays [20]. By increasing the number of cantilevers, the testing surface area increases dramatically. These devices are run in parallel in grids of several dozen, to over 1000. In some cases, each grid will contain devices of different sizes (which correlates to a specific resonant frequency) [19]. The responses of these devices are then averaged to give a more robust sensor response. Some groups have reported down to a 10 ppb measurement with these large arrays.

Reducing draw power of these sensors is currently in progress [19].

1.2.2 Optical Detection

Optical detection of displacement has been used extensively in these cantilever-type devices. Often driven by piezoelectric means, the shift in resonant frequency is measured optically, such as by laser interferometry. Optical measurements can be used both for measuring the resonant frequency of an oscillating cantilever, but also for direct measurement of gases themselves. Non-dispersive infrared (NDIR) sensors are capable of measuring carbon dioxide down concentrations in air down to several thousand ppb [11,21]; however, these sensors suffer for accuracy and are often limited to only measuring select gases, such as carbon dioxide [22]. One drawback of optical detection is the system scalability and integration into smaller testing environments [11]. The smaller the testing environment, the more practical it is for integration into existing systems. Optical measurement systems, although reliable, and accessible, cannot as easily be scaled down into smaller systems, especially since the measurement optics are out of the plane of the substrate. This problem has commonly been solved by also using electrical means such as balancing to measure the shift in resonant frequency instead of measuring cantilever displacement with a laser [3, 13, 16, 17]. This being said, optical measurement is still a fairly accessible way for researchers to measure the displacement of their devices.

1.2.3 Magnetomotive Actuation

A magnetomotive approach to driving cantilevers into resonance relies on exploiting Lorentz force. When a device with a running current is placed in a magnetic field, it experiences a force whose magnitude can be engineered. The electromagnetic force experienced by a charged particle in a magnetic field is given by the following equation:

$$\vec{F} = q(\vec{v} \times \vec{B}) \tag{1.1}$$

Where F is the force experienced by the test charge [N], q is the charge of

the particle [C], v is the velocity of the particle [m/s] and B is the magnetic field [T]. Although the particle will continue to move in the direction of the electric field, the magnetic field generates a force perpendicular to the motion of the particle. When current is flowed through a cantilever perpendicular to a magnetic field, the Lorentz force will cause the beam to deflect.

In addition to the low-cost of the assembly compared to electromagnetic assemblies, once a magnetomotive measurement system has been implemented in a lab, testing of the devices becomes relatively low cost, and low effort as the permanent magnets require very little maintenance [5]. A permanent magnetic assembly also requires no additional power to run, unlike power-hungry electromagnets [5]. A researcher could develop dozens of chips, and characterize them, with little cost for the volume of characterization, aiding device development. To scale to a smaller magnetic assembly, with a smaller magnetic field, the researcher would need to increase the current running through the devices to achieve a similar magnitude response. This however, has practical limitations, as high currents will lead to heating of the device, wires, and any balancing circuitry [5, 10]. Force scales proportionally with magnetic field strength and current, so decreasing to a smaller area with, say, half the magnetic field, would mean that the system would need to be able to handle double the current flow through the devices. By scaling down the system it will be easier to integrate with other systems and technologies.

A key advantage of this technique is the ability to both drive and measure the resonance of the devices through the same port. This allows for the potential to scale the overall system down, allowing for more diversity in applications. The ability for a researcher to easily access a low-cost magnetic assembly allows for further research into both lowering the LOD and the functionalization of devices. Being able to detect single molecules is the pinnacle of sensing; however, the ability to sense a specific analyte has endless possibilities. Every field, from chemistry to biology, would benefit from expanded research into functionalized devices for specific sensing applications. The work of the ENL hopes to lay a foundation for lower-cost analyte-specific sensing, eventually including functionalized sensor arrays that could measure combinations

of different analytes.

Currently, there are several groups working on NEMS for mass spectroscopy. During ion spectroscopy, once a sample is ionized, the spectrum is analyzed based on the charge-to-mass ratio of the sample. The use of gravimetric NEMS means that the sample does not need to be charged in order to be measured, allowing for measurement of neutral samples. This opens the possibility for much more precise measurements, as in ion spectroscopy only one out of thousands of ions generated are detected. Sage *et al.* were able to measure neutral generated particle clusters from 70 KDa to 500 KDa [23]. This is down to only 1.2 x 10^{-19} g, substantially smaller than other reported values [9, 13]. This single-particle sensing ability (albeit large particle) has great potential for sensing applications.

Another technique observed is performing testing in liquid environments for biochemical analysis [24]. Although expanding on the different potential analytes for testing, the additional damping of water lowers the quality factor of devices, increasing noise, and increasing error. Work is being done to improve the LOD and quality factor of these devices. However, this unavoidable loss is necessary for researchers attempting to measure biological samples, which could be compromised in dry conditions. In Yu *et al.* improvements were made to improve LOD of aqueous measurements to 500 ppb of Hg^{2+} ions [24]. Although an improvement on aqueous testing, this is still several orders of magnitude higher than other gas sensing approaches. This group was also able to compare their devices in air and in liquid, and measured quality factors of 10048 and 246 respectively [24].

In other examples in literature, it has been shown that reducing the temperature of a resonator has a positive effect on the adsorption of analyte to the surface of the resonator, as well as increasing the quality factor of devices [9,13]. In Presnov *et al.* they were able to achieve quality factors of 36500 at 20 mK for their magnetomotive SiC nanowires. The mass sensitivity was measured down to 6 x 10^{-21} $gHz^{-1/2}$ [13]. Interestingly, it was also found that lower magnetic fields (under 5 T) increased quality factors of devices. This largely was attributed to non-linearities in magnetic fields above 3.5 T [13]. However,

this technique is not as practical if the driving and cooling system for these resonators is to be scaled down, or made portable.

1.3 Glancing Angle Deposition Thin Films

In future work it is the hope for these devices to be coated with highly porous GLAD (glancing angle deposition) films. GLAD films are films are columnar, and increase the surface area greatly due to the amount of columnar structures deposited. These films are formed due to inherent shadowing from nucleated areas shadowing other areas of the directional flux generated during certain thin film deposition techniques. As the film continues to grow, the nucleated areas grow into columns, whereas the shadowed areas do not. These columns are very thin, and highly dense once formed. The surface area of each individual column will add to the overall surface area of the device [8, 14, 25, 26]. This would be another possible way to lower the LOD for these devices. Research has been conducted into depositing these films onto cantilevers, but limited research exists for using them for gas detection in a magnetomotive approach [14]. This will be discussed further in Chapter 7.

1.4 Outline

The remainder of this work is organized as follows. In Chapter 2 the behaviour of cantilever devices will be analyzed. Theoretical calculations were performed to determine the expected frequency response for two configurations of cantilever (singly and doubly clamped). Determining what sizes of cantilever will deliver a response in a measurable range is critical before fabricating devices.

Chapter 3 outlines the process flow used to fabricate the cantilever devices. Work was done to optimize the final yield by changing process steps. Chapter 4 shows the design of experiment for implementing vapor phase HF (VHF) release of devices. Low yield was attributed to the release step for the devices in earlier work, showing a need to improve on device release. This work was successful in the development of a recipe for MEMS device release.

Chapter 5 shows the magnetomotive assembly and balancing circuit used

by the ENL lab for device actuation and measurement. In Chapter 6 the frequency response of the cantilever devices was found. Yield was substantially improved from previous work. Overall, the efficacy of the labs system was shown. Changes to the overall device fabrication that increased yield serves to help other researchers making similar devices as a starting point.

Conclusions and future works and later research to be done is discussed in Chapter 7.

1.5 Impact Statement

Once a magnetomotive assembly (see also Section 5.1) has been implemented, as in the ENL, testing of the devices becomes relatively low cost. A researcher could fabricate dozens of chips, and characterize them, with little cost for the volume of characterization, aiding device development. Various device configurations can be tested easily. To scale to a smaller magnetic assembly, which generally means a weaker magnetic field, one would need to compensate with an increased drive current to achieve a similar frequency response. This however, has practical limitations, as high currents will lead to heating of the device, wires, and associated circuitry of the system [5, 10]. In our case, the heating will also affect the balancing circuit that will be detailed in later chapters.

Force scales proportionally with magnetic field and current, meaning that for a smaller system with half the magnetic field, the system would need to be able to handle double the current. By scaling down the system it will be easier to integrate with other systems and technologies. The expected impact of this work is to show the efficacy and practicality of our low-cost magnetomotive system as a benefit to other researchers working in NEMS sensing applications. These researchers will then be able to implement this into their labs and testing of their own magnetomotive sensor devices. Combined with the balancing circuit developed by our lab, we are hoping to prove the ease and reliability of our low cost magnetomotive assembly. This low cost set-up will allow smaller labs, which may have access to less funding, to enter research into improving

and lowering the limit of detection of gravimetric MEMS and NEMS. With trends towards further functionalization, and specific analyte testing, lowering the financial bar for entry to other capable and creative groups will only add immensely to global scientific knowledge in this field.

Chapter 2

Resonance of Devices

Determining the behaviour of resonator devices, and knowing where in the frequency spectrum to expect a response is critical in choosing device dimensions and configurations. The size and shape of the devices will determine the fundamental resonant frequency. This frequency needs to fall into a detectable range by the system used in order to have value as a sensor device. In elementary beam theory, beams can be singly or doubly clamped cantilevers, which will form the basis of this analysis. Using these principles, the resonant frequency of the beams can be calculated. Knowing the theoretical resonance of a beam will inform later design decisions on dimensions and configurations.

2.1 Background

To reliably predict the resonance of the manufactured cantilever structures, the theoretical resonant frequency needs to be calculated. For a resonator beam, it is known that:

$$\omega_0 = \sqrt{\frac{k}{m}},\ f = \frac{\omega_0}{2\pi} \tag{2.1}$$

Where ω_0 is the undamped natural frequency [rad/s], k is the effective stiffness of the system [N/m], and m is the effective mass [kg] [6]. The frequency f_0, is in [Hz]. By reducing the mass of a beam, the resonant frequency of the device should increase. Mass adsorption from molecules will have an effect on the resonant frequency. Analyte molecules adsorbing to the surface of the resonator increases the resonator's effective mass. The smaller the mass of the

resonator, the larger of a difference an added mass will have in proportion. Continuing, the Lorentz force of a moving electric charge through a magnetic field is:

$$\vec{F} = q(\vec{E} + \vec{v} \times \vec{B}) \tag{2.2}$$

Where F is force [N], q is elementary charge [C], v is the velocity of the charged particle [m/s] and B is the magnetic field [T]. A doubly clamped beam will form a complete circuit, allowing current to flow. However, for a singly clamped cantilever to form a complete circuit, it needs to form a "U" shape. If the current flows in through one branch of the "U" and out the other, a complete circuit can be made. The force will only act on the connecting portion of the "U" shape. This is demonstrated in Fig. 2.1. As the devices themselves are proportionally much smaller than the external magnetic field, it is assumed that the magnetic field will be uniform across a device.

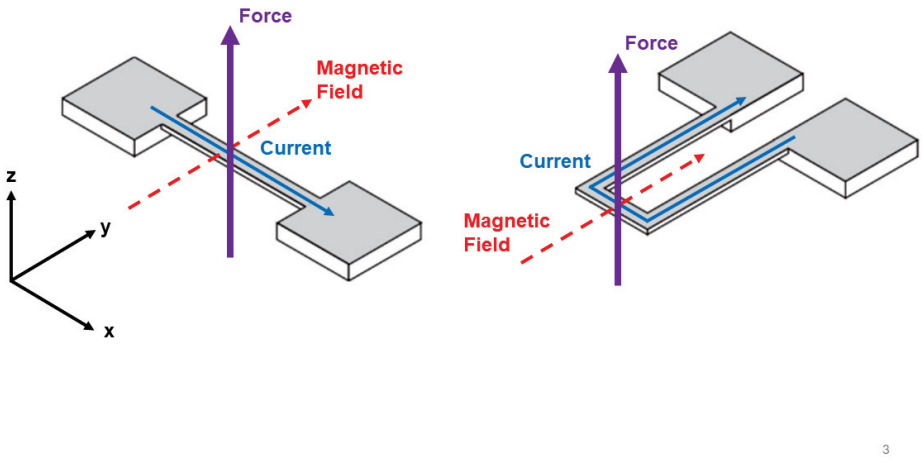

Figure 2.1: The Lorentz force acting on a singly and doubly clamped resonator.

The devices will initially be tested under vacuum. Because of this, it is assumed that due to the low pressure in the system, that the resonators behave underdamped [5,11]. This will simplify initial calculations. The quality factor Q is used to define the degree of damping and energy lost per cycle to determine the quality of the sensors. Q may be extracted from a frequency

plot using the following equation (Eq. 2.3). The sharper the peak, the greater the quality factor of the resonator. Various effects will cause a decrease in the Q factor of a resonator. Thermoelastic damping, electrical losses due to parasitic capacitances, thin film stresses from the metalization layer and clamping losses, will all contribute to a reduced Q [5, 10, 11]. Some of these losses are unavoidable, and some can be reduced.

$$Q = \frac{f_{res}}{\Delta f} \tag{2.3}$$

Some further assumptions made during this beam resonance analysis include:

- Mass and stiffness are constant throughout the beam.
- Any deformations are small with respect to the size of the beam.
- The beam behaves in a linear elastic isotropic fashion.
- Any effects from the Poisson's ratio are ignored.
- Any plane sections that are perpendicular to the neutral axis before deformation occurs, will remain perpendicular and plane after deformation.

2.2 Euler Bernoulli Beam Theory

The Dynamic Beam Equation, also referred to as the Euler Bernoulli beam theory, forms the basis of this analysis [6, 27]. The culmination of which is shown below in Eq. 5.

$$\frac{d^2}{dx^2}\left[E(x)I(x)\frac{d^2w(x,t)}{dx^2}\right] = p(x,t) - \rho(x)\Omega(x)\frac{d^2w(x,t)}{dt^2} \tag{2.4}$$

Where $p(x)$ is the applied force, $E(x)$ is the young's modulus, $I(x)$ is the moment of inertia, $w(x,t)$ is the displacement, ρ(x) is the curvature of the beam, and Ω(x) is the cross sectional area. As stated above, it is assumed that E, I and Ω are constant. It is also assumed that the beam undergoes free vibration, meaning $p(x,t) = 0$. This yields the following simplification:

$$\frac{d^2}{dx^2}\left[EI\frac{d^2w(x,t)}{dx^2}\right] = -\rho\Omega(x)\frac{d^2w(x,t)}{dt^2} \tag{2.5}$$

2.2.1 Doubly Clamped Beams

This analysis will begin with the mathematical modeling of a doubly clamped cantilever beam. In order to solve, variables must be separated in order to obtain several ordinary differential equations (ODE's). For further ease of calculation the substitute: $w(x,t) = X(x)T(t)$, as a function of x and t was made.

$$\frac{d^2}{dx^2}\left[EI\frac{d^2X(x)}{dx^2}\right] = -\omega^2\rho\Omega X(x) = 0 \tag{2.6}$$

$$\frac{d^2T(t)}{dt^2} + \omega^2 T(t) = 0 \tag{2.7}$$

The general solution for Eq. 2.5 is:

$$T(t) = Acos(\omega t) + Bsin(\omega t) \tag{2.8}$$

Next, boundary conditions are applied. For a doubly clamped beam, which would be clamped at x=0 and x=L,

$$\omega(0,t) = 0 \qquad \frac{\partial\omega}{\partial x}(0,t) = 0 \tag{2.9}$$

$$\omega(L,t) = 0 \qquad \frac{\partial\omega}{\partial x}(L,t) = 0$$

yielding a solution of:

$$cos(\lambda_n)cosh(\lambda_n) = 1 \tag{2.10}$$

where the eigenvalues, λ_n, for each harmonic mode can be determined by:

$$\lambda_n = \pi\frac{2n+1}{2} \tag{2.11}$$

These calculations can be extrapolated to approximate the shapes of the different resonance modes, shown in Fig. 2.2 [6]. It should be noted that generally lower resonance modes have less noise compared to higher resonance modes [5,6]. As complexity of motion increases, and overall maximum amplitude for each section decreases, there is the potential for increased noise in the measured signal response.

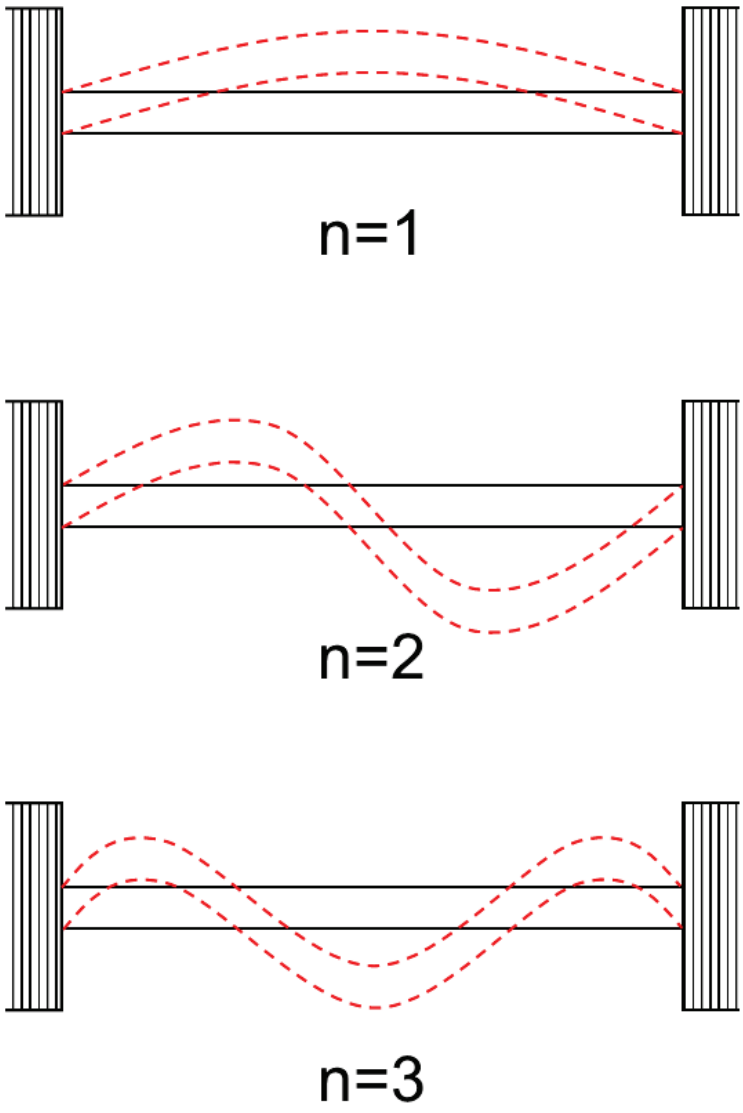

Figure 2.2: Resonance mode shapes for $n = 1$, 2, and 3 of a double clamped cantilever beam. The dotted red lines indicate the shape in resonant mode. Please note that the beam will also flex in the opposite direction as well.

2.2.2 U-Shaped Cantilevers

Another scenario to consider is a singly clamped cantilever. It is desirable to maximize the surface area available to analyte to adsorb to the surface. By configuring the devices as "U"-shaped cantilevers, the relative surface area of the devices can be increased while still largely approximating them as simpler

singly clamped cantilevers. This section will detail this calculation.

When modeling the "U"-shaped cantilevers, they will be treated as two singly clamped cantilevers; calculating the resonant frequency about the x-axis. This yields the following boundary conditions, as the beam is clamped on only one side:

$$\omega(0,t) = 0 \qquad \frac{\partial \omega}{\partial x}(0,t) = 0 \tag{2.12}$$
$$\frac{\partial^2 \omega}{\partial x^2}(L,t) = 0 \qquad \frac{\partial^3 \omega^3}{\partial x^3}(L,t) = 0$$

yielding a solution of:

$$cos(\lambda_n)cosh(\lambda_n) = -1 \tag{2.13}$$

also giving the eigenvalues for the "U"-shaped cantilever:

$$\lambda_n = \pi \frac{2n-1}{2} \tag{2.14}$$

Both beams, regardless of orientation, are rectangular in cross-section. Some literature approximates the beams as a wire, allowing for beam width and cross sectional area to be neglected from the calculations [6]. However, in this case, beam width is substantially larger than the thickness of the beam, meaning moment of inertia and cross sectional area must be included in the calculation of resonant frequency.

$$\omega_n = \left[\frac{\lambda_n}{L}\right]^2 \sqrt{\frac{EI}{\rho A}} \tag{2.15}$$

Young's modulus, E, of Si is 165 GPa [15]. In this equation, I is the moment of inertia about the x-axis for a rectangular cross section, A is the cross sectional area, and ρ is the density of Silicon.

$$f = \frac{1}{2\pi}\left[\frac{\lambda_n}{L}\right]^2 \sqrt{\frac{EI}{\rho A}} \tag{2.16}$$

These calculations can be extrapolated to approximate the shapes of different resonance modes, shown in Fig. 2.3 [6]. Again, it should be noted that

generally lower resonance modes have less noise compared to higher resonance modes.

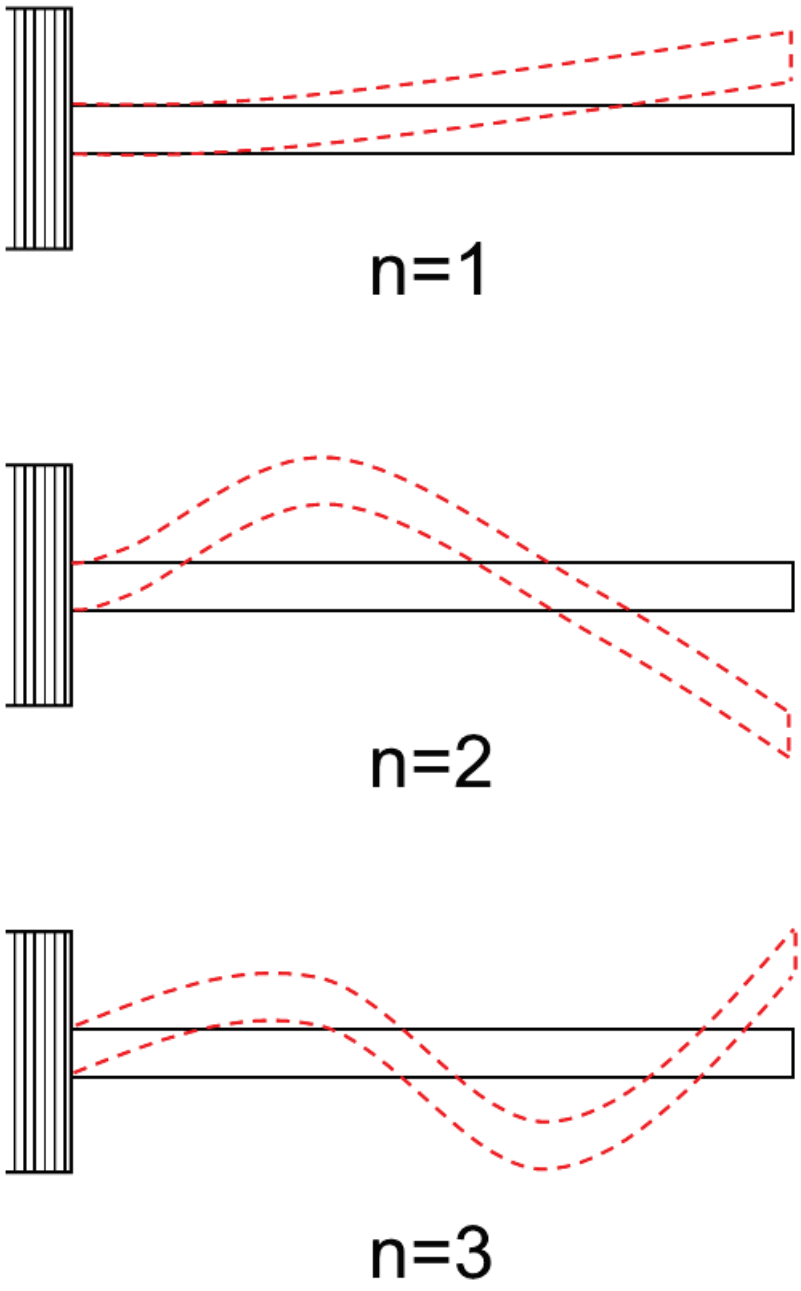

Figure 2.3: Resonance mode shapes for n=1, n=2, and n=3 of a singly clamped cantilever beam. The dotted red lines indicate the shape in resonant mode. Please note that the beam will also flex in the opposite direction as well.

2.2.3 Theoretical Resonance Tables

The devices made for this work have a thickness of 145 nm of silicon (which is the thickness of the device layer of the SOI substrate used), and 29 nm of metal, for a total thickness of 174 nm. The thickness of the metal deposited was determined from a QCM in the tool during deposition. More information about device dimensions and fabrication can be found in Chapter 3. The cantilever lengths were chosen to range from 2.5 μm to 7 μm. The device lengths have a large effect on the resonant frequency. To be detectable by the system, the resonant frequencies need to be within the range of the balancing circuit, discussed further in Chapter 5. Practically, this was below 200 MHz. The width of devices is chosen to be 500 nm. The devices need to be wide enough that there is adequate surface area for the analyte to adsorb to the surface. Too wide, and the effective mass of the resonator will increase, decreasing sensitivity. The width also cannot be arbitrarily small due to mechanical stability during oscillation. It is undesirable to have movement out of plane. Modeling of the movement of the cantilevers was done by a previous student in the group, and the model was consulted in determining the appropriate width for these resonators [5]. It should also be noted that resonant frequency is not the only deciding factor in device size and configuration, and physical limitations exist in fabricating devices on the nano and micro scale. Photolithography and electron beam lithography have practical limits on the smallest size of device possible. Practically, optical lithography cannot make features smaller than 1 μm. There is a greater possibility for fabrication failures when pushing the resolution limits of photolithography equipment.

The following were determined to be the theoretical resonant frequency of the different devices, "U"-shaped and doubly clamped.

Length [μm]	Frequency [MHz]		
	n = 1	n = 2	n = 3
1.0	1490	4138	8110
1.5	662	1839	3605
2.0	372	1035	2028
2.5	238	662	1298
3.0	166	460	901
3.5	122	338	662
4.0	93	259	507
4.5	74	204	401
5.0	60	166	324
5.5	49	137	268
6.0	41	115	225
6.5	35	98	192
7.0	30	84	166
7.5	27	74	144
8.0	23	65	127

Table 2.1: Theoretical resonance of doubly clamped cantilevers

Length [μm]	Frequency [MHz]		
	n = 1	n = 2	n = 3
1.0	166	1490	4138
1.5	74	662	1839
2.0	41	372	1035
2.5	27	238	662
3.0	18	166	460
3.5	14	122	338
4.0	10	93	257
4.5	8	74	204
5.0	7	60	166
5.5	6	49	137
6.0	5	41	115
6.5	4	35	98
7.0	3	30	84
7.5	3	27	74
8.0	3	23	65

Table 2.2: Theoretical resonance of “U”-shaped cantilevers

By mathematically modeling the behaviour of these cantilevers, one can approximate where to find an frequency response when later testing the fab-

ricated devices. This is important as the apparatus used to tune the devices is manually operated. The magnetomotive apparatus and testing system is described further in Chapter 5

Chapter 3

Fabrication

3.1 Process Flow Background and Introduction

This work involved fabricating novel high-sensitivity gas sensors based on resonant MEMS and NEMS structures [5]. The MEMS/NEMS devices are doubly clamped beams and "U"-shaped variations of single clamped resonant beams. The two types of beams vibrate in and out of plane with magnetomotive actuation in order to measure adsorption of analyte due to the added mass causing a shift in the resonant frequency. When a time-varying (AC) current is run through the device in the presence of a magnetic field, a Lorentz force is generated, driving the sensors into resonance at appropriate excitation signal frequencies.

Fabrication of free-floating devices is complex as a top-down approach is often required at the micro- and nano-scale. With a top-down approach, the bulk material must be patterned and etched to reveal the desired devices out of the substrate material and/or layers of thin films. Once formed, the cantilever devices must remain attached to the substrate and be sufficiently anchored for mechanical stability. A difficulty of a top-down approach for free-floating devices is material must be removed from underneath the cantilever to allow them to move freely. This can be achieved by patterning a device layer of material that is situated on top of a release layer. When the sacrificial release layer is chemically removed strategically from underneath the device layer, the devices will be able to move. However, the release layer cannot be removed

in its entirety or else the devices will no longer be anchored to the substrate. Instead, if an appropriate material is chosen the unreleased sections of the sacrificial layer can act as the anchors that secure the devices to the substrate. The materials chosen for the device layer, and sacrificial layer must also have favorable selectivity in their etch rates. If when attempting to remove the sacrificial layer the device layer was also partially or completely removed, the devices would not be functional.

Another challenge is to design a process flow that will allow the small scale required for the cantilevers to operate in an appropriate frequency range, while still having large enough components to connect to large systems. The scale between the contact pads required for electrical connections to outside systems needed to drive the cantilevers into resonance and the cantilevers themselves is the difference between hundreds of micrometres and hundreds of nanometre (3 orders of magnitude difference). The practical techniques to manufacture devices on these two different scales are vastly different to achieve such different resolution. This chapter will outline the fabrication process flow used to make the desired devices. A SEM image showing a completed doubly clamped beam is shown in Figure 3.1 .

3.2 Summarized Process Flow

The process flow consists of four distinct phases that will be discussed in detail in this chapter:

1. High resolution electron-beam lithography (EBL) to define the submicron scale resonator beams, followed by etching.

2. Optical photolithography to define the larger traces and contact pads required for interfacing, followed by etching.

3. Vapour-phase HF release of the sacrificial layer to allow for free floating cantilever beams.

4. Metal thin-film deposition for electrical conduction.

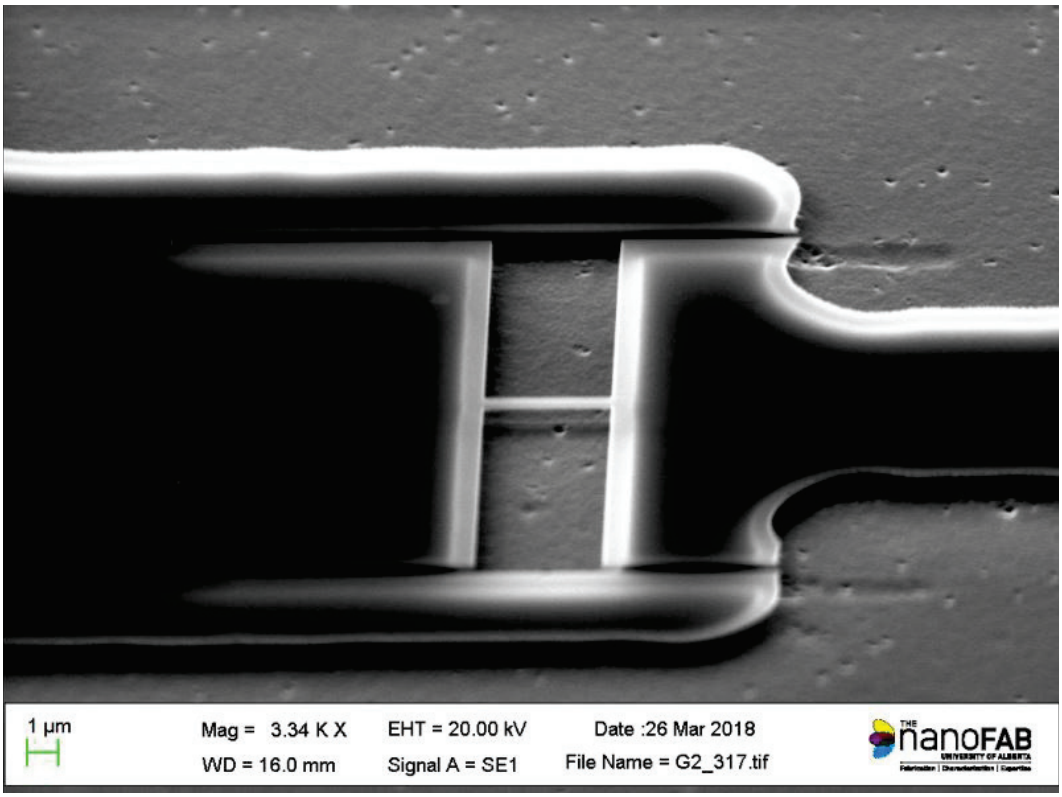

Figure 3.1: SEM Image of a doubly clamped MEMS cantilever

All processing of the devices is done at the University of Alberta nanoFAB Fabrication and Characterization Centre. In future work, the final product will have GLAD films deposited on them in order to determine the effect GLAD films have on increasing absorptivity for select gases and sensitivity of sensors. This would allow for further functionalization of the devices. Fig. 3.2 depicts the overall process flow and is meant to provide the reader with a visual reference for the remainder of this chapter.

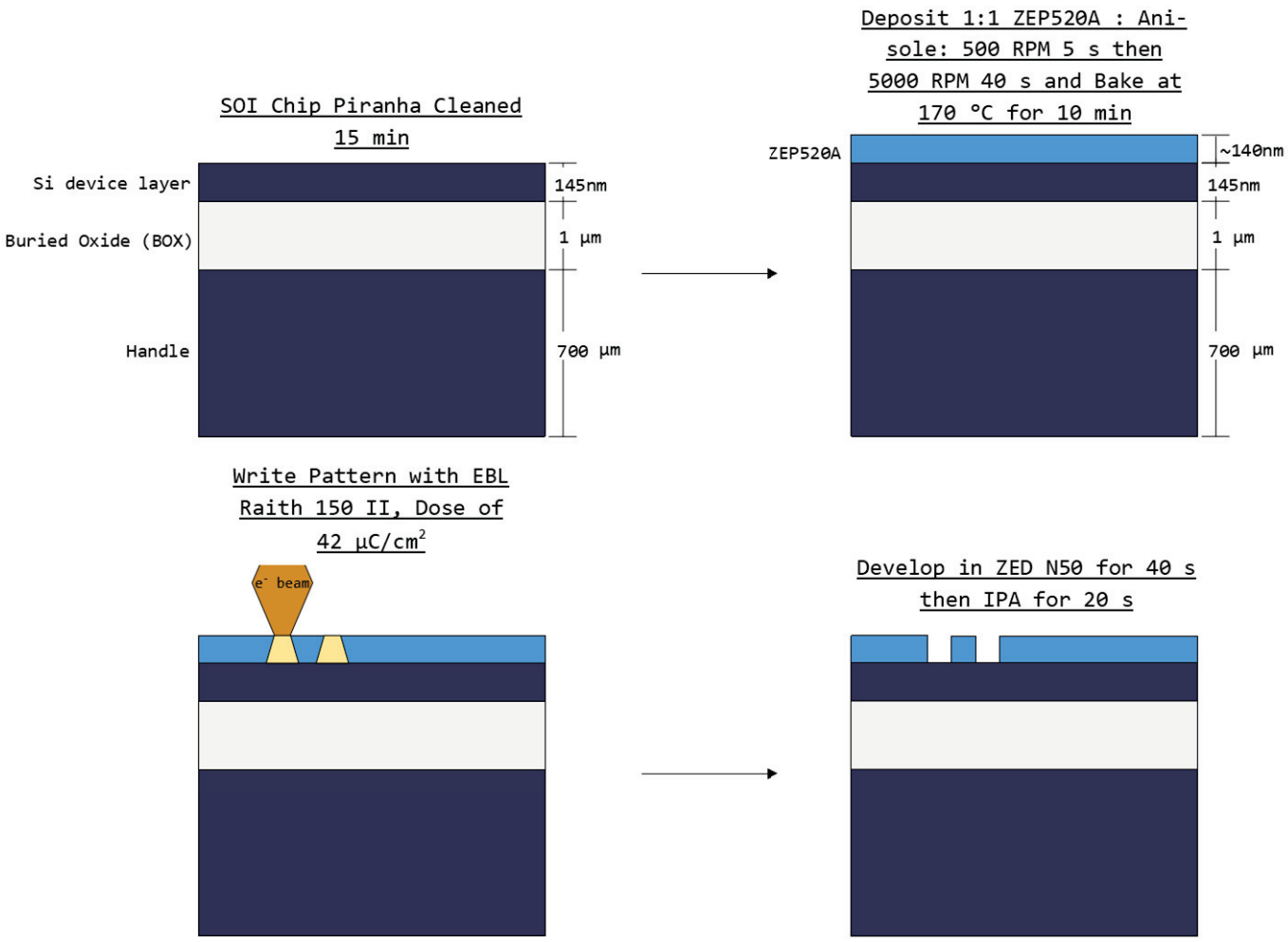
SOI Chip Piranha Cleaned
15 min
Si device layer
Buried Oxide (BOX)
Handle
145nm
1 µm
700 µm
Deposit 1:1 ZEP520A : Ani-
sole: 500 RPM 5 s then
5000 RPM 40 s and Bake at
170 °C for 10 min
ZEP520A
~140nm
145nm
1 µm
700 µm
Write Pattern with EBL
Raith 150 II, Dose of
42 µC/cm²
e⁻ beam
Develop in ZED N50 for 40 s
then IPA for 20 s

Etch in Oxford Estrelas ICPRIE for 50 s using "Unswitched"

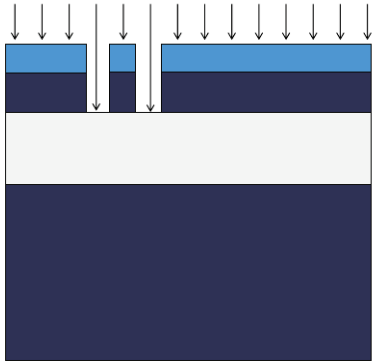

Remove Resist with Acetone ~1 min + IPA Rinse Followed by Piranha Clean 15 min

Prime with HMDS Deposit HPR 504: 500 RPM 10 s then 4000 RPM 40 s and Bake at 115 °C for 90 s

Exposure with UV Light on ABM Mask Aligner Dose of 130 mJ/cm^2

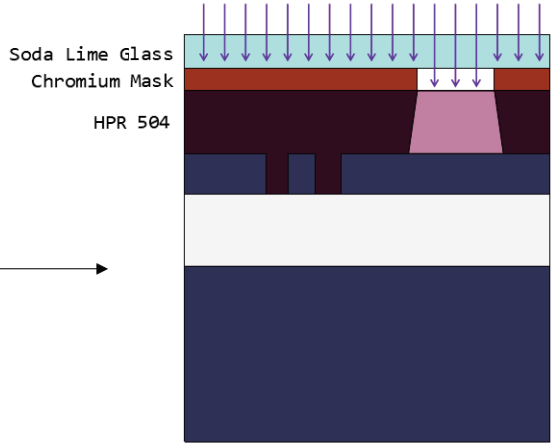

Develop in 354 Developer for 35 s Followed by DI Rinse and Nitrogen Dry

Etch in Oxford Estrelas ICPRIE for 50s using "Unswitched"

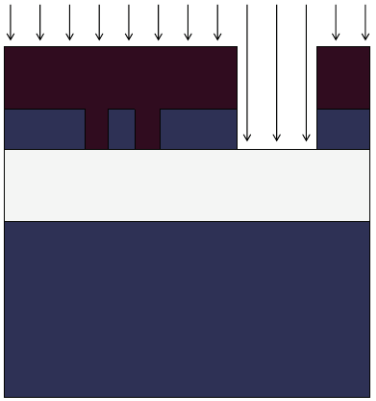

Remove Resist with Acetone ~1 min + IPA Rinse Followed by Piranha Clean 15min*

*To be added at this step: Increase Piranha clean to 30min. Add oxygen plasma ashing, up to 30min

Release Devices using VHF at 10 Torr 8 mgPm H_2O for 1400 s on BOX

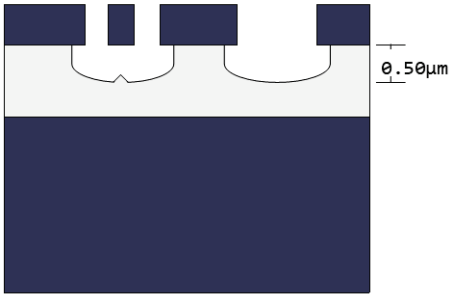

Figure 3.2: Process Flow Diagrams

3.3 Substrate

The resonators need to be fabricated out of a thin material in order to minimise their mass. The smaller the size and mass of the resonator, the greater the effect adsorbed analyte molecules will have on the resonant frequency of the devices. Reducing the thickness of the beams also reduces the stiffness, lowering the resonant frequency [6]. The reduced stiffness also allows for greater amplitude of vibration, making measurement easier [5], as discussed in Chapter 2.

The devices were built out of 1×1 cm SOI (silicon on insulator) chips with a 145 nm monocrystalline intrinsic Si device layer and a 1 μm buried oxide (BOX) layer. SOI devices are a common choice in microfabrication [10] [28]. Silicon and its oxide shows favorable selectivities during etching; meaning that once the silicon device layer is patterned, the buried oxide layer can be removed without substantial damage to the device layer.

It is also critical that the substrate, sacrificial layer, and device layer have good adhesion with one another. In this instance, the oxide layer can be grown thermally on standard Si substrates. Si substrates have been the default substrate of the microfabrication industry for many years [10] [28]. This means that many processes exist for the patterning of the device layer.

The Si device layer that will make up the cantilever beams, and the contact pads and electrical traces will be patterned and etched before mechanically releasing the devices by selectively etching away the BOX layer. To reiterate, the BOX serves three key purposes:

1. Providing electrical insulation for devices, reducing parasitic capacitances and losses.

2. Allows for free floating and movable structures.

3. Provides structural stability for the resonators.

In order to have the single crystalline Si device layer on top of the sacrificial buried oxide layer, the chips are cut out of a SOITECH SOI, RF-MEMS

wafer made with SmartCut technology [29]. These substrates are made by embedding ions in a Si wafer with a grown oxide on the surface. The embedded ions allow the wafer to be mechanically split at the embedded point. The oxidized and ion embedded wafer is bonded to another Si wafer, then the wafer is split. This leaves a largely silicon substrate with a buried oxide layer. The advantage of this process compared to depositing the desired films through other means, is that the device layer is single crystalline silicon, rather than polycrystalline silicon. Single crystalline silicon and polycrystalline silicon have different electrical and physical properties; with single crystalline being favorable for these devices. The depth of the device layer is controlled by the ion depth. Alternatively, SOI substrates can be made through oxygen implantation methods [28].

Finally the substrate is polished to provide an even device layer surface [29]. These wafers can be purchased as substrates for manufacturing of MEMS and NEMS devices. Purchasing pre-made SOI wafers that are readily available on the market allows a researcher to start further along a fabrication process flow.

3.4 Electron Beam Lithography

The vibrating beams need to be defined with resolution on the scale of tens of nanometres to achieve the small sizes and importantly low overall masses needed. Optical lithography will not provide the desired precision for such small structures. Optical lithography can only provide precision on scale of micrometres. This is due to limitations from the wavelength of UV light. On the other hand, the contact pads on the devices (which are on the scale of micrometres) are far too large for EBL to be practical for the entire chip. EBL is a direct patterning technique. The electron beam on the surface must dwell at each point a sufficient time (generally hundredths of milliseconds over an area on the scale of nanometres). Because of this, EBL is incredibly time consuming for large features (on the scale of micrometres or millimetres) which could take several hours to pattern [10]. This amount of time is impractical when more efficient options are available.

A combination of e-beam and optical lithography will provide the desired structures in the most practical manner. Only the features that require the precision of e-beam will be patterned with it, while larger features will use optical lithography, thereby yielding the desired structures, and saving substantial time and money. The smallest features - cantilevers and alignment marks - will be patterned with EBL, whereas the contact pads and electrical traces leading to the contact pads will be patterned with optical lithography. Fig. 3.3 shows the electrical traces; where the electrical connections will be made through pins on the three large square contact pads.

To begin fabrication, the SOI wafer was diced into smaller 1 cm $\times$ 1 cm chips. Smaller chips allow for reproducibility, ease of instrument design, and meet size limitations on the EBL and testing apparatus [5,30]. The permanent magnet assembly that will be discussed in later chapters can only practically fit small chips. The small size allows for an overall smaller volume vacuum chamber during testing: allowing for faster pump-times.

Before lithography can begin, the blank 1 cm $\times$ 1 cm SOI chips must be cleaned. The chips were cleaned with a hot piranha solution (3:1 H_2SO_4 (96%) : H_2O_2 (30%)) for 15 min to remove any organic contaminants [31]. Any contaminants or debris on the surface of the sample will have a negative impact on the following lithography. The dicing process leads to a significant amount of contamination on the surface of the samples, requiring a cleaning step at this part of fabrication. Once clean, the chips are removed from the solution, rinsed with deionized (DI) water to remove piranha solution from the surface of the chip and dried with a nitrogen gun. The chips were cleaned in batches of up to a dozen at a time for efficiency.

E-beam lithography was performed after piranha cleaning. E-beam lithography is very time consuming and costly when patterning large features such as contact pads [10, 30]. Just patterning the small cantilevers takes several hours. Including the time for alignment and focusing, this researcher would take an average of 2 hours to pattern a small batch of 3 chips with the systems available at the time. Direct write lithography techniques take longer for exposure than masked techniques, with the benefit being smaller overall

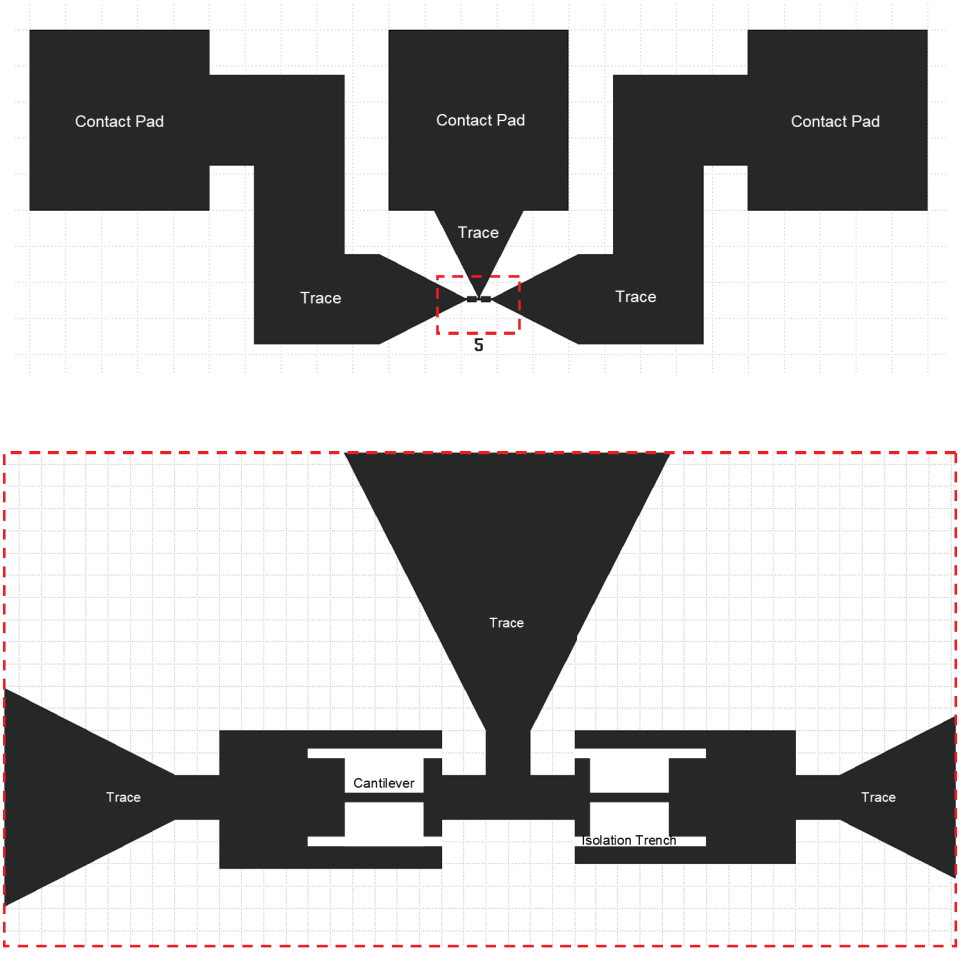

Figure 3.3: Image of the .gds photomask design file showing the electrical traces that will connect the contacts with the cantilever devices. The top image shows the three square contact pads that will connect to the testing assembly. The electrical traces lead to an area highlighted by a red dotted square. The area indicated in the red square is shown in a magnified image below. In the magnified image, the final cantilever that will be separately pattered by EBL is shown with corresponding isolation trenches. The zoomed image is not to scale and proportions have been enlarged for readability.

attainable resolution. To maximise efficiency (and minimise cost), only the smallest parts of the pattern, the cantilevers themselves, electrical isolation trenches, and alignment marks (required for later optical lithography) were patterned by e-beam; these are the only features small enough to need the resolution of EBL. The remainder, electrical traces leading to contact pads, and the contact pads themselves are patterned with optical lithography in a later step.

The resist chosen was Zeon Corporation's ZEP520A photoresist [32]. A Brewer resist spinner was used for this step. After centering on the chuck, the resist was applied to the surface using a micropipette until the surface was completely covered, to prevent waste and bubbles. Bubbles or contaminants in the resist could lead to "comets" or uneven streaks in the resist. ZEP resist was spun onto the wafer, and baked to set the properties of the photoresist.

The resist, 1:1 ZEP520A : Anisole Dilution, has a target thickness of 140 nm. Generally, thinner resists have better resolution compared to thicker resists [4]. The spin parameters for the chip were 500 rpm for 5 s, then 5000 rpm for 40 s.

An additional cleaning step was included before baking to remove any photoresist residue from the underside of the chip; which is very difficult to avoid when spin coating square substrates. Any residue could prevent the chip from sitting flat in the RAITH-II e-beam exposure system used, which could cause stitching errors and improper focusing, leading to poorer resolution if the chip were to shift while patterning (due to unstable contamination under the chip combined with stage movement) [10, 30]. In addition, if the chip does not sit flat in the system, the system would be out of focus in areas that were sitting higher or lower than the point where focusing was performed. Areas that were in poor focus due to unlevel chips will have inconsistent patterning, and poorer resolution and exposure over the surface of the sample. To prevent this, a cleaning step is required at this point. The bottom of the chips were cleaned by securing them upside down using plastic clamps, and scrubbed lightly with a cleanroom swab dipped in acetone. A few seconds are taken while the chip is still upside-down to ensure all acetone has evaporated, before

placing it on the vacuum hot plate. This was done to prevent evaporating acetone from interacting with the resist on the surface of the chip. The chip was baked at 170 °C for 10 min to remove resist solvent and solidify the resist.

Once prepared, the chip will be moved onto the stage for writing. Fine features, such as the resonators themselves, require slightly different parameters than the larger feature such as the alignment marks; for efficiency of writing of large features while conserving the resolution needed for finer features The parameters for e-beam are included in Table 3.1.

Parameters	Value
Resist	1:1 ZEP520A : Anisole
Spread	5 s @ 500 rpm
Spin	40 s @ 5000 rpm
Target Thickness	140 nm
Bake	10 min @ 170 °C
Dosage	42 μC/cm^2
Accelerating Voltage	10 kV
Beam Current	26.3 pA
Aperture (fine)	10 μm
Aperture (coarse)	30 μm
Dwell Time	0.0154 ms
Development	ZED-N50 Developer 40 s
IPA Stop Bath	20 s

Table 3.1: Electron Beam Lithography Parameters

The chips were loaded into the system and system alignment was performed. Generally, several chips (up to three) were patterned in one e-beam session. Time constraints meant only a couple of chips could be reasonably exposed and developed in a day. After e-beam exposure, the chips were developed, and inspected by optical microscopy. The chips were developed for 40 s in ZED-N50 developer, followed by a 20 s bath in IPA (isopropyl alcohol) to stop the development process. The chip was then rinsed in DI water then dried with N_2 gas. Microscopy images were taken at this point to verify good development (Fig. 3.4 and Fig. 3.6).

Figure 3.4: Microscopy images of <5 μm long, 500 nm wide doubly-clamped cantilevers post EBL and RIE

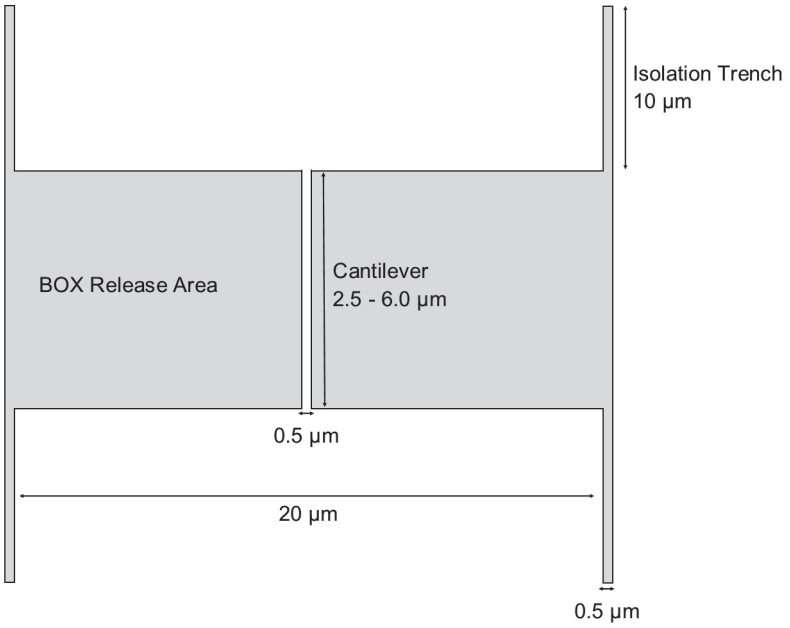

Figure 3.5: Diagram of dimensions of double clamped cantilever beam.

Figure 3.6: Microscopy images of <5 μm long, 500 nm wide "U"-Shaped cantilevers post EBL and RIE

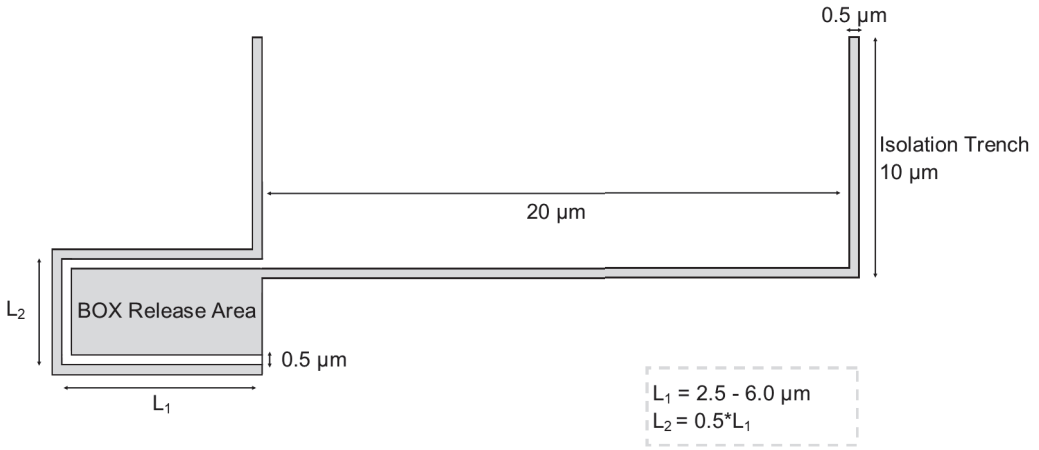

Figure 3.7: Diagram of dimensions of U-shaped cantilever beam.

3.5 Reactive Ion Etching

The next step was reactive ion etching (RIE) of the top silicon device layer with the Oxford Estrelas DSE. A 2 min conditioning run was run before any sample etching. The conditioning run ensures repeatability between batches, as the chamber will be in a known state before etching. Any other recipes run with different chemistries by other users could interfere with etch rates or introduce additional contamination. The recipe used is a modification of the Bosch process, where the passivating polymer used to prevent sidewall etching is pumped in at the same time as the etching agent, SF_6 [10]. As the device layer is only 145 nm thick, this process is sufficient for etching nearly anisotropically. The Oxford Estrelas can only accommodate whole wafers, so the chips need to be bonded to a SiO_2 on Si carrier wafer using the adhesive "Crystalbond" and a hotplate at 65 °C . The selectivity between SiO_2 and Si is favourable for this process, (greater than 50:1 Si:SiO_2) allowing for greater etch rate on the chips than the carrier wafer. The etch was done for 50 s. Microscopy after etching yielded images shown in Fig. 3.4, and Fig. 3.6. Once the etching is complete, the chips were removed from the carrier wafer with a hotplate at 65 °C. The carrier was cleaned with an acetone bath, followed by an IPA bath, then a DI water rinse, completed by drying with N_2 gas for the next user. If there is visible residue on the underside of the chips, they can be cleaned with the same acetone process.

3.6 Photolithography and Etching of Contact Pads

The chips were then cleaned using a 15 min piranha solution to strip the remaining EBL resist and any residual Crystalbond from the etch step. On the photomask, there is a 2×2 grid of 4 patterns, two for singly clamped layout and two for the doubly clamped layout on the photomask, that are rotated through during exposure, allowing for a clean spot on the mask every time. Everytime the chips are exposed, they are brought into contact with the mask.

Any contaminants on the surface of the chip could be left on the mask, and deposited on the next chip. Additional care for the cleanliness of the process will lead to higher yield of the final product. The orientation of the singly clamped beams requires a slightly larger area for connecting to the contact pads due to their geometry. Once all used, the mask would be cleaned in cold piranha to prevent pitting of the chromium on the photomask, but to ensure removal of any organic residues. Mask layout of the contact pads is included in Fig. 3.8. Previously, the mask had a 3×3 grid of 9, however, limitations on the stage movement in the ABM mask aligner system rendered some the die in the bottom row unusable, leading to the choice to only have a 2×2 grid on the redesigned version. The consequence of having fewer die to choose from, however, requires more frequent cleaning of the mask. Every time the mask comes into contact with the chip, the chance of contamination being left on the mask increases.

During piranha clean, most surfaces become hydroxylated, rendering the surface highly hydrophilic [33]. As the photoresist is hydrophobic, the sample surface must hydrophobic for proper adhesion. In order to increase adhesion of the photoresist, the chip, once clean, will undergo vapor HMDS treatment using the YES HMDS Oven. Water adsorbed to the surface is removed by baking the chips at a high temperature. Following this, gaseous hexamethyldisilazane (HMDS) is flowed over the surface, adsorbing, and rendering the surface hydrophobic.

In earlier work by the ENL group, diluted HPR 504 positive-tone photoresist, at a 2:1 dilution ratio with ethyl lactate solvent, was spun onto the chip. The HPR photoresist was diluted in order to prevent beading at the edges and corners of the chip [5]. In H. Brausen's work, it was found that by diluting the photoresist, there was better chip coverage, especially in the corners of the chip [5]. Edge bead introduced during spin-coating of the resist can reduce the effective area for devices to be patterned on a substrate. However, chip design for fitting inside the vacuum system and probe assembly meant that the pattern for the contact pads did not extend to the edges of the chip, making this step unnecessary for this lithography pattern. Resist dilution can also

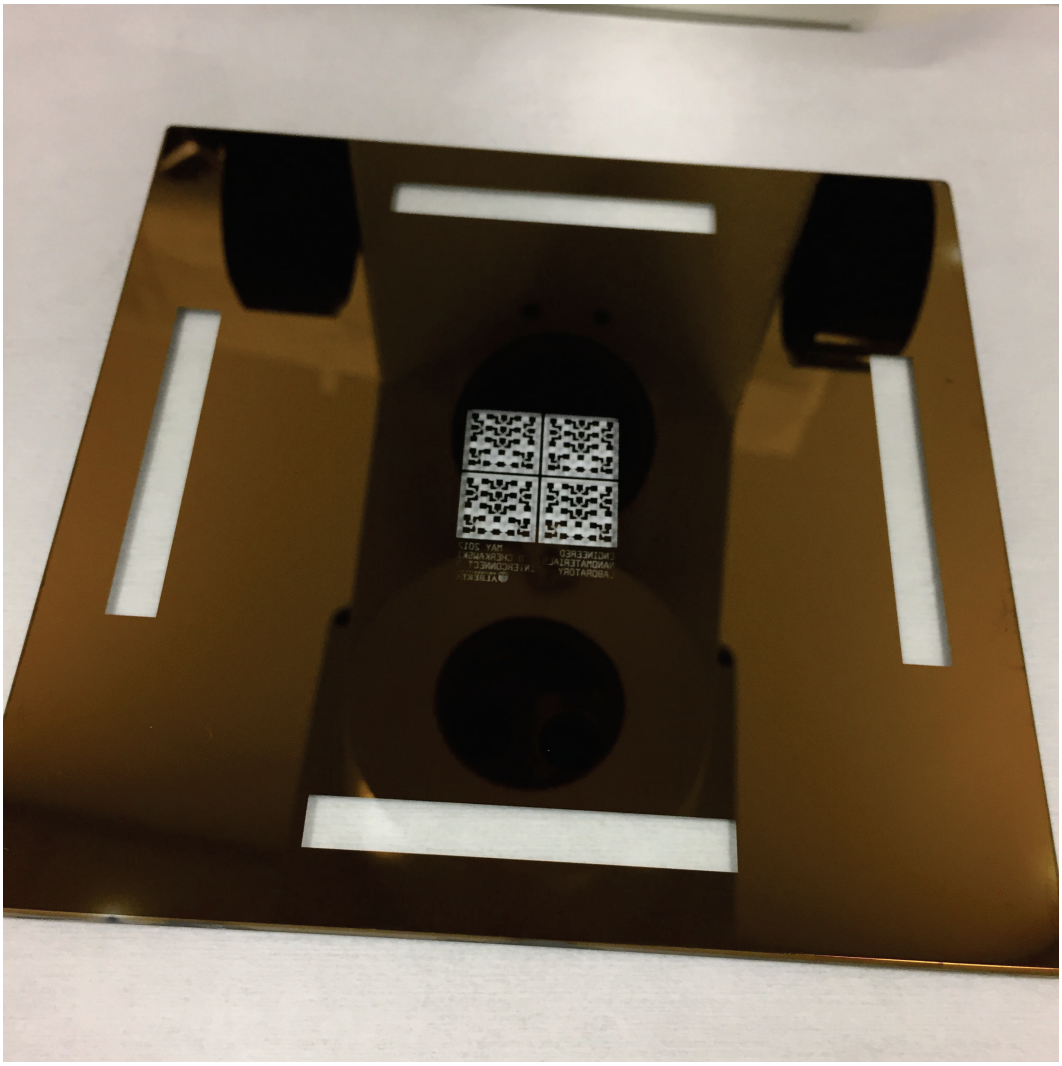

Figure 3.8: Photomask designed by B. Cherkawski for the contact pads and electrical traces for cantilever MEMS of various configurations.

lead to greater wicking to the underside of the square chips. This step will be helpful in the future if redesign of the layout is required in order to be able to fit more devices on a single chip. This redundancy was discovered during the patterning of the chips used for the development of the VHF process, included in Section 4.2. In addition, any errors during the dilution step can lead to particulate generation in the photoresist, or bubbles, which would lead to inconsistent photolithography [5].

All "U"-shaped cantilevers used the diluted HPR, whereas some of the doubly-clamped cantilevers, fabricated in a later batch, used undiluted HPR

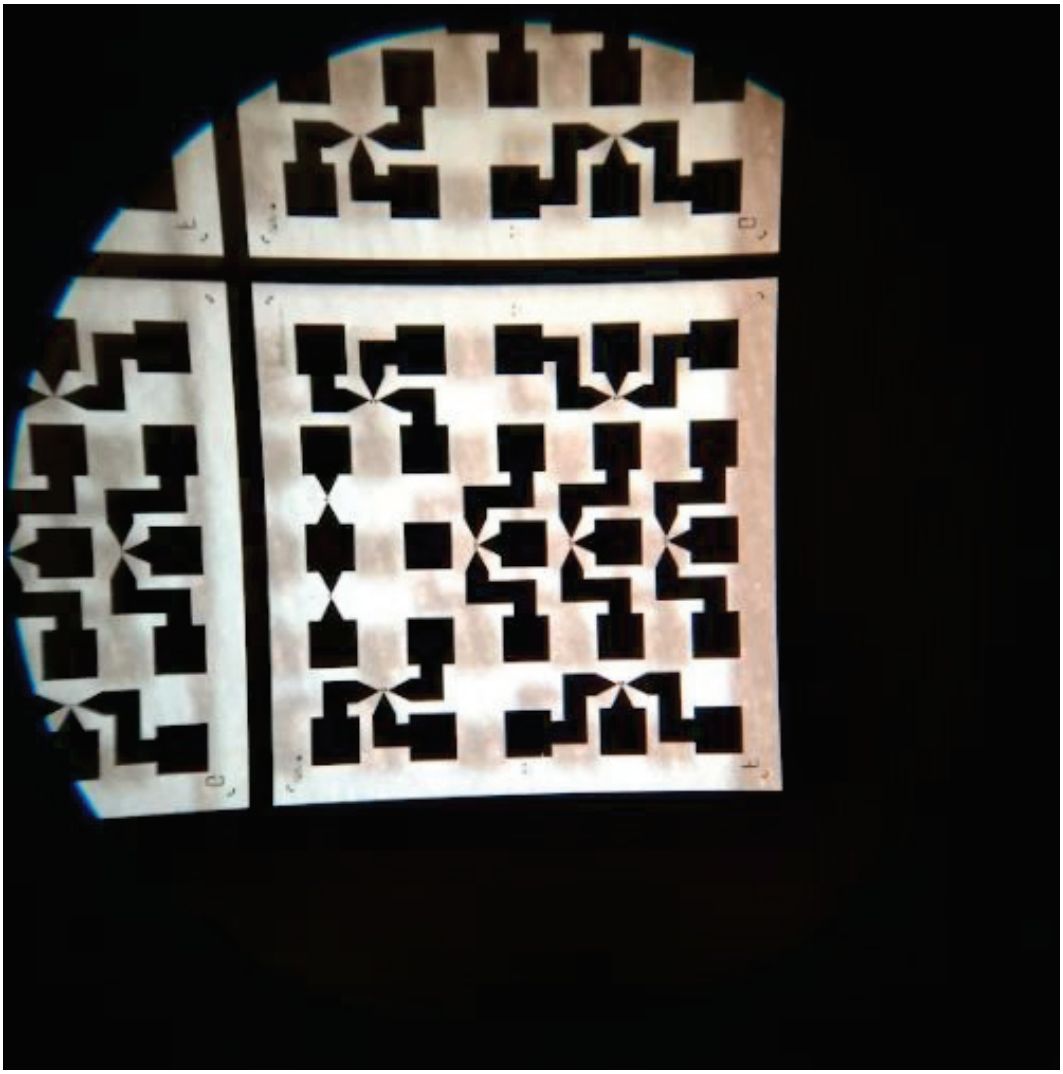

Figure 3.9: Photomask designed by B. Cherkawski. Microscope image of a single die on photomask.

504. This was because the "U"-shaped cantilevers were patterned by EBL first. No difference was noted under microscopy between the two resists (Fig. 3.10 and Fig. 3.11). The change was worked through with members of the nanoFAB staff to ensure consistent results, despite the change of process flow. Reducing the number of steps in a process flow improves yield as it reduces the opportunity for user error.

The diluted HPR 504 was pipetted onto the surface of the chip to reduce waste and bubbles in the photoresist, and spun for 10 s at 500 rpm, then 40

s at 7000 rpm. The chips were immediately baked on a vacuum hotplate for 90 s at 115 °C. Those chips with diluted resist were exposed to a dosage of 85 mJ/cm^2, whereas those who used undiluted HPR 504 underwent a dosage of 130 mJ/cm^2 (as the resist thickness was greater in the undiluted samples, requiring a higher dosage). Dose tests were performed on "dummy" chips to verify ideal dosages for each resist. The diluted chips were developed for 20 s in 354 developer, rinsed with DI water and dried using nitrogen.

In initial development, the chips were spun at a spread of 10 s at 500 rpm followed by 40 s spin at 7000 rpm as done for the diluted chips. A thinner resist, created by spinning at higher speeds, or lowering the viscosity through dilution, has a better resolution. Unfortunately, chip vacuum to the chuck was unreliable at higher speeds with the tools available at the time. After consulting with nanoFAB staff members, a revised spin speed and times with appropriate dosages was chosen to accommodate the change to undiluted resist, leading to a thicker photoresist, but with more precise results, and less chip damages and losses.

The new, and final process for undiluted resist was chosen to be 10 s at 500 rpm and 4000 rpm for 40 s. Table 3.2 contains the two recipes, for ease of comparison. This process was tested on the "C-chips" used in fine tuning the new VHF process, included in Section 4.2. Once the photoresist is spun onto the chip, the chip will be vacuum baked at 115 °C for 90 s (regardless of dilution or not), to set the properties of the photoresist. The chip will then be allowed to rehydrate in atmosphere for at least 15 minutes. Rehydration is required for the chemical reaction that occurs during UV exposure. Contact photolithography will be performed on the chip using the ABM Mask Aligner. Following exposure, the chip will be developed in 354 Developer for 35 s. After optical inspection, the chip will undergo another RIE step with the same parameters from Section 3.4 (50 s of the unswitched recipe in the Oxford Estrelas ICPRIE).

The development work that went into optimizing the optical lithography portion of the process flow led to less chip losses overall compared to previous work done by the group. As any chips that have already undergone EBL have

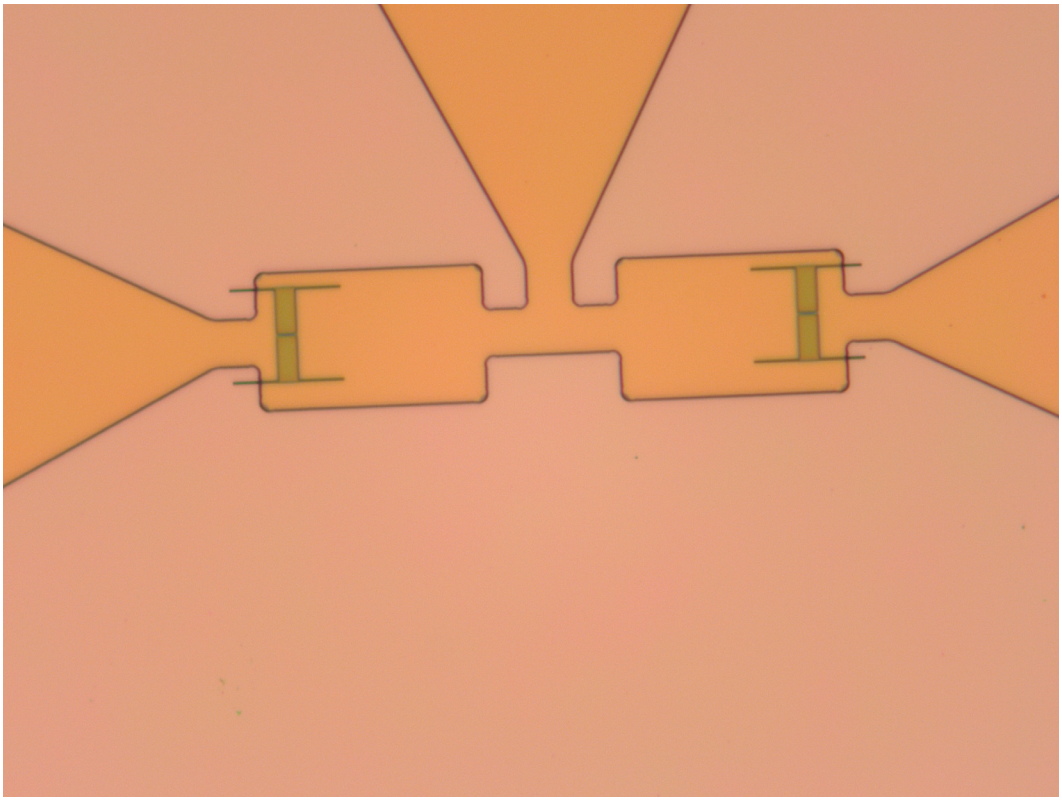

Figure 3.10: Microscopy images of 4 μm doubly-clamped cantilevers post contact pad and trace patterning with photolithography and RIE

a significant amount of time invested, any losses due to poor lithography are costly at this stage.

Parameters	Diluted HPR 504 Resist	Undiluted HPR 504 Resist
Spread	10 s @ 500 rpm	10 s @ 500 rpm
Spin	40 s @ 7000 rpm	40 s @ 4000 rpm
Bake	90 s @ 115 °C	90 s @ 115 °C
Dosage	85 mJ/cm^2	130 mJ/cm^2
Development	20 s	35 s

Table 3.2: Lithography Parameters

3.7 VHF Release and Process Development

In order for the devices to be able to actuate, they need to be released from the BOX sacrificial layer. Previously, the devices would be released using a combination of buffered oxide etch (BOE), and critical point drying (CPD).

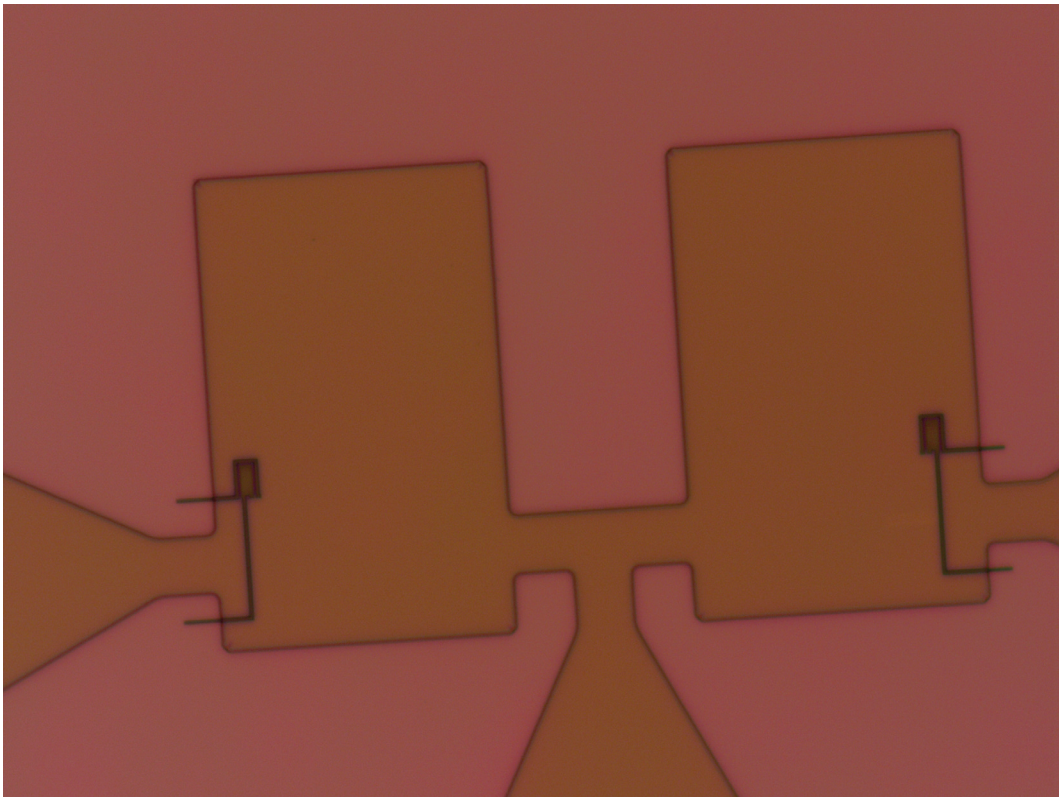

Figure 3.11: Microscopy images of 7 μm U-Shaped Cantilevers post contact pad and trace patterning with photolithography and RIE

However, stiction is a large issue with BOE release, requiring CPD to dry the devices appropriately [10]. Stiction, or static friction, occurs when liquid trapped in the MEMS evaporates. Surface tension pulls the device layer down during drying, leading it to stick permanently to the base layer, causing device failure. As well, the etch itself can take several hours to complete. With the necessary CPD step, the release of the devices could take an entire day's work. Any operator errors during CPD, such as slow transfer time to the tool, can lead to some drying, leading to stiction and reduced yield [10]. In addition, wet chemical etching with BOE involves significant safety hazards [10].

Vapour-phase HF (VHF) etching addresses all of these issues. As no liquid is present during VHF, stiction from water drying at this step is eliminated entirely. The process itself is much faster, and would take the user less than one hour (for a 1 μm BOX). This tool also includes an in situ NDIR sensor, allowing for process monitoring and end-point detection, speeding up process

development. If the etch time is insufficient it is easy to etch for several more minutes, as opposed to doing more BOE and having to repeat CPD [34]. Development of this process was conducted and fine tuned to this application. Due to several factors, this involved significant time for recipe development and fine tuning. This work is detailed in Chapter 4. At the time of development this was a new tool available to researchers in the facility.

3.8 Metalization

The device layer is intrinsic silicon and is not sufficiently conductive for magnetomotive actuation [10, 15]; the chips will need to undergo metalization. Using PVD on an electron-beam evaporation system, Al will be deposited onto the chips. Al is commonly used in microfabrication for metallization of devices [10]. Aluminum is less dense than other common materials such as gold, adding less mass to the resonator [15]. The Al deposition will occur at a pitch of 5 nm, and a rate of 1 Å/s. The Al film will need to be 5 - 50 nm for adequate conductivity [5]. In addition, a 1 - 5 nm thick film of Ti will be deposited before the Al in order to increase wear resistance from the contacts used to apply electrical current to the MEMS. Materials engineering analysis was performed by this author to introduce this additional layer. It was noted that in previous students work, repeated testing and probing of the devices led to significant damage of the contact pads, leading to failure of devices during re-testing. Titanium is several times harder than Al [35] and will improve longevity of the chips with repeated contacts during testing. The Ti thickness was 6 nm, and the Al thickness was 23 nm. The resistivity of Al is 2.65×10^{-6} Ωcm, making it appropriate for this application. The thermal expansion coefficient of Al is 23.0×10^{-6} °C^{-1}, Ti, 8.6×10^{-6} °C^{-1} [15], and Si $\times$ 2.3 10^{-6} °C^{-1} [10, 35]. The intermediary Ti, with a thermal expansion coefficient between that of Al and Si, should reduce stress gradients resulting from temperature shifts. The materials analysis for this decision was made by this author.

After metalization the devices would be ready for testing and SEM imaging.

A schematic depicting the complete process flow was shown in Fig. 3.2 earlier in this chapter.

3.9 Summary

Several changes in previous iterations of the process flow were implemented, increasing the number of chips that made it from the fabrication stage to testing from under 50% to 100% [5, 14]. The old process flow and the changes implemented by this author is shown in Table 3.3

Old Process Flow	New Process Flow
Piranha cleaned SOI chip	Piranha cleaned SOI chip
Spin coat ZEP520A : Anisole 1:1	Spin coat ZEP520A : Anisole 1:1
Expose cantilevers using EBL	Expose cantilevers using EBL
Develop with ZED N50 Developer 40 s	Develop with ZED N50 Developer 40 s
Etch 50 s Si with ICPRIE	Etch 50 s Si with ICPRIE
Strip resist acetone and IPA	Strip resist acetone and IPA
Piranha clean 15 min	Piranha clean 15 min
Spin coat HPR 504 : Ethyl Lactate 2:1	**Spin coat HPR 504**
Expose to UV light using mask aligner	Expose to UV light using mask aligner
Dosage 85 mJ/cm^2	**Dosage 130 mJ/cm^2**
Develop in 354 developer 20 s	**Develop 354 developer 35 s**
Etch 50 s Si with ICPRIE	Etch 50 s Si with ICPRIE
Strip resist acetone and IPA	Strip resist acetone and IPA
Clean EKC265 @ 65 °C 15 min	
Piranha clean 15 min	Piranha clean 15 min
	Optional O_2 plasma clean
BOE etch to release	**VHF etch to release**
Critical point dry	
Metalization Al	**Metalization Ti and Al**

Table 3.3: Process flow changes summary. Changes are highlighted in bold font.

Eliminating the dilution step for HPR 504 improved photolithography errors by reducing the number of steps, and reducing the chance for operator error. The photolithography parameters for exposure and development were re-optimized for the new process flow. Photomask redesign improved efficiency at the exposure step. An extra clean with EKC265 was removed, as it was

found contamination at this step was not from the etch, but rather organic contaminants in the CPD from other users. The VHF release was substituted for the BOE release and subsequent CPD step. More than 50% of chips were lost at this step in the old process flow due to stiction, organic contamination from the CPD chamber, or operator error in etch depth. VHF improved yield substantially at this step, eliminating stiction. It also eliminates the chance for under-etch failures as it is relatively easy to etch longer, as you do not need to repeat the CPD and risk losing majority of your chips for a top-up etch. The changes in the process flow took fabrication chip yield from less than 50% to 100%.

Chapter 4

VHF Device Release Optimization

This chapter outlines the design of experiment and process optimization for the switch from buffered oxide etch (BOE) device release and critical point drying (CPD) with CO_2 to vapor phase HF etching.

4.1 MEMS Device Release Background

A crucial step for device functionality in MEMS fabrication is device release. The sacrificial layer (the buried oxide in the SOI chip) must be removed sufficiently to allow free movement of the devices during actuation. However, enough oxide must remain to anchor the devices to the underlying substrate in the appropriate locations. Optimization of the process is needed to ensure fully released devices, while preserving the structural integrity of the anchoring points.

A standard way for device release is to use a combination of buffered oxide etchant (BOE) to remove the oxide via wet chemical etching, immediately followed by critical point drying (CPD) to remove any liquid from the sample to prevent stiction [10]. Hydrofluoric acid is a common etchant for silicon dioxide in microfabrication. Stiction and contamination introduced during CPD was a contributing factor to low yield in previous work by the ENL group [5]. Poor yield due to issues during device release is reported in literature as well [36]. The reaction by which SiO_2 is chemically etched is shown in Eqn. 4.1 [37].

$$SiO_{2(s)} + 4HF_{(aq)} \rightarrow SiF_{4(aq)} + 2H_2O_{(l)} \tag{4.1}$$

A consideration is as the reaction proceeds, fluorine is consumed in producing the etch byproduct silicon tetrafluoride. This means that the concentration of the acid decreases over time, slowing the effective etch rate. For thin films, on the scale of 10's of nanometres any loss in etch rate would be insignificant. However, MEMS generally have thick buried oxide layers. To ensure an accurate etch where the etch rate can be accurately determined for repeatable etch depths, BOE is used instead. BOE contains a lower concentration of HF, but also a buffering agent, ammonium fluoride. As HF is consumed, the ammonium fluoride provides additional fluorine to keep the concentration of HF constant:

$$NH_4F_{(aq)} \leftrightarrow NH_{3(aq)} + HF_{(aq)} \tag{4.2}$$

The constant concentration leads to a more consistent etch with less roughness of the etched surface from the more stable and slightly slower etch rate. Hydrofluoric acid has a favorable selectivity between silicon and silicon dioxide. The etch rate of Si in HF is near zero and considered negligible, whereas the etch rate of thermally grown SiO_2 in commercial BOE is several 10's of nm's per minute [38] [37]. Hard masking, where a protective thin film is deposited on top of the top layer, at this step is unnecessary as the Si will not be etched more than an negligible amount.

The BOE process is a wet chemical etch; exposure of the devices to liquid is unavoidable in this process. As liquid (water) trapped in the MEMS devices evaporates, surface tension pulls the device layer down during drying, leading it to stick permanently to the base layer via static friction (or stiction), causing device failure. BOE as an etchant can be a lengthy process, generally etching on the scale of 10's of nm's per minute [37]. A 500 nm buried oxide layer could take could take hours to complete with clean-up and CPD steps. To etch through 1 micron of BOX layer at a rate of 40 nm/min would take just under half an hour. Safety considerations and procedures add significantly

to processing time. Hydrofluoric acid is incredibly dangerous, and can be fatal if exposed by absorption into the body by skin contact, inhalation, or ingestion [39]. Neutralization procedures necessary in a shared use facility add to the time needed to complete a BOE process.

As a multi-step manual process, the opportunities for operator error was high, making repeatability of this step difficult. This release and dry step caused significant yield issues. Variance in etch rate due to agitation differences by the operator is difficult to duplicate. Not agitating the solution decreases the etch rate, leading to less undercut for the same length of etch time. Any end point uncertainty could not be confirmed until later in the process, making adding additional etching time difficult and complex.

After BOE etch, the water used to rinse the samples must be removed from the devices in a way that prevents surface tension and stiction. Stiction in particular was mitigated with critical point drying. By using liquid CO_2 under high pressures and low temperatures, the intermediary fluid used to keep the devices from stictioning can be removed from the devices. Water and CO_2 are not miscible, so after etching with BOE, the samples need to be submerged in a miscible intermediary liquid, such as IPA or methanol to remove the water [1]. The critical point drying process eliminates any possible surface tension from the liquid as it dries by preventing crossing of the liquid/gas transition boundary shown in Figure 4.1. Pressure and temperature is carefully controlled to keep the CO_2 liquid until the temperature and pressure are at the critical point, at which the system can be slowly vented and CO_2 released [1].

With the necessary CPD step, the release of the devices could take an entire day's work. Any operator errors during CPD, such as slow transfer time to the tool, can lead to some drying, leading to stiction and reduced yield [10]. If it is found after the CPD step that further BOE etching is required, the whole process must be repeated from the beginning. This would be very time consuming, and frustrating for a researcher. Besides using previous etch rate data, there would be no concrete way to be sure that the devices were adequately released until after CPD was complete as the devices must remain submerged.

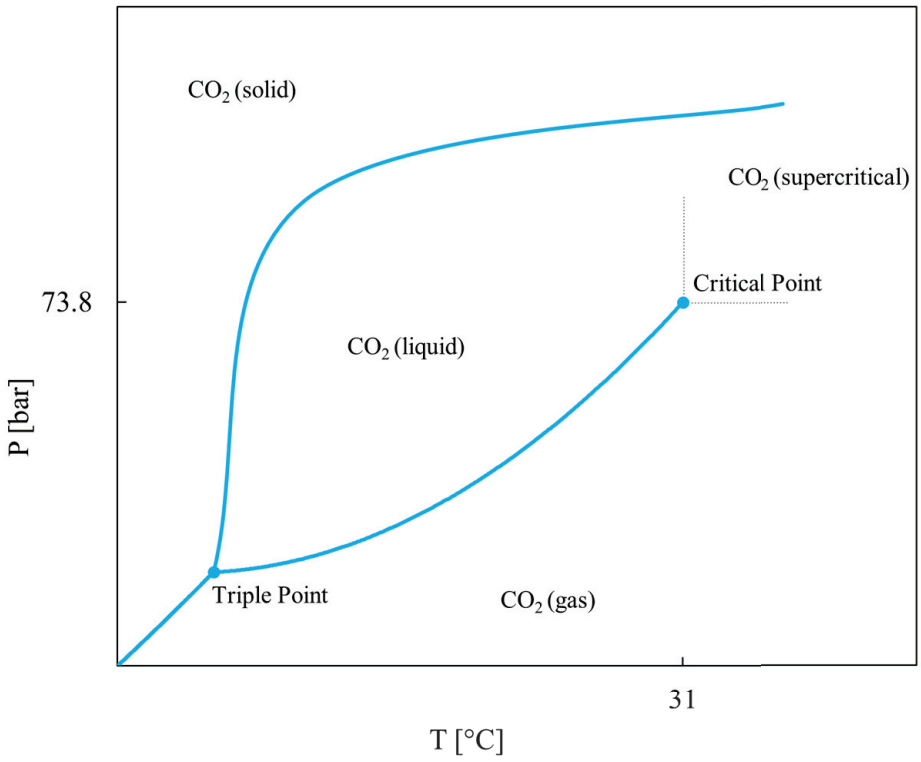

Figure 4.1: Carbon Dioxide Pressure-Temperature Phase Diagram Adapted from [1] and [2].

Another problem arising from CPD is contamination from other user's processes, as on occasion, significant contamination was noticed after CPD. This is an unavoidable hazard in a shared lab space.

Vapour-phase HF (VHF) etching solves all of the mentioned problems with BOE and CPD. As no liquid is present during VHF release, stiction from water drying at this step is eliminated entirely. The process itself is much faster, and would typically take the user less than one hour (for a 1 μm BOX layer). This tool, also includes an in situ NDIR sensor, allowing for process monitoring and end-point detection, speeding up process development. This sensor also allows for more accurate end point detection if etching all the way through the BOX layer. If, upon inspection, the devices are found to been underetched (not fully released), it is easy to etch for several more minutes vs. doing more BOE followed by CPD [34].

Another advantage is the automation of the process. With computers controlling etch times and parameters, operator error is reduced. The tool also means that the researcher does not need to work hands-on with highly hazardous BOE as all hazardous products are contained, and purged from the chamber.

However, to transition to a new process such as VHF requires an investment of time by the researcher into process optimization.

Before releasing the structures using vapour hydrofluoric acid (VHF), the wafers will again be cleaned in hot piranha etch for 15 min. Any polymer contamination on the wafer is detrimental, and could lead to pitting and contamination as outlined later in this section. Images taken before processing showed that the contamination was isolated to occurring at some point during the VHF step. As the chips were thoroughly cleaned of any organic residue using Piranha solution, it is very unlikely that this residue was caused from pre-existing organic contaminants. This particular residue was also not observed on any earlier chips processed using BOE and CPD.

HF requires a catalyst in order to dissociate [21]. The catalyst in this tool is vapour H_2O. Conveniently, one of the products of the reaction is H_2O(g) [21]. However, the amount of product produced during the etching can vary

significantly depending on the amount of exposed SiO_2, which will be more easily reached by the reactants; a microfluidics problem. The consequence is that every device design will require a unique etching recipe, even if composed of similar BOX thicknesses [34]. Multiple parameters, such as water partial pressure, or overall system pressure must be fine tuned in order to yield the desired device release. The reaction for VHF is shown in Eqn. 4.3. It should be noted by the reader the similarity with Eqn. 4.1, but this time, the phases of the reactants and products are different.

$$SiO_2(s) + 4HF(g) \rightarrow SiF_4(g) + 2H_2O(g) \tag{4.3}$$

4.2 VHF Release and Process Development

To fine tune the VHF process, 24 test chips were patterned using only photolithography and dry etching in order to approximate the amount of exposed SiO_2 on the chips, as the e-beam pattern area is small enough to be considered negligible in the effect of H_2O generation during etching. Each exposed e-beam area was approximately 100 microns square, compared to the largely open area of the chip in between contact pads. Removing the lengthy e-beam step allowed for more time to be spent of VHF development, and allowed for more optimization tests to be run.

To reduce waste from the relatively high cost of SOI wafers, chips that would have been otherwise discarded were chosen for initial tests. During dicing of the wafer, there are some wasted chips that are near the edges of round wafers that are irregularly shaped, and cannot be used for manufacturing the devices. The irregular chips were used for the first several rounds of tests, to get an approximate etch process developed first, and especially to measure the etch rate. The second phase of fine tuning of the process made use of used chips that had been scratched, or poorly processed (for example, poor, unsalvageable alignment between the e-beam and optical lithography pattern). The square, but damaged chips were a better approximation of the exposed SiO_2 area compared to the irregularly shaped chips, proving better for fine

tuning the recipe.

Tool manufacturer guidelines recommended by the nanoFAB gave a starting estimate on process times. It is known that increasing the HF flow rate decreases the etch rate, but improves uniformity, whereas increasing the H_2O flow rate increases the etch rate, at a loss of uniformity [34]. This is because of the catalyst H_2O is required for the HF to break-down into a reactable form. If the ratio of HF:H_2O is too high, the relative amount of catalyst (H_2O) is lower, leading to a lower reaction rate. Finally, an overall increase in system pressure increases etch rate, again at a loss of uniformity. A balance needs to be struck between the pressure of HF to H_2O to achieve a decent etch rate, without a significant loss of uniformity. It should be noted that there is inert carrier gas, N_2, to control system pressure as well. This is visualised in Table 4.1.

Parameter	Etch Rate	Uniformity
HF flow rate ↑	decrease ↓	increase ↑
H_2O flow rate ↑	increase ↑	decrease ↓
System pressure ↑	increase ↑	decrease ↓

Table 4.1: Parameter Effects in VHF Processing

Each parameter was altered independently until the desired results were achieved using the one factor at a time (OFAT) design of experiment approach. After performing the first test, visible and severe residue was present on all the chips, Fig. 4.3. This residue was not present before etching as their chips had undergone a piranha clean and had been visually inspected before the VHF etch. As an additional test, some chips underwent an oxygen plasma clean in addition to piranha cleaning before VHF, and the residue was still present. In addition, longer etches evidenced poor uniformity, showing a need to improve uniformity before running on chips that have undergone costly EBL. The initial test parameters are included in Table 4.2. All chips were qualitatively examined under optical microscope and notes taken on the quality of the surface of the chips post etching. SEM images were taken within a couple of days of VHF processing. Chips were kept in sealed containers in a

cleanroom environment until imaging could be completed.

Chip	Pressure [Torr]	Time [s]	Observations
C.1	13	150	Visible residue
C.2	13	300	Severe residue and pitting
C.3	13	200	Visible residue

Table 4.2: Test 1: VHF General Test

Clearly, parameters of the etch needed to be altered to achieve the desired results. It was determined that the pressure needed to be reduced until contamination was either reduced or eliminated. If the pressure in the system was too high, it was a possibility that by-products of the reaction could be condensing on the surface of the chip or not properly evaporating.

Chips C.4 - C.6 were run at incrementally lower pressures until residue was reduced as shown in Table 4.3. Chip C.7 was run at a shorter time than C.6 to rule out the possibility that the residue would drastically increase with longer etch times.

Chip	Pressure [Torr]	Time [s]	Observations
C.4	11	200	Reduced but visible residue
C.5	10.5	200	Reduced residue
C.6	10	200	minimal residue
C.7	10	150	minimal residue

Table 4.3: Test 2: VHF Pressure Test

The chips etched at lowered pressures yielded much better results. Keeping the pressure below 10.5 Torr decreased the residue considerably. However, running the process above 10.5 Torr showed visible residue. Chip C.5 showed minimal contamination compared to chip C.4, but with much less undercut, (Figs. 4.3, 4.4, and 4.5). Chip C.7 showed insufficient etch depth due to the etching time being too low. It was also found that chip C.7 was inadequately cleaned and images were not included in this work.

Round three of processing was to fine tune the data from round two, and is included in Table 4.4. The third test was to compare two times at similar

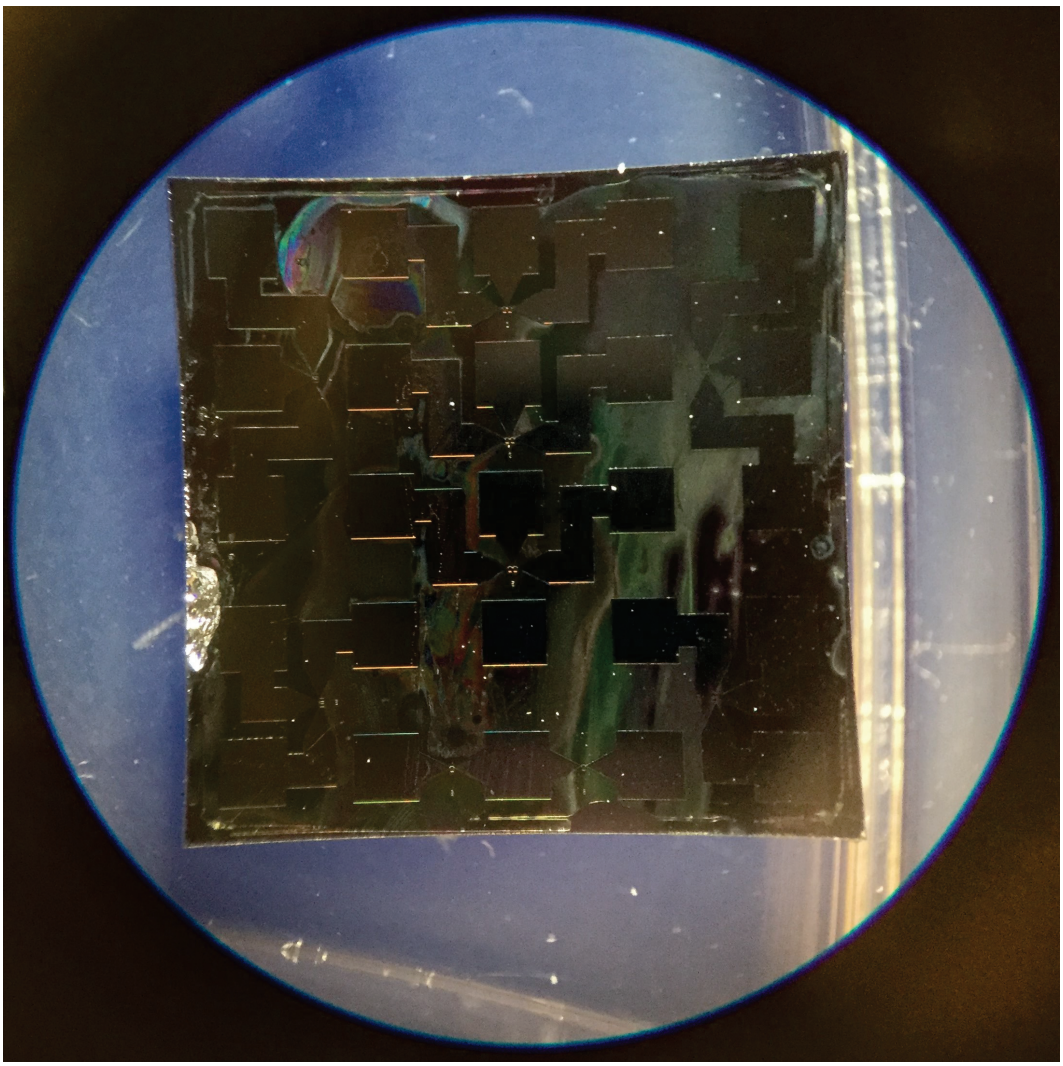

Figure 4.2: Microscopy image of chip C.1. Severe contamination visible on the chip after VHF etching, not present before. Chip was piranha cleaned immediately before processing, meaning the residue was unlikely to be organic.

pressures, to see if the length of etch leads to increased residue as C.7 will be considered an outlier.

Chip	Pressure [Torr]	Time [s]	Observations
C.8	10.5	175	Visible residue
C.9	10.5	225	Visible residue
C.10	10	175	Visible residue
C.11	10	225	Visible residue

Table 4.4: Test 3: VHF Pressure Test 2

Chips C.10 and C.11 (Figs. 4.7a, 4.7b) had the cleanest surfaces compared to C.8 and C.9 (Figs. 4.6a, and 4.6b) done at higher pressures. Comparing tests done at the same pressure, C.8 and C.9 showed no appreciable increase in contamination with increased time. This indicates that pressure had a greater effect on contamination than the time of the process. C.10 and C.11 also showed no appreciable increase in contamination with increased process time. However, the etch depth was insufficient for functional cantilevers. The desired etch depth was 500 nm, half of the BOX thickness. This etch depth will leave adequate anchoring for the beams via the remaining oxide under the electrical traces and contact pads. Etching more than necessary will increase the effective length of the cantilever which has a significant effect on the theoretical frequency, as discussed in Chapter 2 With contamination reduced, other etch parameters could then be investigated as per the OFAT method.

The next experiment served to alter the overall water vapour flow rate. For determining the effect of water, a system pressure was chosen where there was known residue (Table 4.5). If a pressure was chosen with no residue, then it would be difficult to determine if water pressure has an effect on the residue present. One factor will be altered and compared at a time as per the OFAT method. Relative water pressure was varied to determine the effect it has on the residue. Less residue was present when water was increased from 5 mgpm from previous runs to 6 mgpm (C.13) and 7 mgpm (C.12) as observed by optical microscopy. After, a pressure known to yield little contamination and a higher pressure (two different parameters) were chosen. Residue was

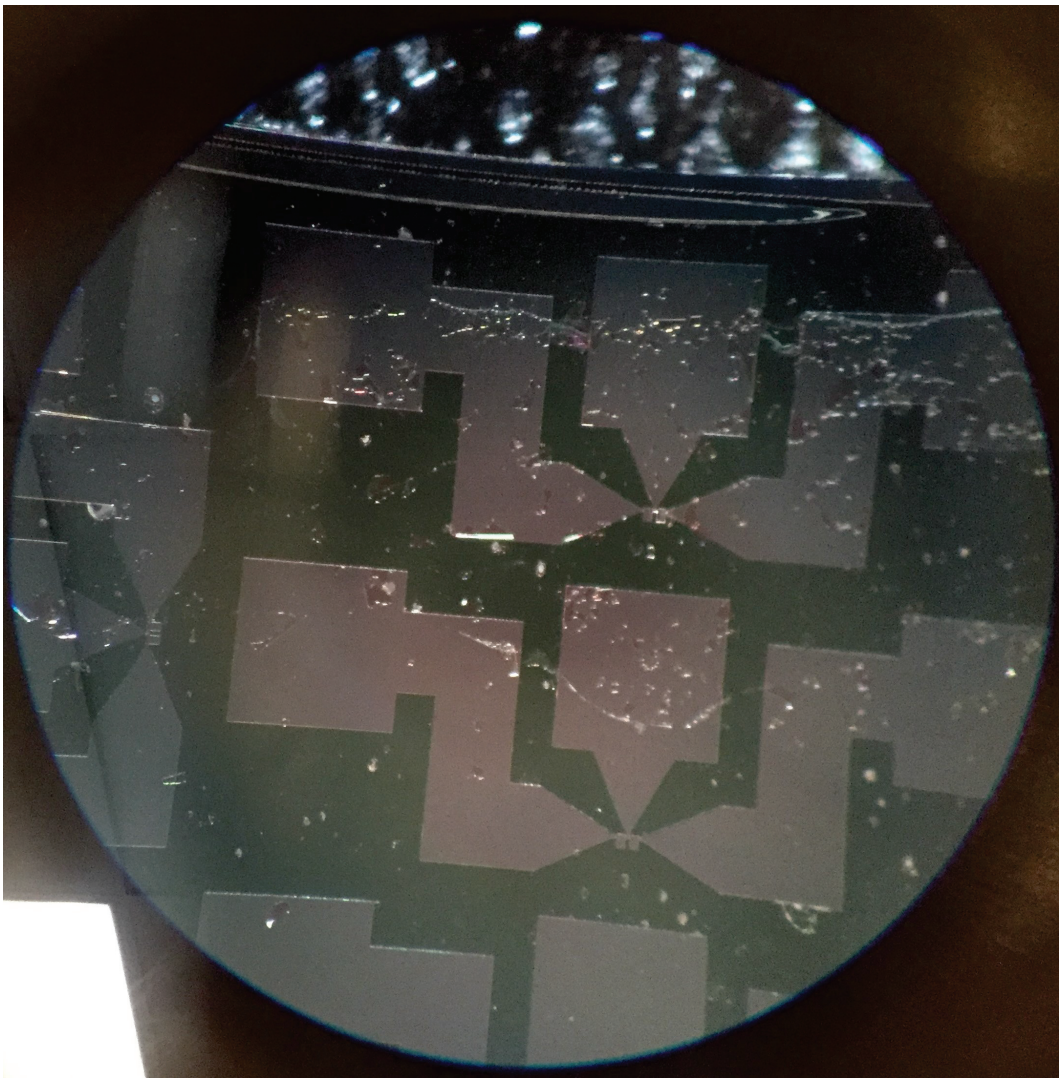

Figure 4.3: Microscopy image of chip C.4. Severe contamination visible on the chip after VHF etching, not present before. Chip was piranha cleaned immediately before processing, meaning the residue was unlikely to be organic. Compared to chip C.1, the residue on chip C.4 was reduced by lowering the pressure in the system during the etch.

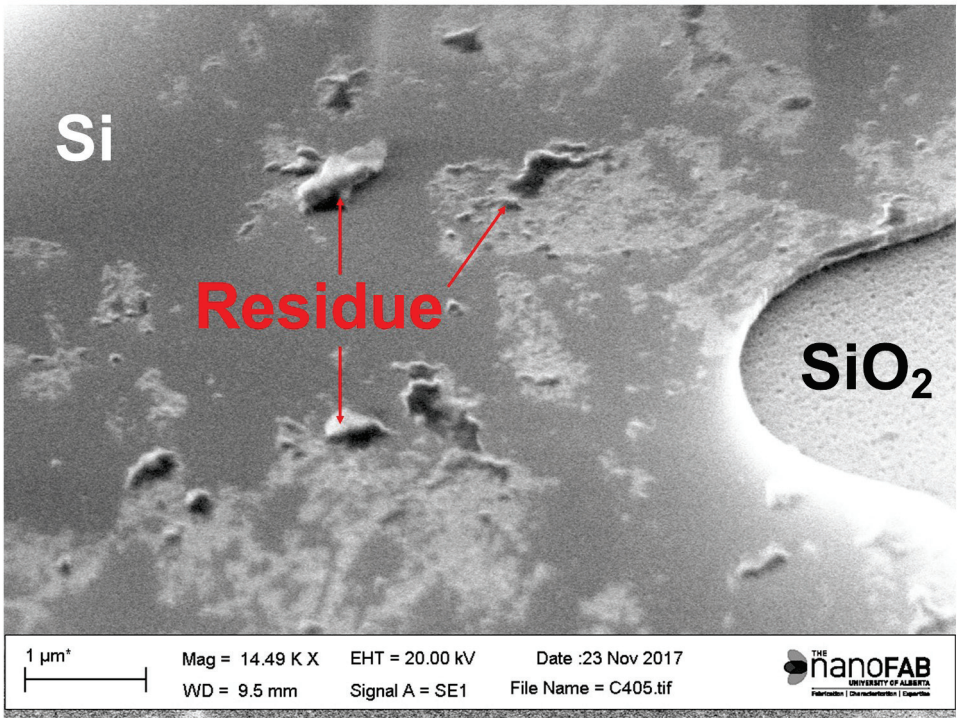

Figure 4.4: SEM image of Chip C.4, VHF etched at 11 Torr, for 200 s, severe contamination observed over the surface of the chip. Limited charging of the residue on the surface of the chip could be indicative of a inorganic residue on the surface.

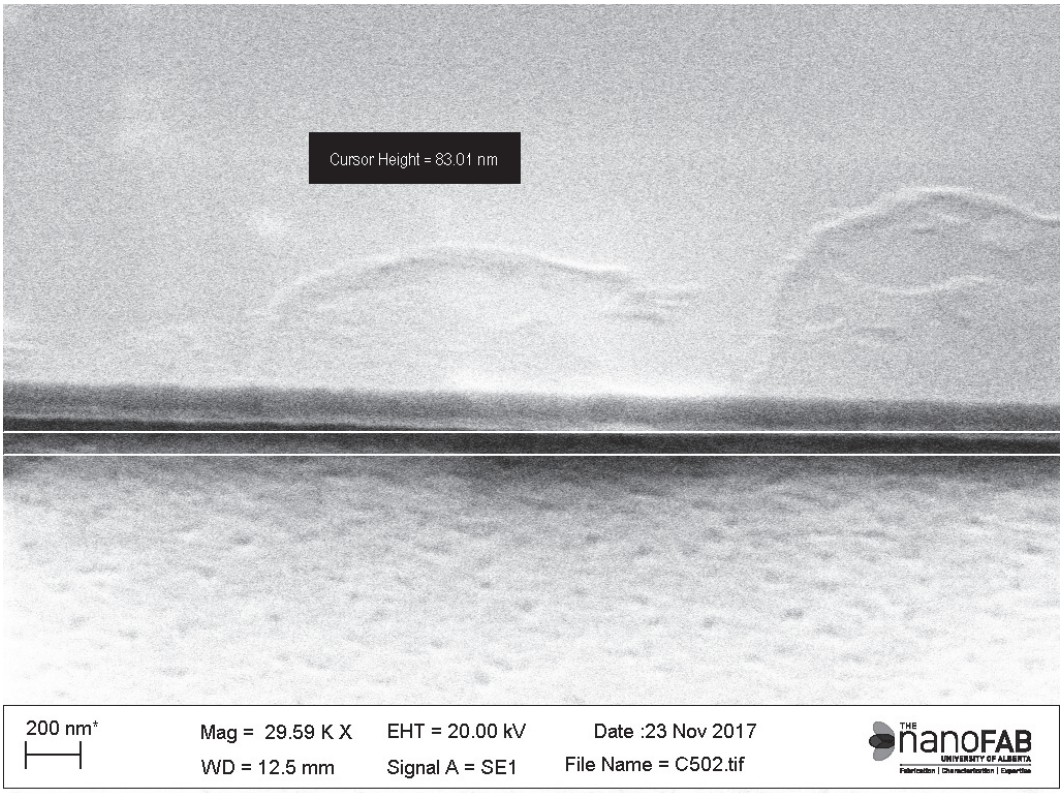

Figure 4.5: SEM image of Chip C.5, VHF etched at 10.5 Torr, for 200 s, reduced contamination observed compared to chips etched at 13 Torr, but not eliminated

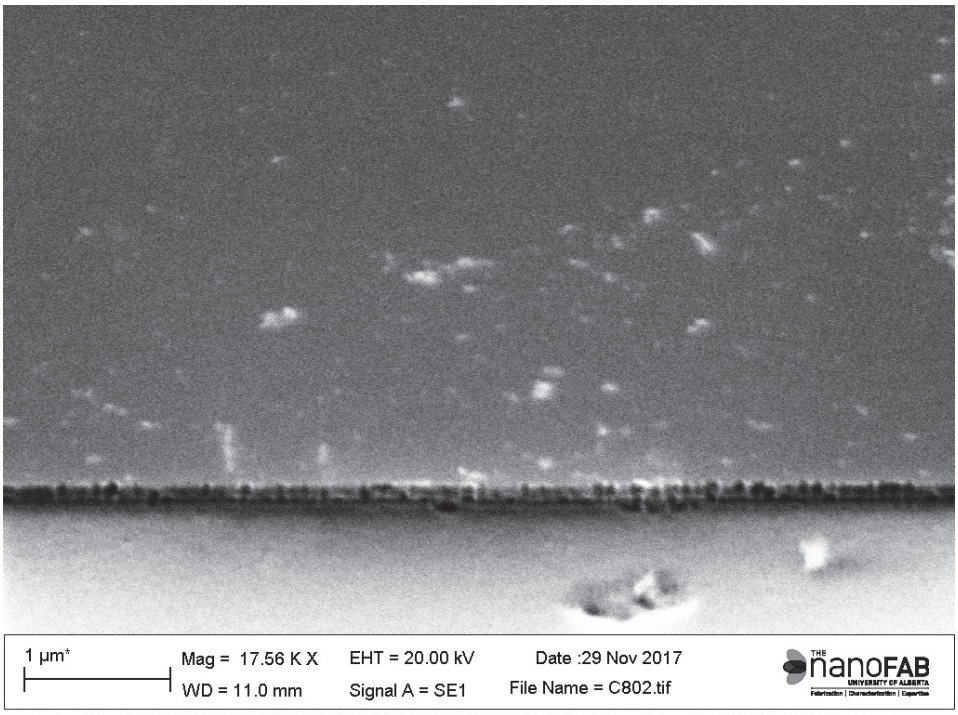

(a) SEM image of Chip C.8, VHF etched at 10.5 Torr, for 175 s

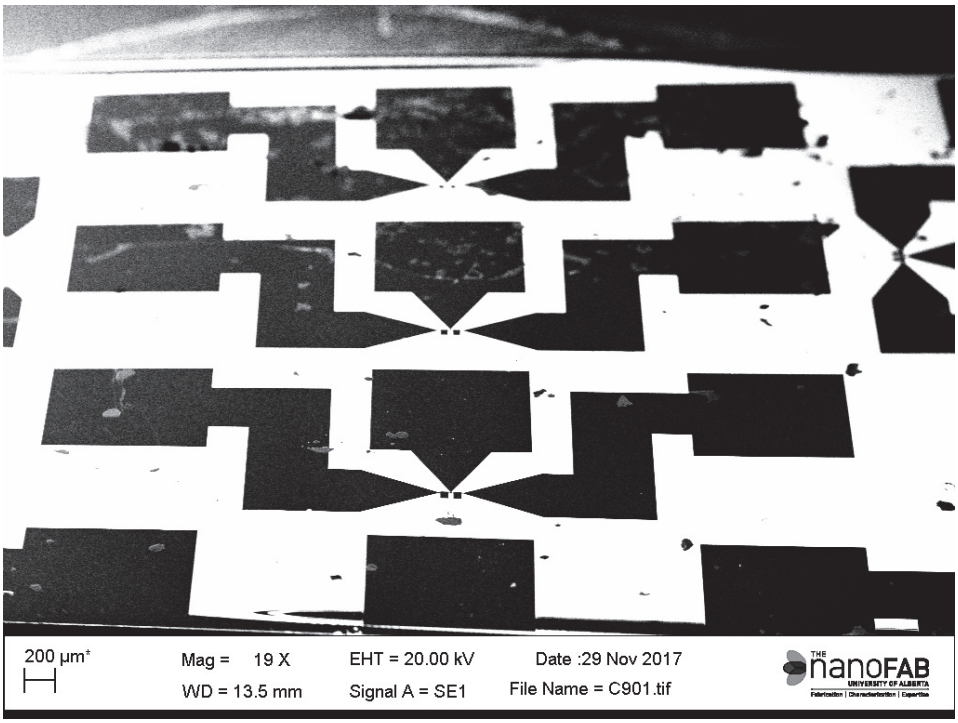

(b) SEM image of Chip C.9, VHF etched at 10.5 Torr, for 225 s

Figure 4.6: SEM images comparing contamination during VHF tests performed at 10.5 Torr. Reduced contamination observed, but not eliminated at 10.5 Torr when compared to higher pressures. No appreciable difference in contamination between the two chips despite the difference in etch time. Magnification is shown as different between the two figures to demonstrate scale of residue.

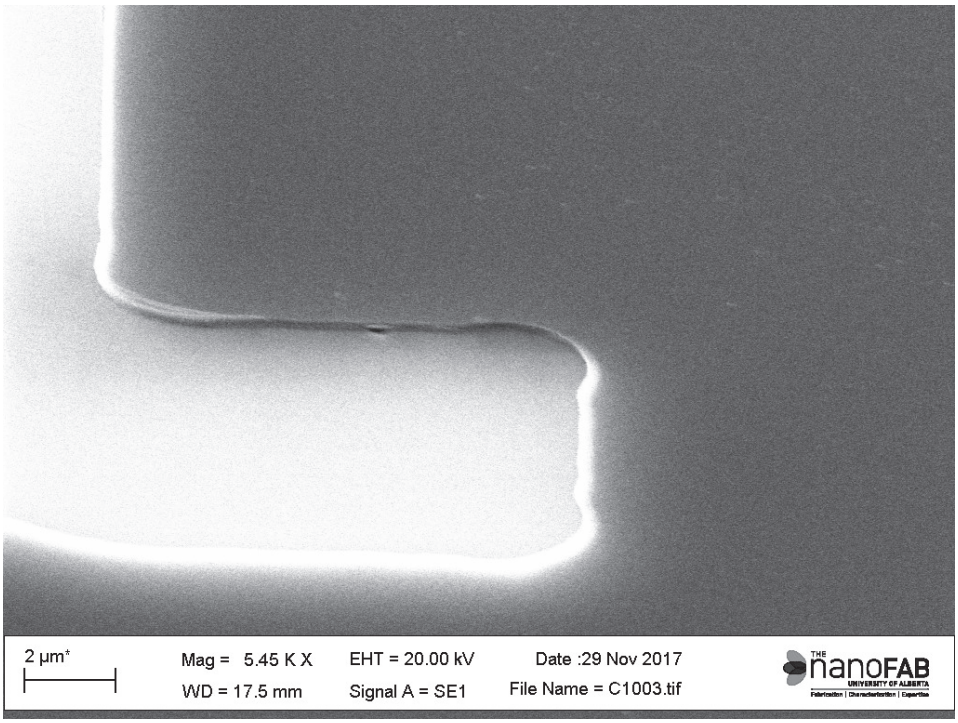

(a) SEM image of Chip C.10, VHF etched at 10 Torr, for 175 s

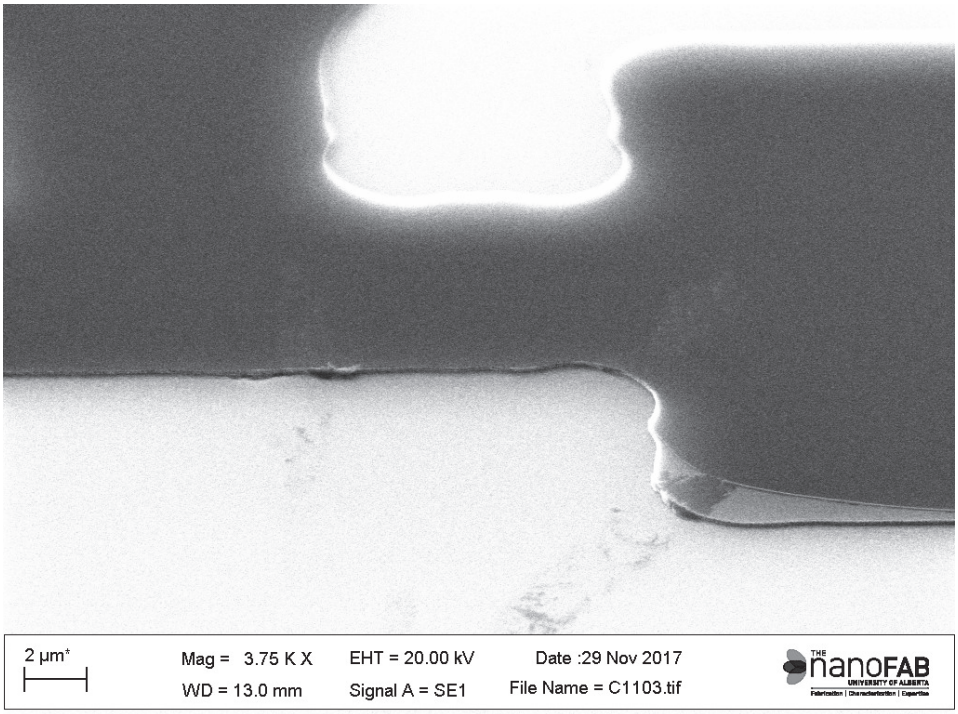

(b) SEM image of Chip C.11, VHF etched at 10 Torr, for 225 s

Figure 4.7: SEM images comparing contamination during VHF tests performed at 10 Torr. Reduced contamination observed at 10 Torr compared to 10.5 Torr. No appreciable difference in contamination between the two chips despite the increase in etch time.

eliminated at this point. User error was made on the input of recipe time on C.13. The data was still included as the previous tests were suggestive that the length of the etch did not have an appreciable increase on the residue present on the surface post etching. Now that the etch rate was established, a etch time to reach approximately 500 nm depth was needed. (Please note that chips labelled C.14 and C.15 are correct as given in the tables). No residue was observed on C.15 as shown in Fig. 4.8. The etch depth was estimated based on SEM imaging.

Chip	Pressure [Torr]	Time [s]	Water [mgpm]	Observations
C.12	10.5	175	7	More reduced residue
C.13	10.5	225	6	Reduced residue
C.15	10	175	8	No residue

Table 4.5: Test 4: VHF Water Test

Once contamination was eliminated, and shown to be a result of VHF processing parameters, the process needed to be calibrated to etch to a depth of 500 nm. Previous tests showed that contamination for the chips was eliminated at pressures below 10 Torr, and above 8 mgpm water flow. Earlier tests showed that both of these parameters had an effect on the overall contamination level. However, it showed that the etch rate at lower pressures is slower compared to higher pressures, as theory would indicate (Table 4.1). These two variables (water flow and overall system pressure) should not be arbitrarily increased as uniformity will suffer as a result. Etch times were varied as per Table 4.6. SEM imaging, shown in Figs. 4.9 and 4.10 confirmed the elimination of residue.

Chip	Pressure [Torr]	Time [s]	Water [mgpm]	Observations
C.14	10	300	8	Etched 104 nm
C.16	10	400	8	Etched 150 nm
C.17	10	500	8	Etched 235 nm

Table 4.6: Test 5: VHF Time Test 1

With rates approximated, to conclude that both pressure and water have an effect on residue, one chip (C.19) will be run at 11 Torr but similar water

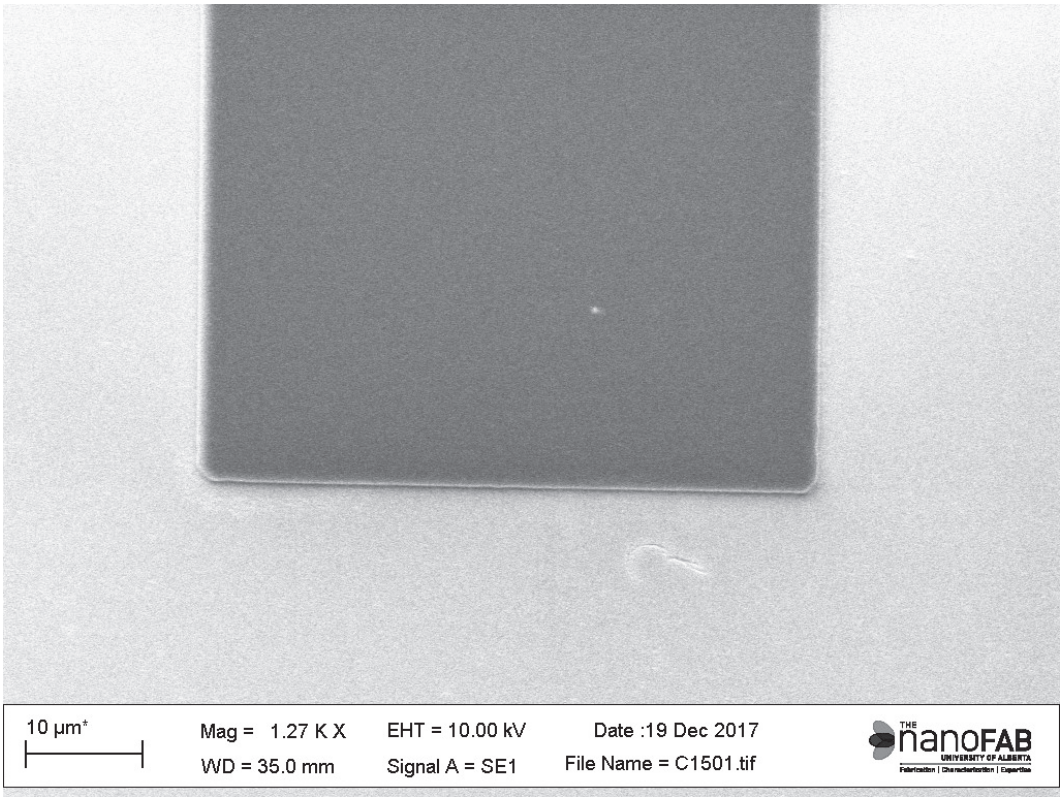

Figure 4.8: SEM image of Chip C.15, VHF etched at 10 Torr, for 175 s, 8 mgpm H_2O, contamination eliminated.

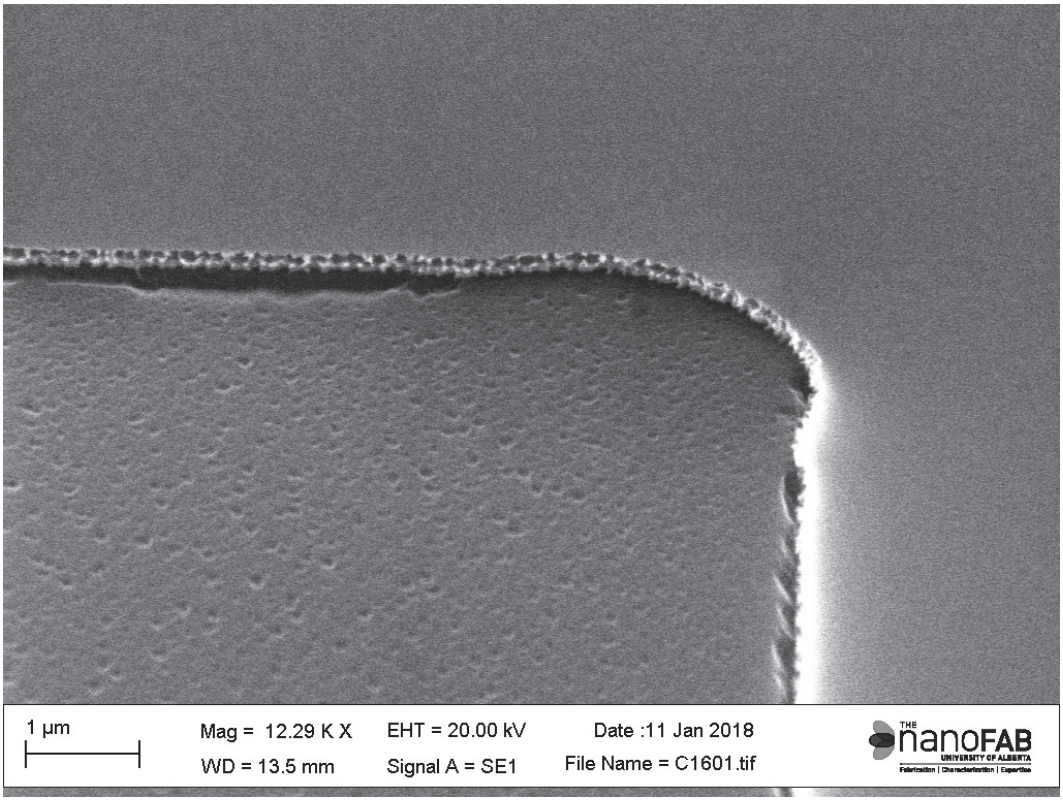

Figure 4.9: SEM image of Chip C.16, VHF etched at 10 Torr, for 175 s, 8 mgpm H_2O, approximate etch depth: 199 nm

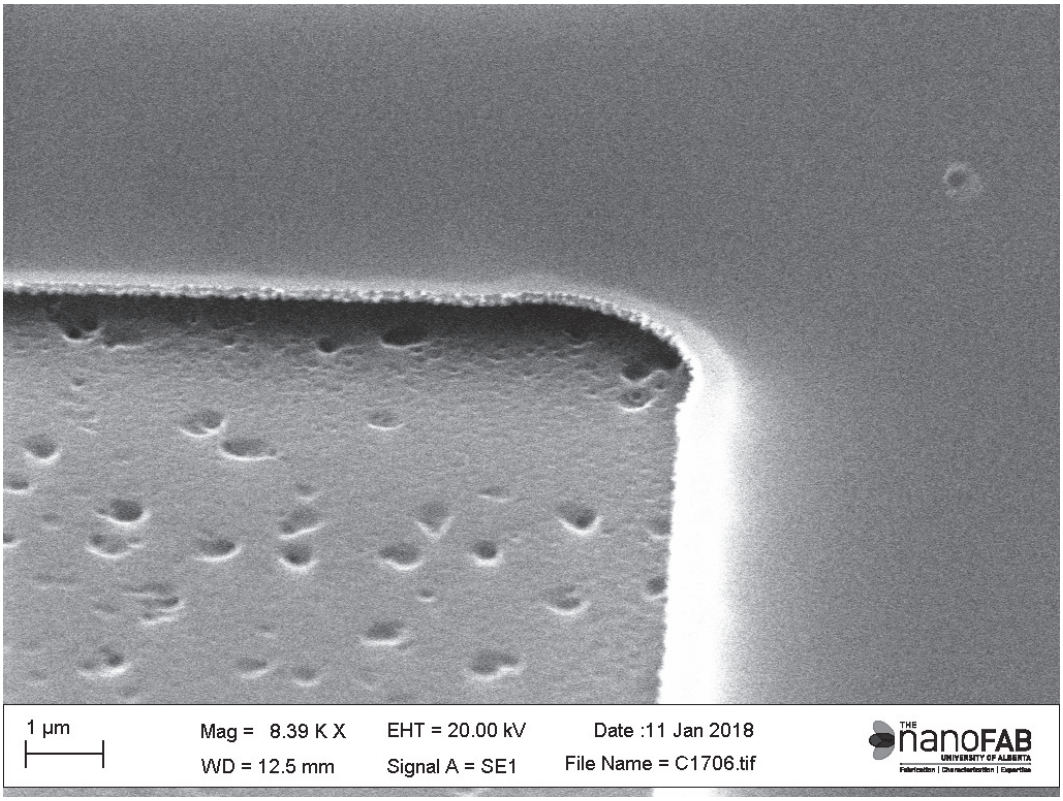

Figure 4.10: SEM image of Chip C.17, VHF etched at 10 Torr, for 500 s, 8 mgpm H_2O, approximate etch depth: 217 nm.

to achieve similar etch depth. The contamination was again present at the higher pressure of 11 Torr, leading to the decision to only etch at 10 Torr for these chips despite the increase in etch rate at higher system pressures. The parameters for this round of testing is shown in Table 4.7.

Chip	Pressure [Torr]	Time [s]	Water [mgpm]	Observations
C.18	10	1050	8	Etched 490 nm
C.19	11	750	8	Etched 489 nm, contamination present
C.20	10	1400	8	Etched 490 nm*

Table 4.7: Test 6: VHF Time Test 2

C.20 was etched in two steps due to user error, with the combined times leading to a satisfactory etch depth. Breaking vacuum did not increase the contamination with respect to similarly process chips. VHF provides the unique opportunity to etch further if the initial etch depth was insufficient, something that would be incredibly time consuming and impractical to do with BOE and CPD. There was negligible observed effect on the chip being etched in two stages, a perfect example of how forgiving VHF processing can be compared to BOE and CPD.

Final testing to verify parameters was conducted as per Table 4.8. These tests showed that uniformity may be suffering, but contamination on the chips poses a greater threat to performance as VHF release is performed immediately before metallization, with no wet cleaning step being possible in between. Chip C.23 was used as an additional verification that top-up etching was reasonable with this process. Based on other data, chip C.21 was likely an outlier. As thickness was approximated based on SEM imaging, there is a reasonable margin of error on the etch depths measured. SEM imaging of the final test chip in Fig. 4.12 is shown compared to a successfully released cantilever in Fig. 4.13. The final parameters chosen for this process were an etch time of 1400 s and a water flow of 8 [mgpm].

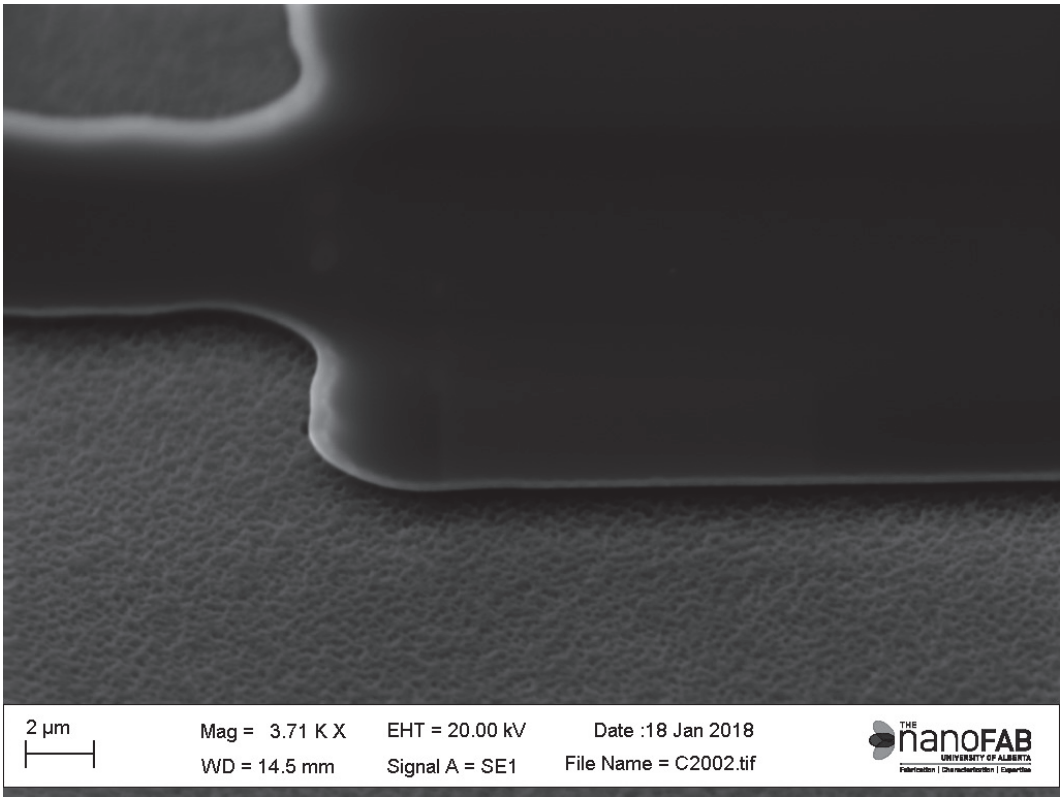

Figure 4.11: Chip C.20, VHF etched at 10 Torr, for 1400 s, 8 mgpm H_2O, approximate etch depth: 490 nm.

Chip	Pressure [Torr]	Time [s]	Water [mgpm]	Observations
C.21	10	1400	8	Etched 347 nm
C.22	10	1450	8	Etched 430 nm
C.23	10	1000 + 400	8	Etched 400 nm then 506 nm
C.24	10	1350	8	Etched 479 nm

Table 4.8: Test 7: VHF Final Test

The finalized process step was able to release the devices with minimal, if any contamination introduced. The etch depth was satisfactory to allow for oscillation of the devices. The process was run very quickly in a single batch on the actual test devices due to the ability to etch a large batch of chips at one time. The etch depth remained at approximately 500 nm even with the marginally increased surface area of the cantilevers. Some uniformity was sacrificed for an etch with reduced contamination. At some points near the edges of features, pitting was observed; likely a problem related to fluid mechanics and diffusion of reactants. As stated earlier, water is a critical catalyst in the process. If the water is unable to diffuse efficiently out of confined spaces, such as in constricted areas like the edges of features, localized increased etch rates could occur. Any pitting observed was only found at the edges of features and did not extend enough under the contact pads or cantilevers to have concerns of reduced structural integrity. Results showed in Chapter 6 that chips with observed pitting at the feature edges were still functional. The large size of the contact pads means that loss of structural integrity due to localized over-etching is improbable. Reducing the contamination which could have a very detrimental effect on the adhesion of the metal layer increased the overall yield of these devices when compared to previous work.

In previous work, often more than half of the chips would be lost at the BOE and CPD stage of the process flow [5, 14]. Changing to the VHF process improved yield substantially, as no chips were lost due to poor release or organic contamination from the shared CPD chamber. The work done to optimize the VHF process was very beneficial to final chip yield.

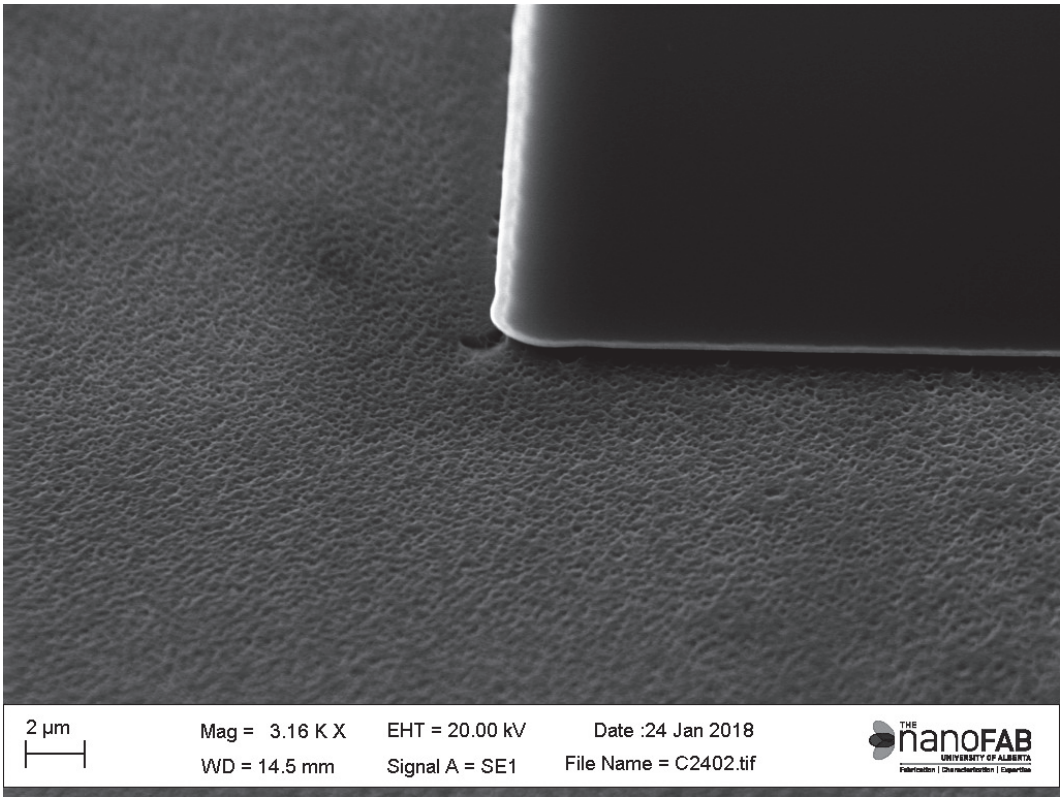

Figure 4.12: Chip C.24, VHF etched at 10 Torr, for 1350 s, 8 mgpm H_2O, approximate etch depth: 479 nm.

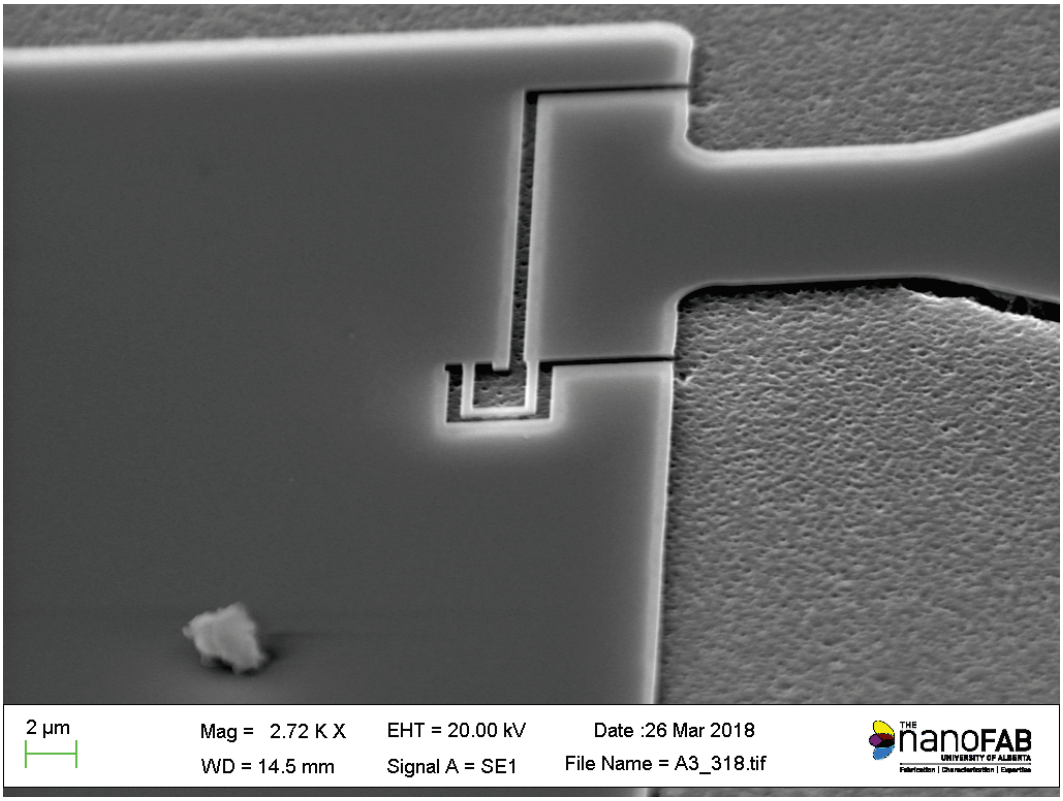

Figure 4.13: Chip A.3, VHF etched to a comparable amount to C test chips.

Chapter 5

Device Testing and Magnetomotive Approach

Work done by previous students (H. Brausen) in the Engineered Nanomaterials Laboratory led to the creation of the electronic balancing system used for device testing in this thesis. This author added to and built some of the elements of the testing apparatus used. This chapter will detail how the system operates to allow for actuation and measurements of the magnetomotively actuated cantilever devices.

5.1 Device Testing and Magnetomotive Setup

The testing apparatus, shown in Fig 5.1, had several key components to its operation:

1. A network analyzer for measurement of the resonant frequency of devices.
2. The ENL designed balancing circuit used to locally reduce background noise for the signal.
3. A Halbach array for a 1 T magnetic field within which the devices under test are placed.
4. A chip holder and pin assembly for securing the test chip inside the Halbach array and for making electrical contact with the contact pads on the chip.

5. A vacuum chamber for hosting the Halbach array, balancing circuit, and chip holder assembly. It also allows for controlled pressure and in future work, introduction of test gases.

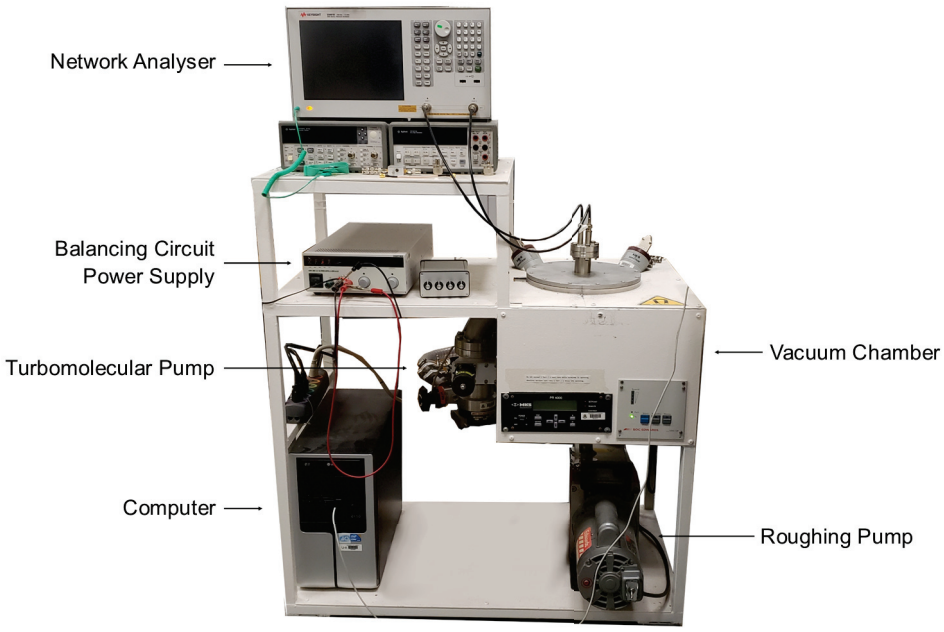

Figure 5.1: Photograph of the entire testing assembly including vacuum chamber, network analyzer and balancing circuit.

A diagram depicting the simplified electronic setup is shown in Fig. 5.2. The network analyzer is connected to a computer with LabVIEW software for interpreting the data obtained from the system. The details for this system will be discussed throughout the chapter, the diagram is included here to provide a visual reference for the reader for the coming discussion.

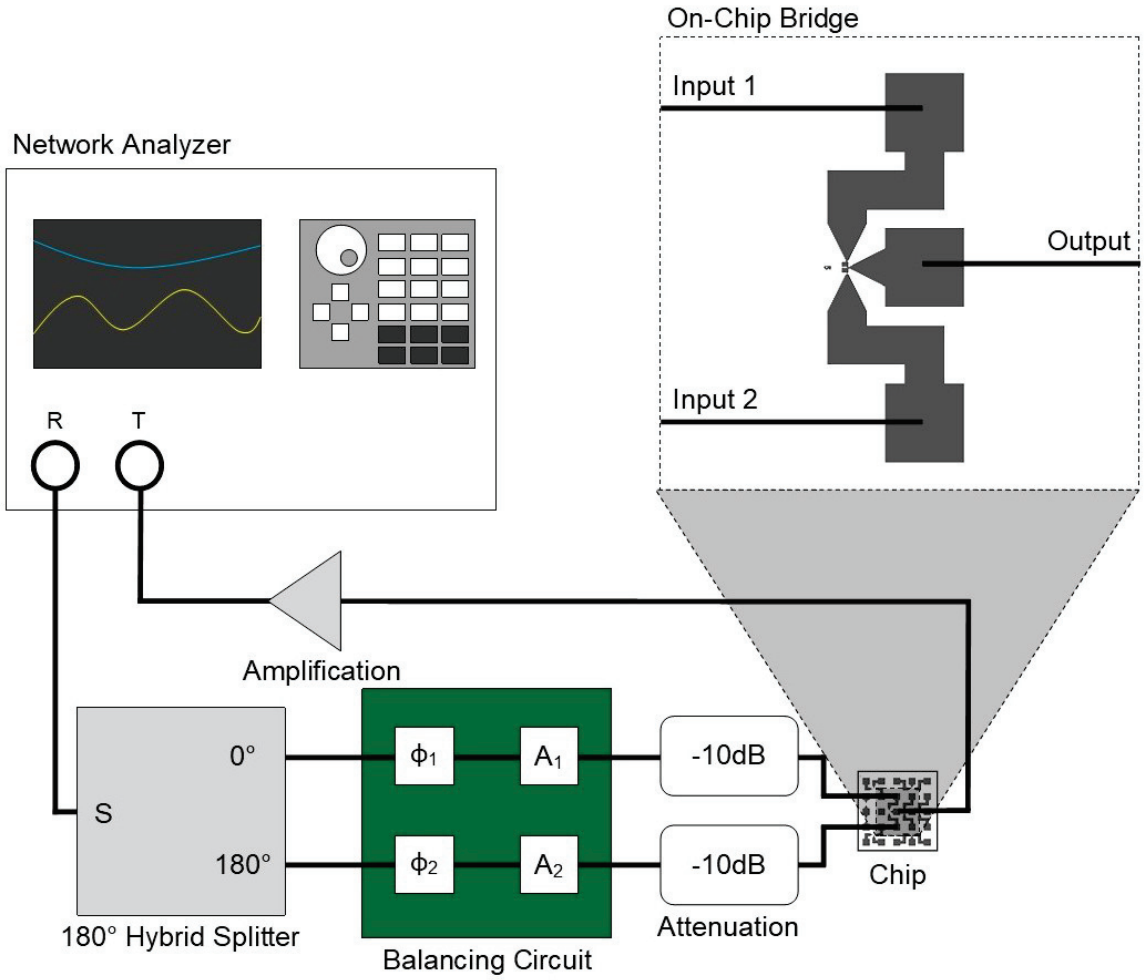

Figure 5.2: Diagram showing the set up with the balancing circuit, network analyzer and on-chip bridge.

5.1.1 Network Analyzer

The network analyzer used was a Keysight E5061B, capable of RF signal generation. This system is capable of operating at the high frequencies required for the measurement of the devices. The driving signal for the devices is passed through RF coaxial cables through a feedthrough in the vacuum chamber lid. From there, the signal is sent through a 180° hybrid splitter. The splitter generates two approximately anti-phase signals. Theoretically the two signals should be fully anti-phase, however, in practice there is always some small magnitude or phase errors; which is key to the approach used in this work.

From there, the signal enters the balancing circuit.

5.1.2 Balancing Circuit

The balancing circuit used in the lab was created by H. Brausen and J. Sit, and published in "A Bridge-Balancing Circuit for Balanced Measurement of Resonant Sensors" [3]. A balancing system can significantly reduce the background noise in a system [3]. By locally reducing the background noise near where the expected frequency response for a given device is, the easier it is to detect the device resonance [40].

Other techniques exist for measuring MEMS cantilever devices. However, there are benefits and draw-backs to any given approach. Traditional optical read-outs of resonance are not as readily integrated into fully packaged systems [10, 11]. Piezoresistive methods introduce a large electrical resistance to the circuit, effectively creating a low-pass filter, which may swamp out a small measurable response [11] [41]. Parasitic capacitances present in both the chip and testing apparatus make detection of the signals difficult before the implementation of this set-up. The balanced bridge measurement technique reduces background noise and parasitic capacitances [3, 9]. When the devices are in resonance, the signal can be manually balanced and amplified to be more easily detected from against a lowered noise floor.

In order to work, the bridge itself needs to be balanced when out of but near resonance. Imbalance in the system, introduced in a variety of ways, leads to background noise, making detecting device resonance difficult, if not impossible [3]. Mismatch in cable length, wire dimensions, connectors, any device asymmetry or any physical variation between the two signal branches physical setup is unavoidable in real-world applications. In a theoretical and perfect system, if the two cantilevers were perfectly symmetrical and the system also perfect, when the signal recombines on the chip, the two anti-phase signals would cancel each other out. But the inherent mismatch allows for the signal to be measured on the output.

It is needed to fine tune the amplitude and phase of the driving signals in order to minimize the background signal [3]. By reducing the background

signal, the signal-to-background-ratio is improved by 25 dB [3, 5]. Otherwise, as discussed, in an idealised scenario, the two signals would cancel each other out when recombined on chip, and the signal would not be detectable. With the output signal at the common port much closer to zero, this lowers the background significantly, allowing for easier detection of the resonant response. An image of the balancing circuit is shown in Fig. 5.3.

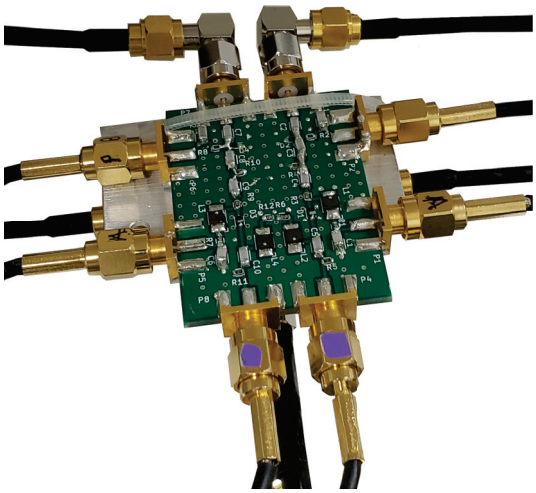

Figure 5.3: Balancing circuit as developed by the ENL group [3]. Each branch of the signal from the hybrid splitter enters the balancing circuit from the cables at the top of the diagram. From there, the signal passes through two mirrored phase and amplitude branches for manual balancing. The signal then exits the circuit through the two cables at the bottom of the diagram (labeled in purple) to be passed through the device.

The balancing circuit is used by manually adjusted the phase and amplitude of each signal branch to locally minimize the background noise near an expected signal response. The balancing circuit introduces a finely adjustable phase delay and attenuation on the two signal branches. When the device is out of resonance, but reasonably near the expected resonant frequency, the circuit is used to "tune" the setup to maximize signal cancellation at the output port. This brings down the background noise, so that when the device is in resonance the signal is more readily seen and measured.

After the circuit, a 10 dB attenuator is used on each signal branch to improve isolation between the circuit and device [5] [3]. Each signal branch

will pass through two mirrored cantilever structures, before recombining on the output branch of the device. Once recombined, the signal returns to the network analyzer for analysis, shown in Fig. 5.4.

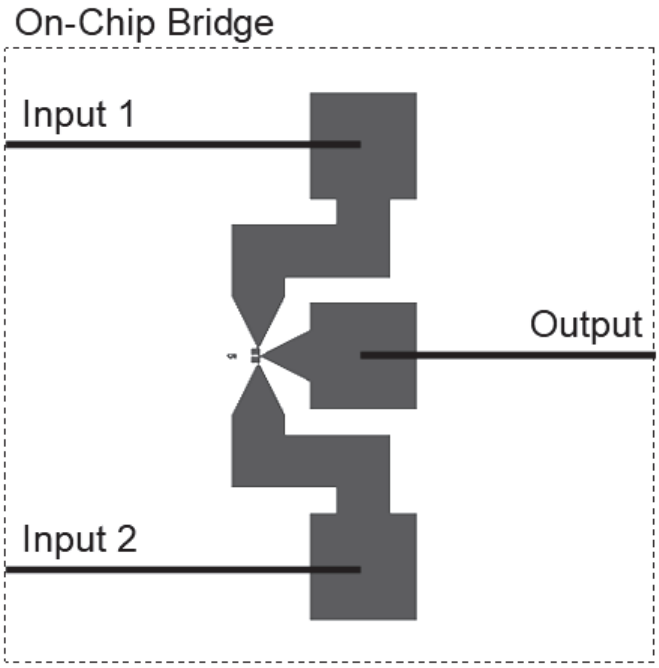

Figure 5.4: A diagram depicting the signal recombination through the two branches of device. Anti-phase drive signals are introduced at the input ports, which should theoretically cancel each other out before reaching the output port. However, mismatch in the signal unavoidable in real world application leads to a detectable signal on the output port.

5.1.3 Halbach Array

Superconducting magnets have been used traditionally for magnetomotive actuation [10,11]. Superconducting magnets are capable of generating static and uniform fields of variable strength, in some cases up to 8 Torr [9]. Some groups were successful in their actuation of high frequency devices up to 200 MHz [9]. However, these magnetic assemblies are extremely expensive in the context of a small research lab. There was a need to find a solution to an affordable magnetic assembly that would produce a strong, stable and uniform magnetic

field that is reasonably resistant to demagnetization.

When looking into implementing an electromagnetic system, there are several considerations. First: electromagnets need power to be magnetised. This adds to the cost of running the assembly in electricity. The system often needs cooling loops to prevent overheating, adding to the running cost of the tool. The more parts to a system, especially with water cooling systems, the more maintenance costs associated to keep them running. Additionally the overall cost of these systems, with all the needed components can easily run over $ 10,000 CAD. These costs only increase with time with electricity and maintenance [42, 43]. The large benefit to these systems is the ability to change and control the strength of the magnetic field. As stability of the field matters more to the application shown in this work, being able to control the strength of the magnetic field is superfluous for the added cost. The permanent magnetic apparatus has a much lower starting cost (generally thousands of dollars [44]). The magnetic assembly also will never need maintenance, electricity or any added costs once implemented, significantly reducing the financial burden for the system.

It was chosen to use a Halbach array of 8 NdFeB rare-earth magnets capable of generating a uniform 1 T field of 30 mm in inner diameter and 40 mm height [5]. This size was sufficient for a small carrier to be made that would hold the 10 mm square chips securely, while still maintaining the smallest reasonable volume. It is important when designing a system that will be operated under vacuum to have a minimal size, as the larger the chamber required to hold the testing assembly, the more volume of gas there is to pump down. As well, the larger the chamber size, the higher the internal surface area, which in turn means more amount adsorbed gas on these surfaces. Water vapour (in particular from the natural humidity in the air) can adsorb easily to the chamber walls but desorbs slowly compared to other gases present in air, increasing system pump time.

A Halbach array is created by rotating the direction of magnetic field on each permanent magnet, creating a one sided flux, with the magnetic field concentrated on one side of the assembly, and near zero on the other. This

also allows for additional safety, as the magnetic field is near 0 outside of the ring of permanent magnets, preventing attraction of unwanted ferromagnetic parts into the magnetic assembly. A diagram depicting the field direction for a Halbach array is shown in Fig. 5.5.

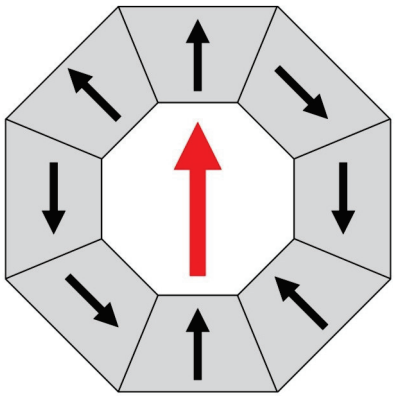

Figure 5.5: Diagram of Halbach array orientation of NdFeB magnets used during testing. The black arrows indicate the magnetic field direction for each magnet. The red arrow indicated the overall produced 1 T magnetic field in the center of the assembly.

Unlike electromagnetic systems, a permanent magnet assembly is always "on", and cannot be switched "off" by cutting off the current supplied to the system. The passive nature of the permanent magnetic assembly means little to no maintenance or upkeep is required to maintain a stable, uniform permanent magnetic field. Provided the magnet does not exceed its Curie temperature, the temperature at which magnetic properties of a magnetic material change, the magnet will stably provide a magnetic field indefinitely. The Curie temperatures for these types of magnets are well above normal operating temperatures, at approximately 300 °C, depending on the manufacturer [45] [46].

This system is of comparatively lower cost compared to other methods, such as electromagnets [5]. Any free floating device with an appropriate current running through it could theoretically be tested in this system, allowing for a diversity of testing applications and device on-chip configurations. This

assembly could allow a research group to do rapid prototyping of simple devices, which is incredibly beneficial in functionalization research.

Safety is important in a design with permanent magnets, as the magnetic field is always present. Retaining brackets were made out of Al and the vacuum chamber used was manufactured out of austenitic stainless steel to prevent damage to the system by attraction to other ferromagnetic parts of the system.

Using a system with a lower magnetic field would require an increase in current running through the devices to achieve the same amplitude of response from the sensor. Greater current would result in more heating of the wires, balancing circuit and devices themselves [5, 10]. In addition to shifts in behaviors due to temperature changes, heating of the devices lowers the quality factor of the device due to the increase in damping and overall energy lost per cycle.

With this comparatively low cost system in place, different designs of cantilevers, or other magnetomotive MEMS/NEMS devices can be made and tested with little to no change required for the testing apparatus. For testing configurations and frequency responses for varying sizes and shapes of cantilevers, having a system like this is advantageous. The permanent magnetic assembly/Halbach array is shown implemented in a vacuum chamber in Fig. 5.6.

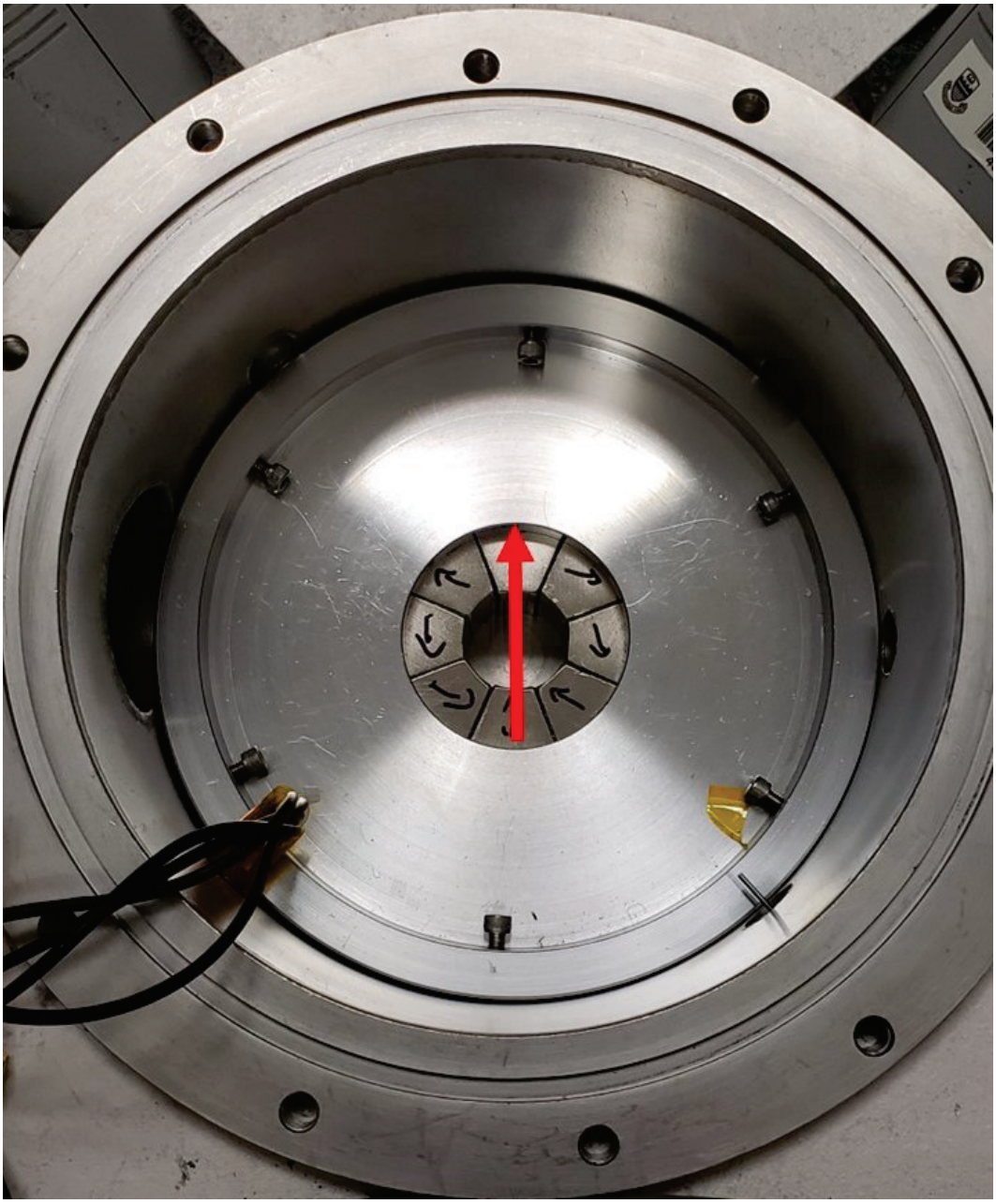

Figure 5.6: Photograph of Halbach array implemented in vacuum chamber. The black arrows indicate the magnetic field direction for each magnet. The overlaid red arrow indicates the overall direction of the magnetic field.

5.1.4 Chip Holder and Assembly

As stated earlier, the drive signal from the network analyzer is connected to a 180° hybrid splitter. The output signals from the splitter are then passed through the balancing circuit designed by the ENL lab followed by 10 dB

attenuators [3]. The signals, carried by two coaxial cables, are connected to a multipin electrical feedthrough on lid of the vacuum chamber. The signals are connected to a brass pin assembly that makes contact with the chip itself. The brass pins are spring-loaded and apply a small pressure to the surface of the contact pads, ensuring good electrical contact.

This author built the wiring assembly for the pins to be able to test all devices on the chips while keeping the chip clamped in its holder, as compared to the two of previous work. This allowed for testing of more devices per chip. Having more devices to test per chip gave more robust data per chip. This also allowed for the testing of devices of different sizes within one chip itself, rather than varying the lengths on each chip to be tested. The pin assembly is shown in Fig. 5.7. The 5 x 5 array allowed connection of eight separate sets of devices per chip for testing in the balanced-bridge configuration. Each device required three pins: two anti-phase inputs and one output.

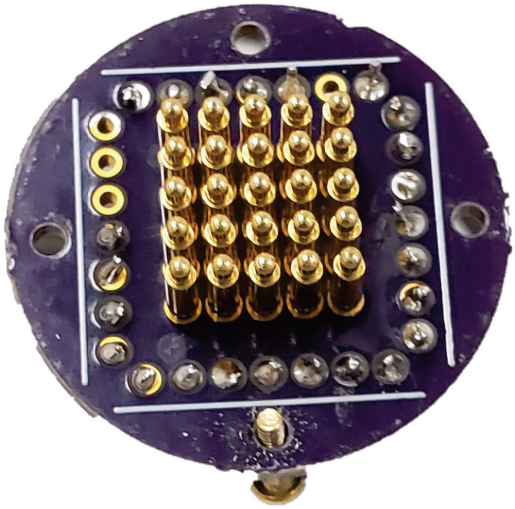

Figure 5.7: Pin assembly to connect contact pads to circuit. For eight devices, a total of 24 connections are required, leaving one pin unused.

The chip holder fits into the Halbach array in the bottom of the vacuum chamber. The chip holder is pictured in Fig. 5.8. The brass pin assembly with the wiring connections is placed, pins facing down, onto the chip holder. Two pins are used for alignment, and two brass screws are used to secure the two parts together. The full assembly is placed into the Halbach array and the

wires are connected to the feedthroughs for the balancing circuit, the signal passes through each branch of the electrical traces and through the cantilevers. The signals are recombined on the output and the signal returns to the network analyzer after amplification. The signal can then be analyzed to determine the frequency response of the cantilever system.

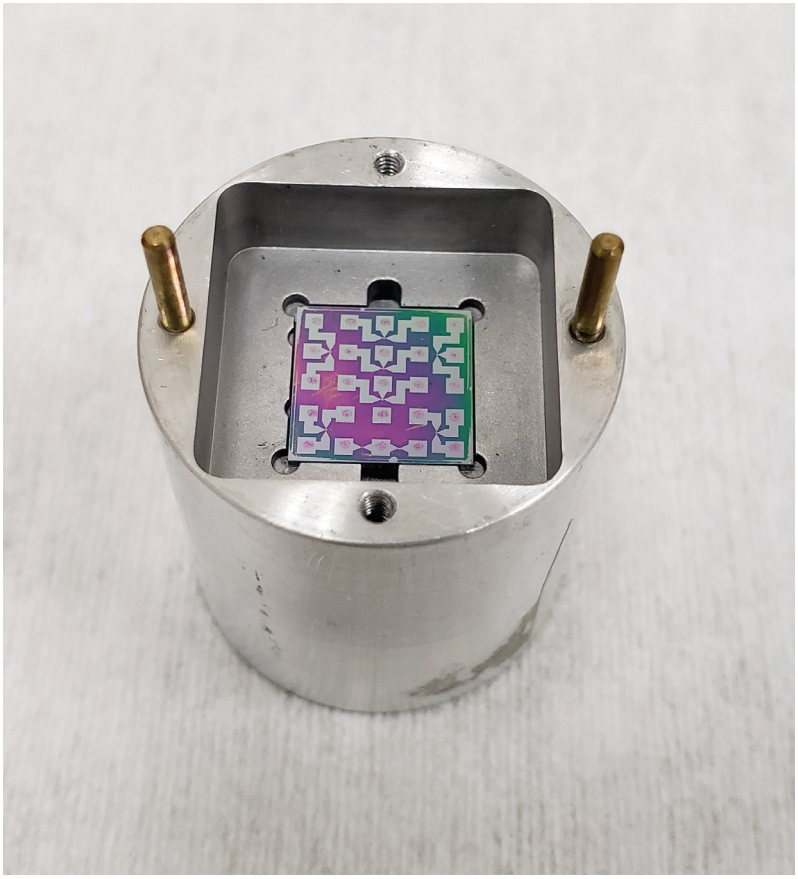

Figure 5.8: Chip holder used to connect to pins assembly that will be placed inside the Halbach array. A completed chip is shown inside the holder.

5.1.5 Vacuum Chamber

Operating the devices under vacuum, will reduce mechanical damping due to the viscous flow of air, allowing for resonance parameters to be determined without the effect of air damping [5,6]. This allows for the successful measurement of more devices, whose responses may have been otherwise lost to system noise due to limited quality factor (Q). The system is capable of pressures that range from atmosphere to less than 1 mTorr. To achieve this, the system uti-

lizes a turbomolecular pump, backed by a roughing pump. The chamber is vented using a dry nitrogen line, allowing for variable-pressure environments, enabling the option of testing the devices with air damping present. For detection in different gaseous environments, the system could be later adapted to allow for different gases besides nitrogen to be introduced to the testing chamber. The chamber pressure is measured with two capacitance manometers, which, in combination, are capable of measuring pressures from 1 mTorr to 1000 Torr. Each measures at a different pressure range, requiring two to measure at lower pressures. Electrical connections are made using a multiconductor feedthrough on the lid of the vacuum chamber, and attached to a balancing circuit, and network analyzer.

5.2 Operation

With all of the components described a frequency response of the devices can be measured. The chip is fitted into the pin assembly as in Section 5.1.4. The brass screws are tightened, and the spring loaded pins make contact with all of the contact pads from the devices across the chip. The two input and one output wires for any given device are then secured to the balancing circuit and vacuum chamber feedthrough respectively (Section 5.1.2). The chip holder assembly is then placed into the Halbach array in the vacuum chamber such that the direction of the Halbach array will be perpendicular to the cantilevers (Section 5.1.3). The lid of the vacuum chamber is closed and the chamber is roughed out using the roughing pump followed by pumping with the turbomolecular pump (Section 5.1.5) until a pressure below 2 mTorr was reached.

Once the hardware is setup for testing the network analyzer can be prepared. A sweep was set up between 0 MHz and 200 MHz which is within the functional range of the balancing circuit. The sweep was chosen to have 500 data points and a delay of 60 ms. Power to the balancing circuit is then turned on, and the operator can begin to balance the circuit near where an expected frequency response may be. The phase and attenuation of each signal

branch is carefully balanced using four knobs until the noise floor is lowered near an expected frequency response. The sweep of the network analyzer is then shortened to only be within 10's of MHz of the frequency response to maximize data points for the response.

A response is detected by the network analyzer due to Lenz's law [47]. The Lorentz force equation is used to determine the force experienced by the beam in a magnetic field. However, due to Lenz's law, the magnetic field created by the current flowing through the device opposes the change in flux. The opposition of the current to the magnetic field leads to a detectable voltage difference in the network analyzer, causing a measurable resonance peak. It is important to note that in this testing apparatus, the devices are both driven and measured with the same set of wires. The ability to both drive the resonator and measure with the same set of wires, shows promise for scalability, and later packaging into a finished device. Other methods of determining the deflection and resonant frequency (such as optics) are not as readily scalable to a packaged device as the optical system must be out of plane of the sensor [10, 11, 14].

The following figures demonstrate a live example of the balancing circuit and overall system in action. Fig. 5.9 shows a signal passed through the system without the balancing circuit. Any signal could easily be missed due to noise. In the second figure, Fig. 5.10 shows the system with the balancing circuit tuned to approximately 110 MHz, within the ranges that a cantilever response could be measured. Fig. 5.11 shows a 4 μm long doubly clamped cantilever with a resonant response at 127 MHz. The noise floor is substantially lowered at this balancing point, making picking up a signal easier, as shown in Chapter 6. As shown in the figure along the red line, when the balancing circuit is not used, it would be impossible to see the resonant response.

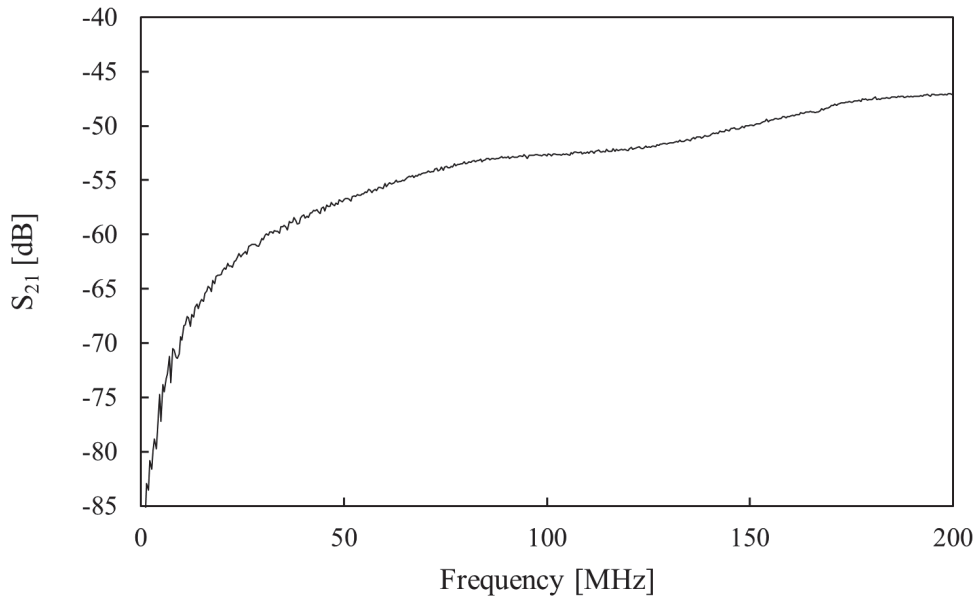

Figure 5.9: Plot of the response from the system with the balancing circuit not in use.

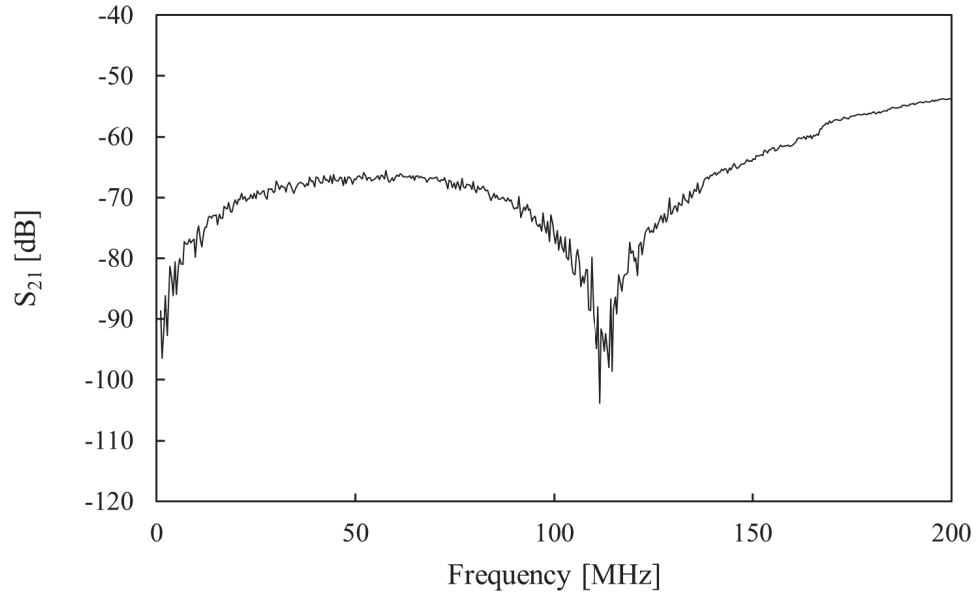

Figure 5.10: Plot of the response from the system with the balancing circuit balanced to 110 MHz.

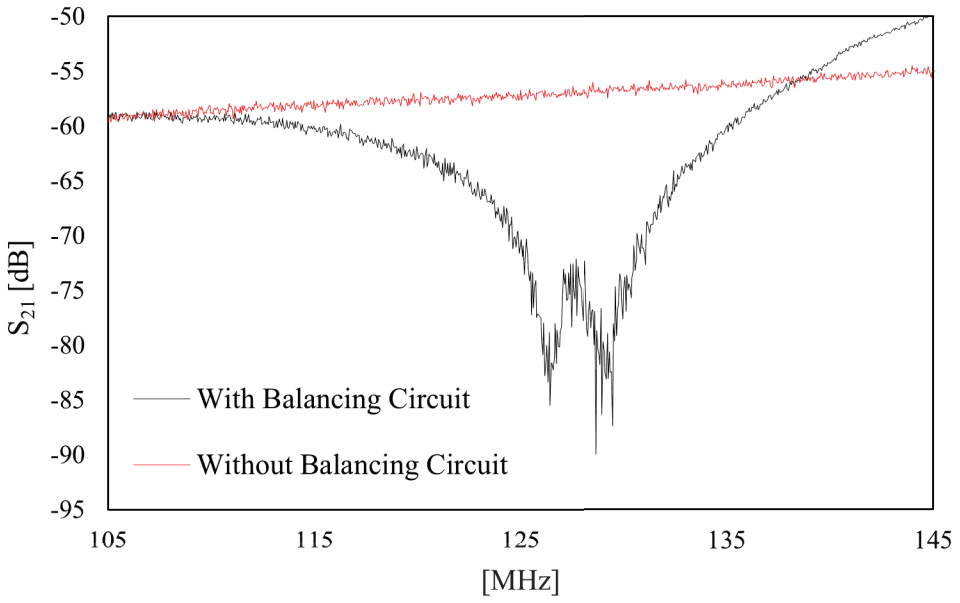

Figure 5.11: Plot of a 4 μm long doubly clamped cantilever with a resonant response at 127 MHz. The device was measured both with and without the use of the balancing circuit, and the results were combined in this plot.

In order to calculate the quality factor equation 2.3 from Chapter 2 is used. Re-included below:

$$Q = \frac{f_{res}}{\Delta f} \tag{2.3}$$

Where Q is the quality factor, f_{res} is the measured resonant frequency and Δf is the width of the plot at the full width half maximum of the peak. The height of the peak is defined by the minimum being set as the noise floor, where the balancing circuit brings down the noise to the minimum on the plot. Where the plot may be slightly uneven, an average was taken at the minimums on each side of the plot. This is roughly demonstrated in Fig. 5.12. This approach may been seen as conservative, and quality factors may be calculated higher if fitting a Lorentz to the curve. But this author chose to only use the measured data to calculate the quality factor rather than extrapolate to data outside of the range collected to fit a Lorentz curve, which may yield higher quality factors [5, 9]

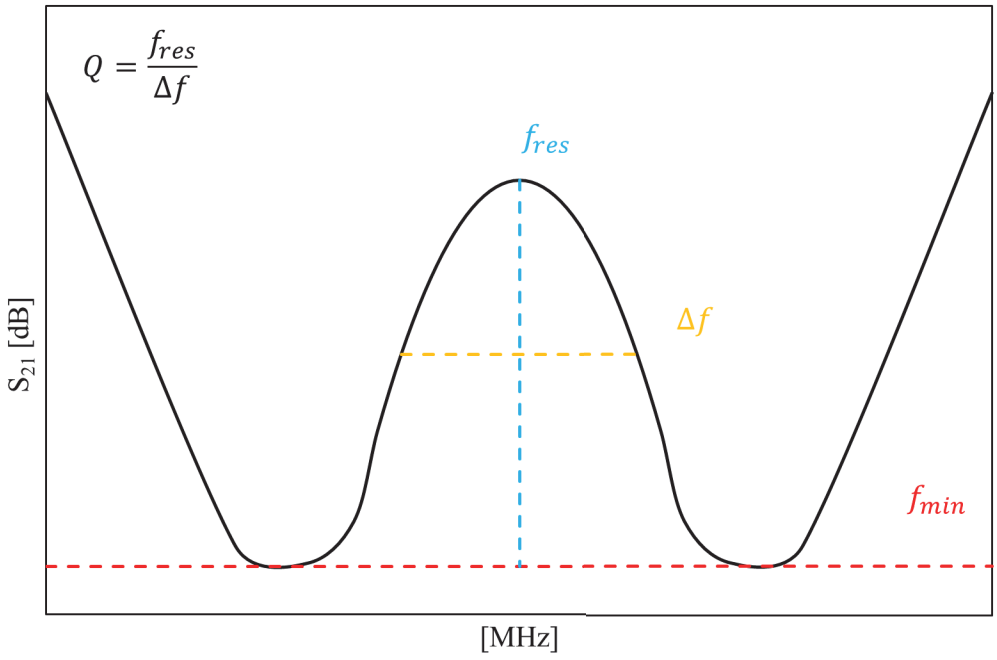

Figure 5.12: Plot of how the values were extracted from the resonance plot to determine quality factor.

The next chapter will discuss the implementation of the balancing circuit and testing assembly in the manufactured chips. This system is relatively low cost compared to other methods such as electromagnets [5]. This work serves to lower the bar of entry to other researchers looking for an inexpensive, accessible way to characterize and research MEMS cantilever devices.

Chapter 6

Results

The results obtained in this work serve to prove the efficacy of the use of the balancing circuit developed by the Engineered Nanomaterials Laboratory for quickly obtaining data for rapid prototyping of devices. The data set was obtained before the onset of the global COVID-19 pandemic. Because of the length of time devices had sat, it was determined that comparing results of newly fabricated devices to devices that had been idle should not be done. Contamination could have accumulated on the sensors in the time they were idle, which would alter the resonant response of the devices due to the added mass.

6.1 Theoretical Resonances

As determined in Chapter 2, the theoretical resonances from Eqs. 2.1 - 2.16 of devices is as follows in Fig. 6.1 and Fig. 6.2. The theoretical resonance of a device gives a starting point for a researcher to look for a response from the cantilever. The length is the factor that was varied between cantilevers. The balancing circuit is manually tuned once a current is running through the device to where an expected frequency response should be.

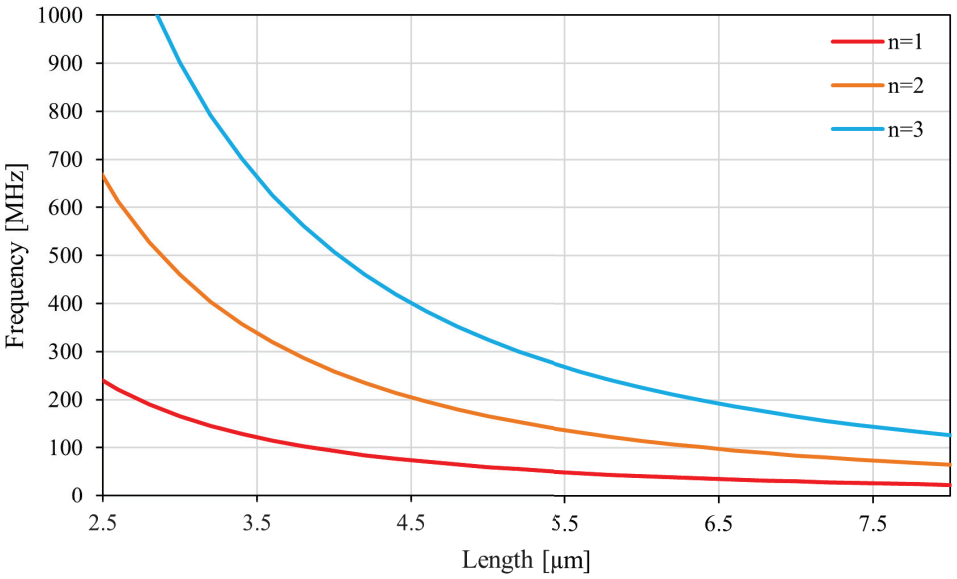

Figure 6.1: Theoretical resonant frequencies of doubly clamped cantilevers of varying lengths at n=1, n=2, and n=3

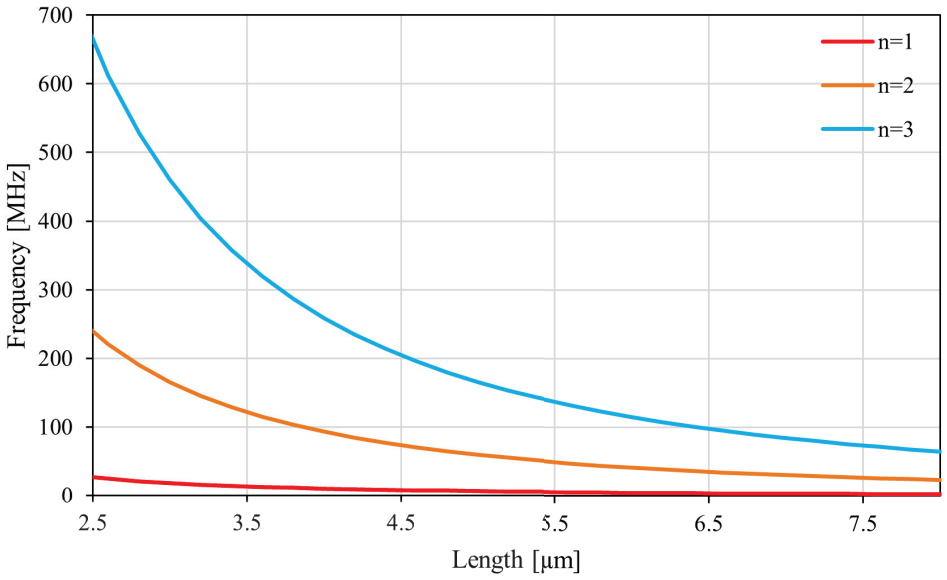

Figure 6.2: Theoretical resonant frequencies of "U" shaped cantilevers of varying lengths at n=1, n=2, and n=3

6.2 Results and Plots

The results obtained found that yield was improved significantly from previous work done by the group. All chips tested had working devices. The average

yield found across the doubly clamped devices was found to be 60%, while the yield from the "U" shaped cantilevers was found to be 58% with functioning cantilevers on every chip. In previous work many chips did not have any working devices, or only one or two functional across the entire chip. In initial development done by J. Westwood, yield of the devices above 7 μm in length was found to be above 86% . However for smaller devices, less than 7 μm, such as the range in this work, the yield was 0% [14]. For the "U" shaped cantilevers in H. Brausen's work, average yield was below 31% for chips that survived to the testing stage [5]. During the BOE and CPD release more than 50% of chips were lost due to failures in processing and were not counted towards yield. Other groups report large chip losses during a BOE and CPD release that improved to below 60% after implementation of VHF [36] [48]. Higher yields are reported in cantilevers with much larger dimensions than presented in this work [49] [50]. However, the smaller the device, the more difficult the fabrication will be.

The work done to optimize the process flow significantly increased the yield of devices. Additional work done by the author to expand the pin apparatus (Fig. 5.7) discussed in Chapter 5 lead to greater ease of testing all devices across any given chip without needing to re-land probes during each test, which could scratch the surface of the chip. The Ti adhesion layer introduced by this author also led to greater robustness of the chips when re-testing and re-attaching the probes to the chip.

6.2.1 Doubly Clamped Cantilevers

Included here is the plots obtained from the testing of the doubly clamped cantilevers. To obtain the results, the balancing circuit was used to lower the noise floor near where an expected response would be. If a response was found, the frequency peak was observed for several minutes (where possible) to ensure confidence in the response. Data was collected at this point. After searching for any other frequency peaks, the circuit would be re-balanced at the measured response to verify its validity as a data point. Comparing within the same chip (Chip 1: Fig. 6.3, Fig. 6.4, and Fig. 6.5) shows that for the 3.5 μm, 4 μm, and

5 μm cantilever, the overall quality factors were within similar ranges. The highest Q factor was measured on the 4 μm cantilever, showing that quality factor was likely unaffected by the cantilever length in this range. Quality factors and resonances agreed with other groups performing similar work in the same frequency range, although higher Q factors are possible [47] [51] [40]. SEM images taken from chip 2 of the doubly clamped cantilevers is shown in Fig. 6.6 and Fig. 6.7.

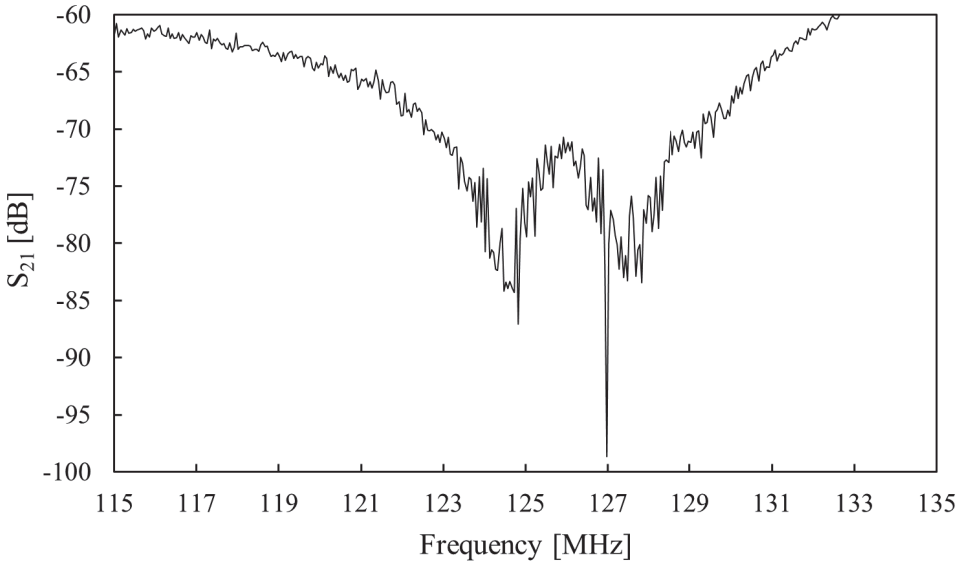

Figure 6.3: Plot showing the resonance of a 3.5 μm long doubly clamped cantilever from chip 1

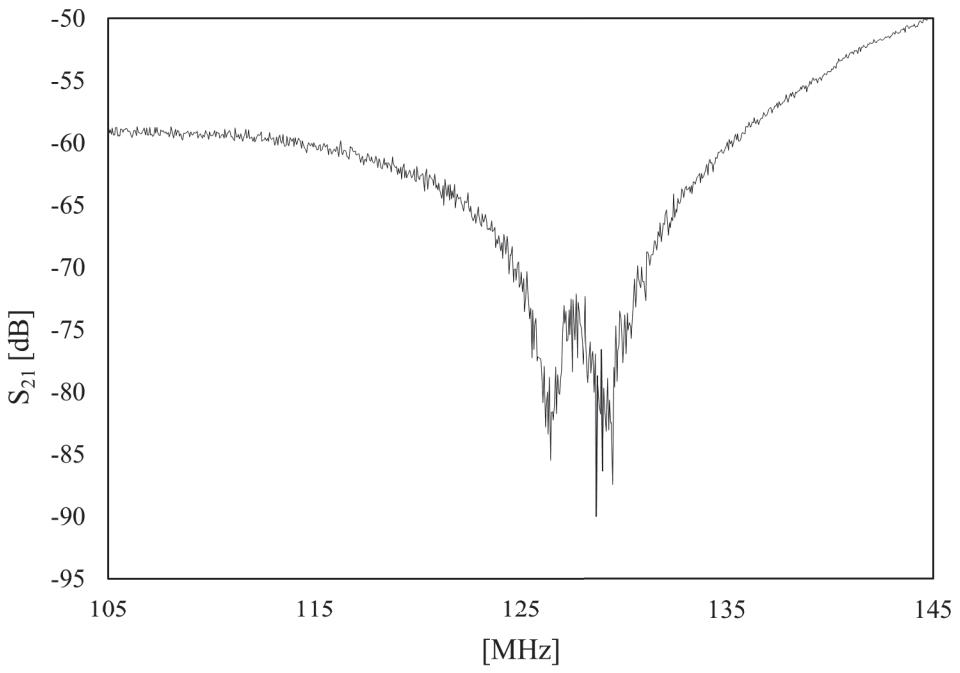

Figure 6.4: Plot showing the resonance of a 4 μm long doubly clamped cantilever from chip 1

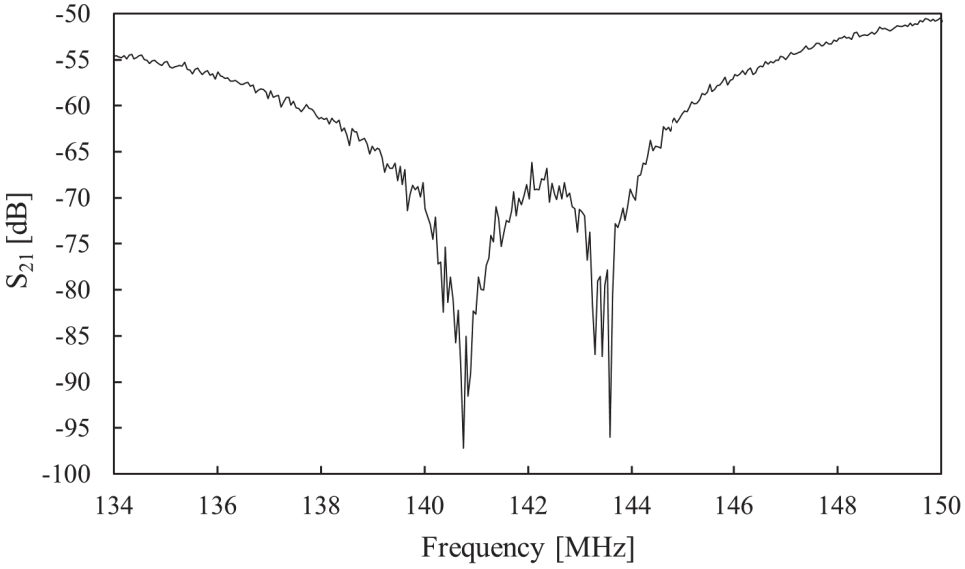

Figure 6.5: Plot showing the resonance of a 5 μm long doubly clamped cantilever from chip 1

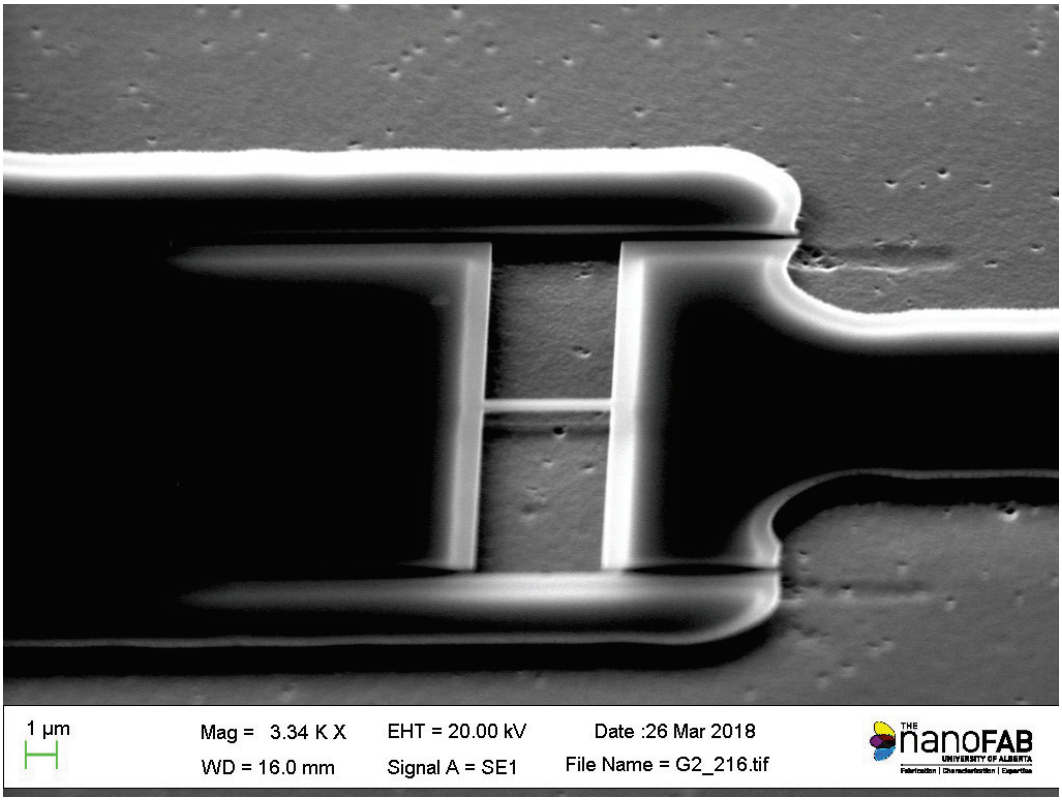

Figure 6.6: SEM image showing a 3.5 μm long doubly clamped cantilever from chip 2

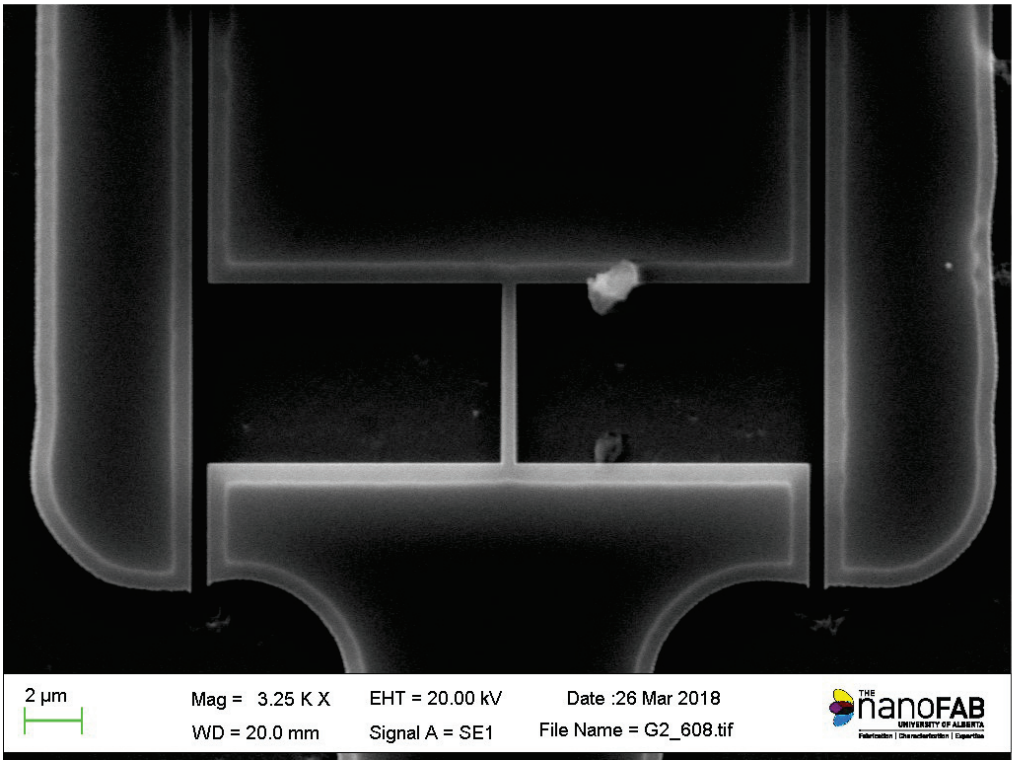

Figure 6.7: SEM image showing a 5.5 μm long doubly clamped cantilever from chip 2

Table 6.1 shows the cumulative results of those devices tested from before the COVID-19 pandemic. For some of the chips, a clear frequency response was measured, however, the device or connection failed before a plot could be obtained.

Chip 1

Length [μm]	Frequency [MHz]	Q	Mode (n)
3.5	126	85.3	1
4	127	96.3	1
4.5	175*	n/a	1
5	143	63.9	2
5.5	143*	n/a*	2

Chip 2

Length [μm]	Frequency [MHz]	Mode (n)
3	173	1
4	94	1
5.5	143	2

Table 6.1: Measured resonances for doubly clamped cantilevers. Parameters denoted by * failed or lost the signal response shortly after testing and quality factor could not be determined. For speed of characterization Chip 2 did not have the quality factor recorded. Only the resonant frequency response was recorded. The most likely resonant mode based on the resonant frequency was included.

6.2.2 "U" Shaped Cantilevers

Table 6.2 shows the cumulative results of the "U"-shaped cantilevers. Although a clear resonant response was measured on a large proportion of devices within a given chip, quality factor varied. Chip 2 was not included in testing as an error during lithography led to no usable devices as the chip was not exposed. As this chip was not processed further from the EBL step, and as no cantilevers were made at this step, it was not counted towards the yield of devices. Again, if a response was found, the frequency peak was observed for several minutes (where possible) to ensure confidence in the response. After searching for any other frequency peaks, the circuit would be re-balanced at the measured response to verify its validity as a data point. Chip A.4 was tested a second time after several days had elapsed to verify the validity of the data. All re-measured points were within 1-2 MHz or less of initial measurements. Quality factors and resonances agreed with other groups performing similar work in the same frequency range [47] [51] [40].

Chip 1

Length [μm]	Frequency [MHz]	Mode (n)
3	100	2
3.5	150	2
4	176	3
4.5	157 / 118	3 / 2
5.5	120	3
6	138	3

Chip 3

Length [μm]	Frequency [MHz]	Q	Mode (n)
3	168	224.5	2
3.5	136	32.3	2
4	203	61.6	3
4.5	170*	n/a	likely outlier

Chip 4

Length [μm]	Frequency [MHz]	Mode (n)
2.5	262	2
3	132	2
3.5	136	2
5	155	3

Table 6.2: Measured resonances for the "U" shaped cantilevers. Chip 2 had a lithography error early in processing and had no resonators to test. As shown in later plots, devices from chip 1 although measurable had poor quality factors. The most likely resonant mode based on the resonant frequency was included.

Although quality factor clearly varied between devices of different lengths even on the same chip, the data collected is still valuable for proving the efficacy of the magnetomotive system used. Fig 6.8 - Fig. 6.12 show the frequency response measured across chips 1 and 3. SEM images from some devices measured after testing are shown in Fig. 6.13 and Fig. 6.14. Upon testing the 4.5 μm long "U" shaped cantilever from chip 1 two different frequency responses were found.

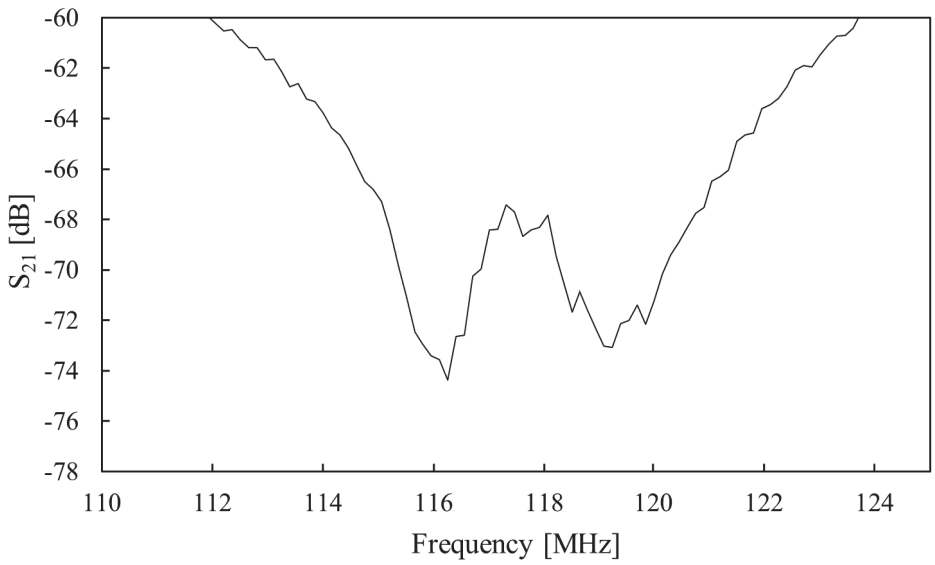

Figure 6.8: Plot showing the resonance of a 4.5 μm long "U" shaped cantilever from chip 1

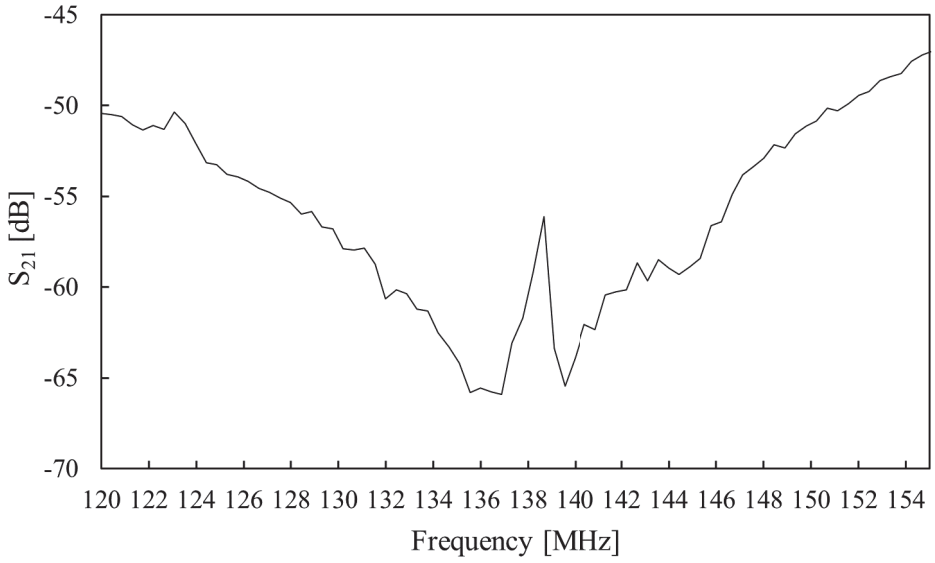

Figure 6.9: Plot showing the resonance of a 6 μm long "U" shaped cantilever from chip 1

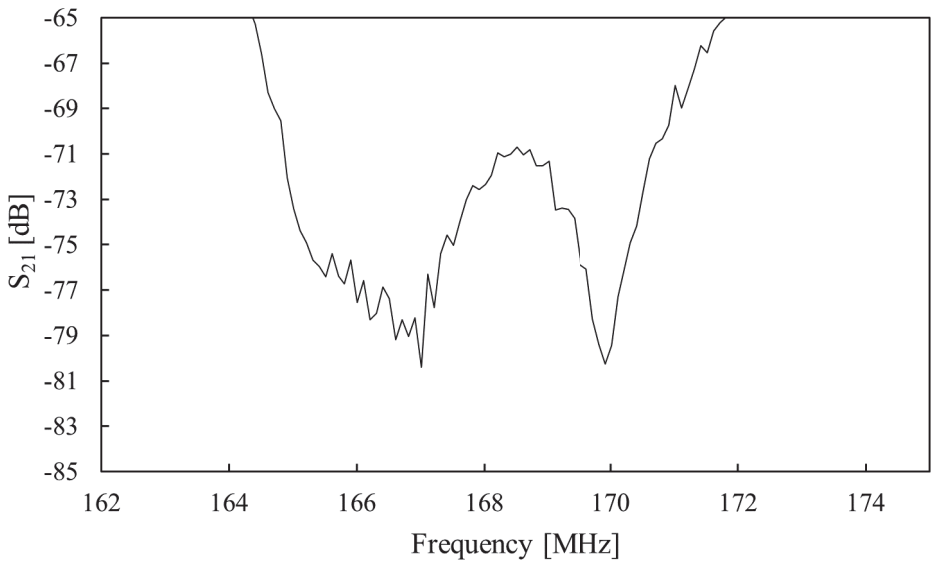

Figure 6.10: Plot showing the resonance of a 3 μm long "U" shaped cantilever from chip 3

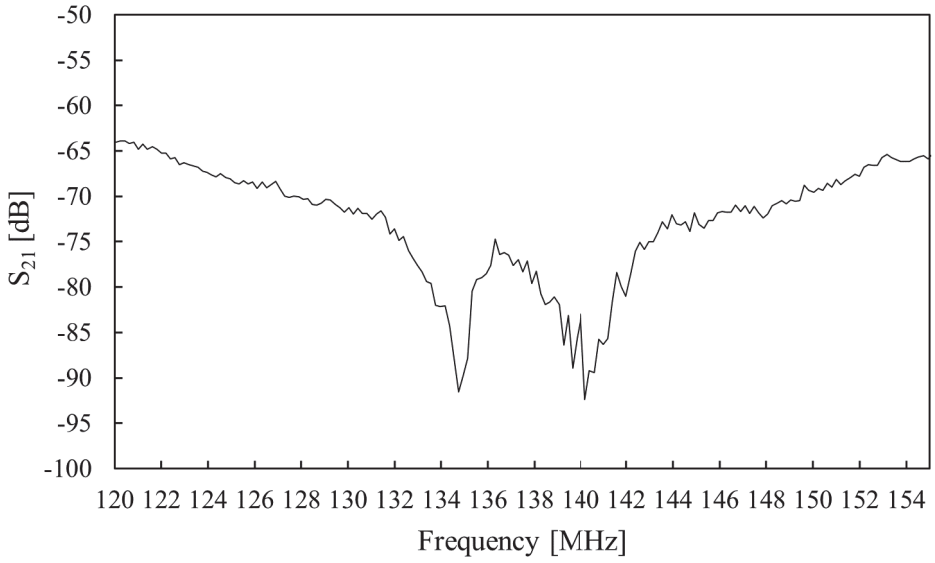

Figure 6.11: Plot showing the resonance of a 3.5 μm long "U" shaped cantilever from chip 3

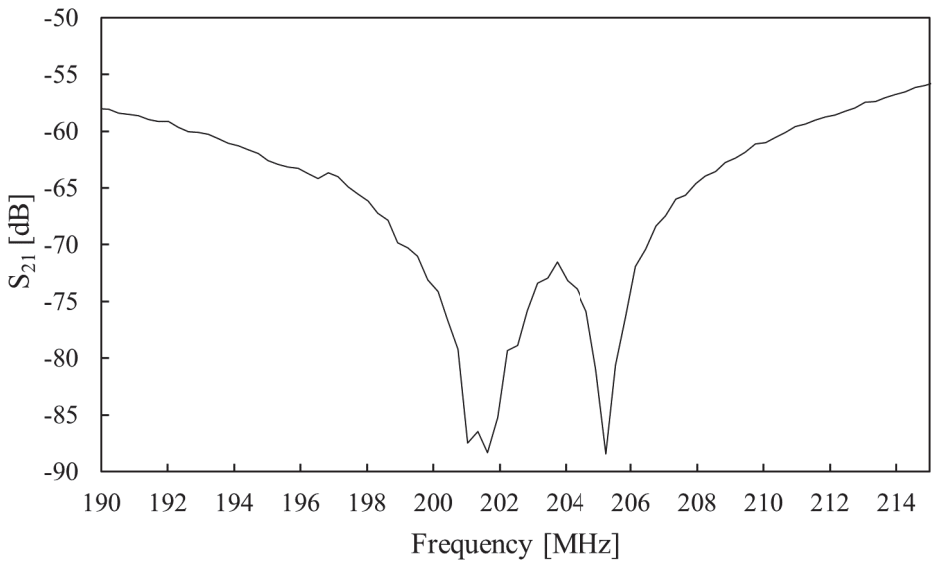

Figure 6.12: Plot showing the resonance of a 4 μm long "U" shaped cantilever from chip 3

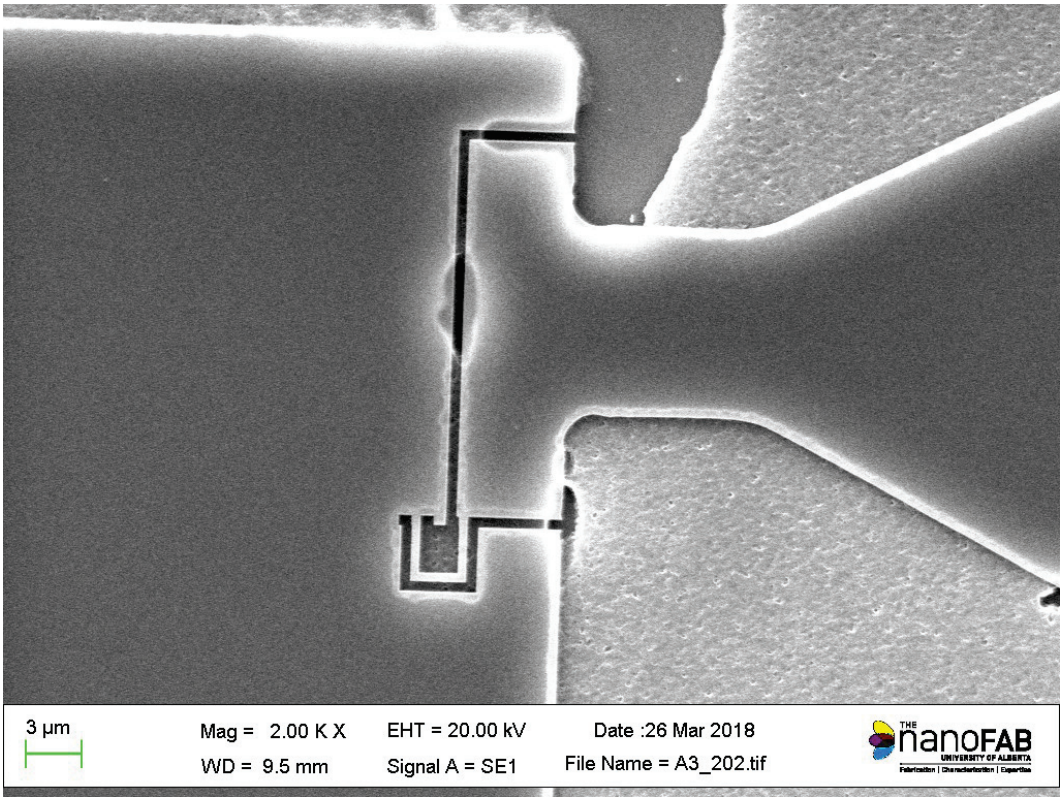

Figure 6.13: SEM image showing a 3 μm long "U" shaped cantilever from chip 3

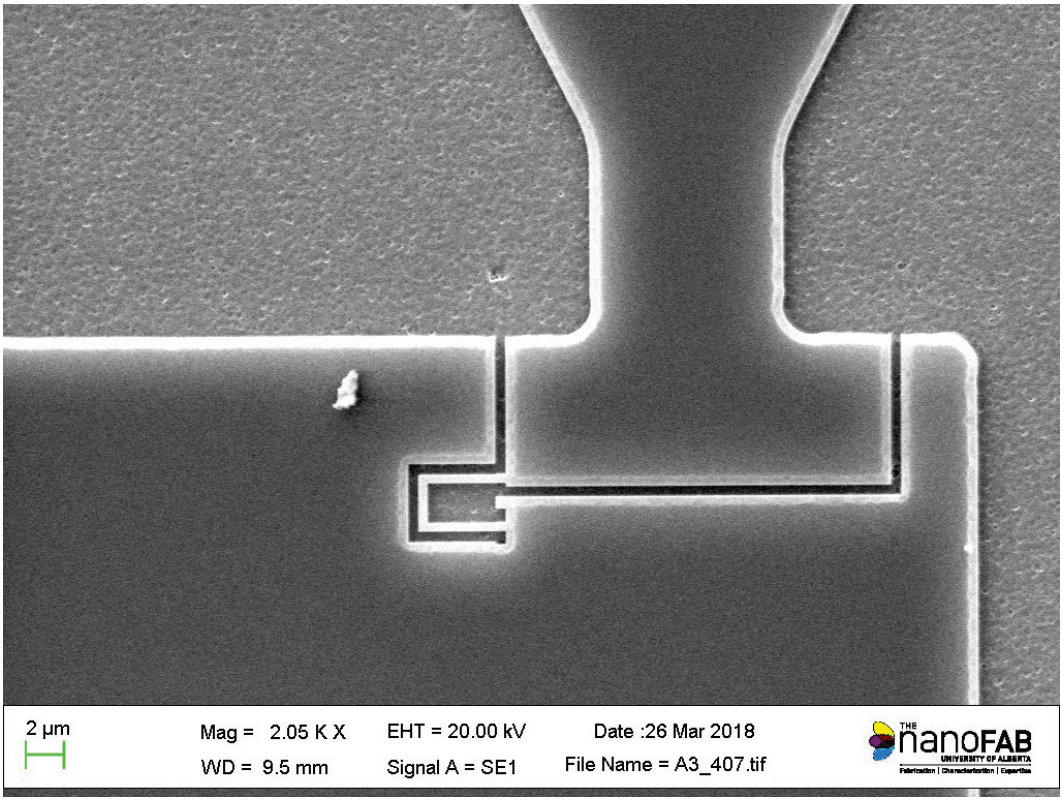

Figure 6.14: Plot showing the resonance of a 4 μm long "U" shaped cantilever from chip 3

6.3 Assumptions and Discussion

When determining the theoretical frequencies for the devices, simplest motion was assumed. However, the shape of the "U" shaped cantilevers will likely have some torsion in their motion as it is statistically more likely that both branches of the "U" shape would not move in unison [47]. Any variance between both branches of the "U" such as length, undercut, film thickness, etc can cause mismatch that could lead to some torsion. This additional movement that counteracts the theoretical assumption will likely lower the quality factor of devices, leading to additional energetic losses.

Determining the theoretical resistances is helpful to a researcher in order to determine a starting point for where to look for the frequency response. However, these calculations rely heavily on the assumption that all values are near to expected. For even a difference in 5 nm of film thickness difference, the

resonant frequency can shift by several percent, significantly increasing error when looking for a response. With a manual balancing circuit, operator skill level and experience has a large impact on the results measured from the tool. It is very likely that a skilled operator would be able to obtain more data with experience compared to an unskilled operator.

The size and shape of the cantilevers has a large effect on their theoretical resonant frequency. Certain parameters, if changed, could cause a drastic shift in the expected resonant frequency. For either shape of cantilevers, if it is assumed an error of up to 10 nm in the deposition thickness, the theoretical resonance plot will be as follows in Fig. 6.15 and Fig. 6.16. Where the dotted line indicates how the resonant frequency will shift with a change in film thickness. It should be noted that the shift in thickness is relatively small, indicating there is more error allowable at this step in the process. This also bodes well for future adaptation of the devices for the deposition of functionalization films (such as GLAD). Adding to the thickness has less effect on device behaviour when compared to other properties.

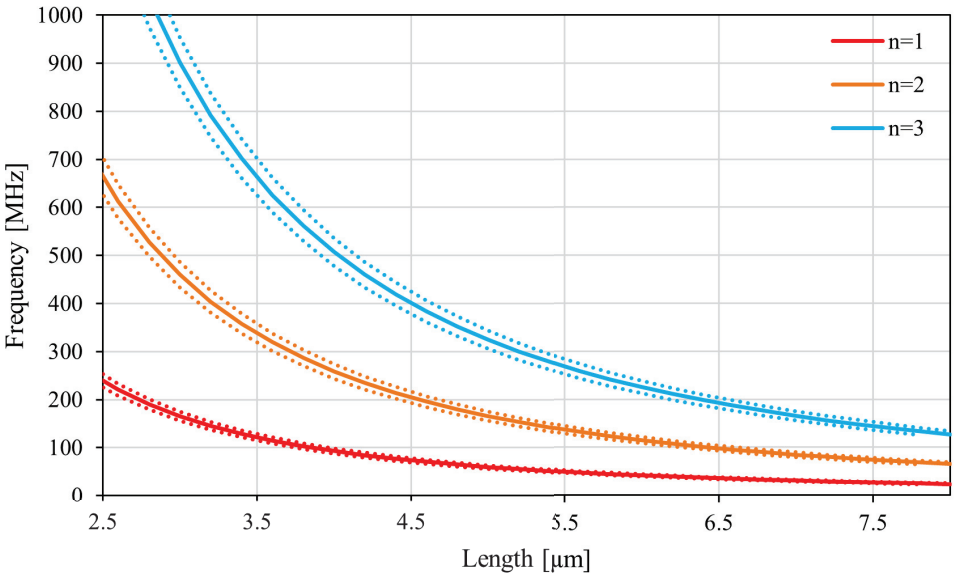

Figure 6.15: Thickness variance of 10 nm in the theoretical frequency of the doubly clamped cantilevers.

It is known that the VHF etch process is largely isotropic: meaning the etch will proceed in all directions at a nearly equal rate. When calculating the

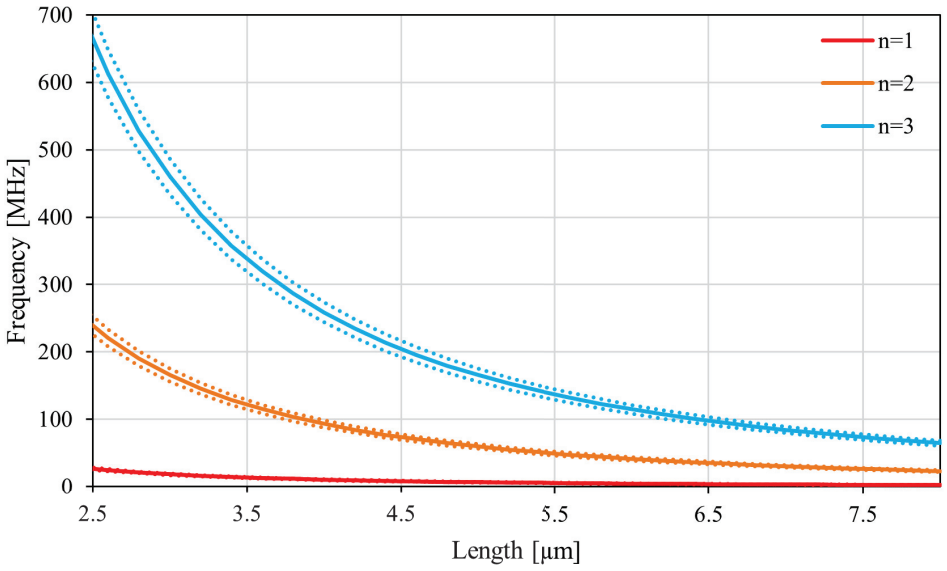

Figure 6.16: Thickness variance of 10 nm in the theoretical frequency of the "U"-shaped cantilevers.

theoretical resonant frequency of the cantilever, the length is key. To release the devices, the BOX was etched to a depth of 500 nm. If it is assumed that the etch is perfectly isotropic, this means that the undercut will also be 500 nm. This would increase the effective length of the resonator. The doubly clamped cantilevers have two anchoring points, this could lead to an effective resonator length increase of 1 μm. However, as the undercut for the "U" shaped cantilevers would be on the same side, the effective length would only increase by a maximum of 500 nm, making this design more robust to etch variance. The shift would be as shown in Fig. 6.17, 6.18, and 6.19.

This potential large shift in theoretical resonant frequency means that although a first point of searching for a resonant response can be approximated by the theoretical calculations, it may not be accurate. As shown in Fig. 6.18 there is overlap between the plots for the n=1, and n=2 modes. This leads to a large margin of error in estimating the exact response for a cantilever. That being said: once fabricated, the effective length thickness or other size parameters will not change. Once the resonance is found, it is more beneficial to measure the overall shift due to added analyte during testing. Calibration is a critical step in sensor use. Once the "null" is established with no analyte, the

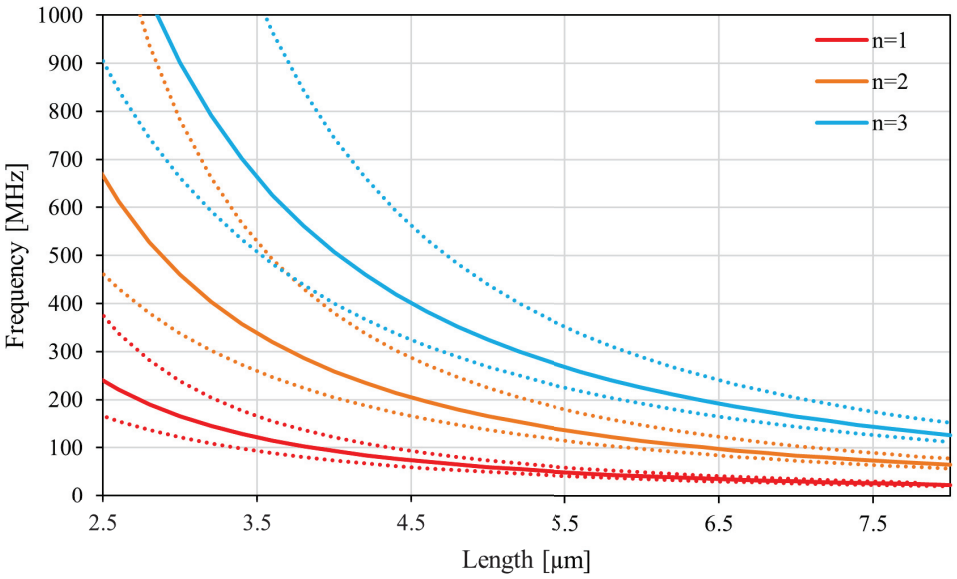

Figure 6.17: Length variance due to undercut of 0.5 μm in the theoretical frequency of the doubly clamped cantilevers.

system should be calibrated. In real time as the frequency shifts in a testing scenario, the shift is the key factor and not the original theoretical resonant frequency.

The purpose of this work was not to perfect these types of cantilevers. Work was done to improve overall yield of the devices, which led to a larger data set available. With more functional devices to test overall the ease-of-use of the low-cost testing assembly was proven. This researcher was able to characterize far more devices than were able to be done previously by the group. If implemented by other groups, they too may be able to increase their overall data sets, for lower costs for testing. Once a reliable process such as this is in place, work can proceed towards testing of different analyte, depending on the desired research outcome.

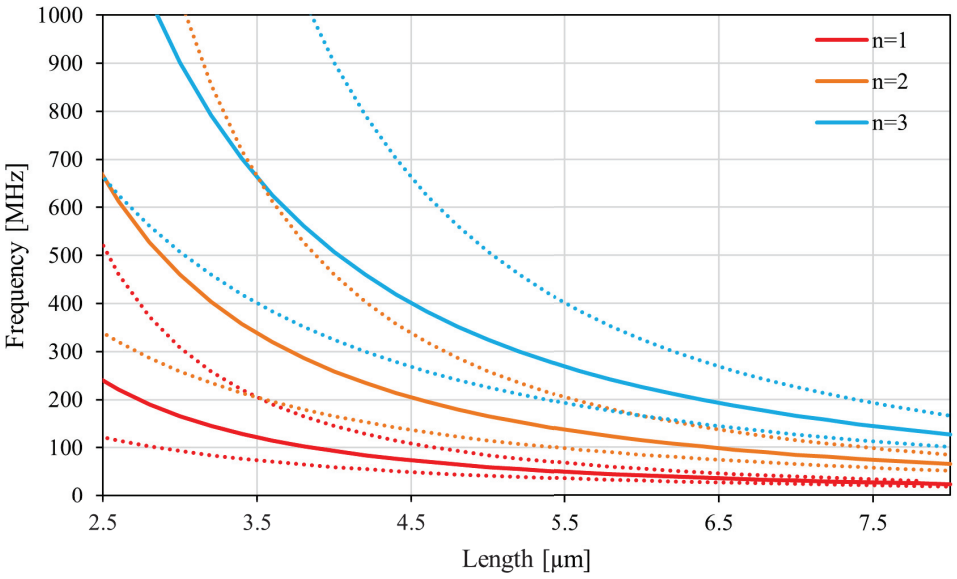

Figure 6.18: Length variance due to undercut of 1 μm in the theoretical frequency of the doubly clamped cantilevers.

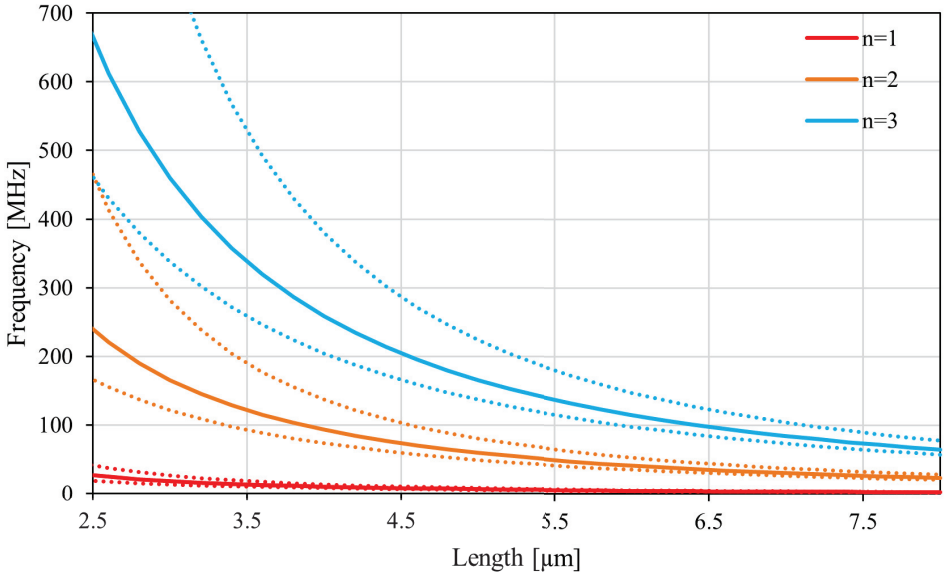

Figure 6.19: Length variance due to undercut of 0.5 μm in the theoretical frequency of the "U" shaped cantilevers.

Chapter 7

Conclusion and Future Works

7.1 Conclusion

The work outlined in this thesis showed the efficacy of the low-cost, easy-to-use magnetomotive apparatus designed by the ENL. This author was able to manufacture and test substantially more chips than done in previous work.

Work done on fine tuning the process flow allowed for substantially higher overall yield of devices. Reducing redundancies in the process flow, and simplification reduces the error or contamination that could be introduced at any given step. The photolithography process was simplified to reduce the unnecessary (for this design) dilution step for better photoresist film thickness uniformity near the edges of the chip. Photomask redesign allowed for more chips to be processed in a given day due to reduced need to clean the mask and optimal chuck movement to access all die on the photomask.

Work done on optimization of VHF recipes led to a recipe that largely reduced contamination on the chip at this step. Stiction and CPD drying errors were eliminated at this point, improving yield. The switch to VHF led to much better control over the etch depth of the BOX layer of the devices. Operator error was reduced in etch depth variance, as it proved relatively simple to add more etch time as needed, with little to no consequence for the final outcome of the product. This more reliable process improved yield and led to less chip loss due to errors at this point in the process compared to previous work. The overall chip yield of the devices was improved substantially from below 50% to having functional devices on 100% of chips.

The efficacy of the low-cost magnetomotive assembly and balancing circuit was shown with resonance responses of the chips within expected values. This work did not intend to "perfect" the design or testing of MEMs cantilever devices. Groups have been pushing the boundaries of the limit of detection for these types of devices for some time now. It is hoped that this work will give a starting point to other researchers hoping to do similar work, and reduce barriers of cost or time. Ease of testing could lead to faster prototyping and fabrication of devices for testing. Once done, a group could focus on functionalization of devices for more specific testing of analyte. Especially in the field of micro- and nano-fabrication, interdisciplinary approaches to work such as this is critical. Not only is work needed in the analysis, and electrical design of a system. But also in the overall fabrication and manufacturing of micro- and nano-scale devices.

It is the hope of this researcher that this work will give a good "head-start" to others working in the field to further the limits of what is possible with sensor technology.

7.2 Future Works

With the efficacy of the low-cost system used in this work established and a clear, repeatable process for fabrication of differently shaped cantilevers, there is still work to be done. With the low-cost system in place, a researcher could focus on the functionalization of the cantilevers themselves, by testing and depositing different materials for a functionalization layer. Once an appropriate functionalization layer is determined for the specific application the researcher desires, they could consider actuation of the device using piezoelectric means or a smaller magnetomotive assembly. This would allow for actuation of the devices on a chip level, which would not require a large system like the one proposed in this work. However, adding complexity to a fabrication process significantly increases development time, and fabrication for a chip. It can be preferable to design and optimize a simpler structure, before integrating to a fully on-chip final product.

7.2.1 Further Functionalization with GLAD

GLAD films are columnar thin films that are porous with low density. By altering standard physical vapour deposition techniques to induce glancing angles of a collimated incident vapour flux on the substrate, GLAD films will be grown due to random nucleation of the film and subsequent atomic self-shadowing from nucleated particles. The fabrication of these films is achieved by tilting the substrate to oblique angles, typically between 60° and 85°. As atoms adsorb to the surface, they will randomly nucleate. The droplet that forms on the surface of the substrate will experience cohesive forces and surface tension. The difference between the adhesive forces wetting the droplet to the substrate and the cohesive forces can cause the droplet to form a rounded shape. Due to the wetting angle of the nucleating film and the shape of the rounded nuclei on the substrate, they will shadow an area behind them, due to the oblique angles during deposition. As the film continues to grow, the impinging atoms will be unable to directly reach the shadowed area and instead will deposit onto the droplets, leading to column growth instead of bulk growth. Some nuclei will seed too close together, and may become shadowed by larger particles, leading to extinction and competitive growth. Once extinguished, the other columns will receive more incoming flux, leading to gradual broadening of the columns in the porous film as the deposition continues. This is demonstrated in the diagrams shown in Fig. 7.1 and Fig. 7.2

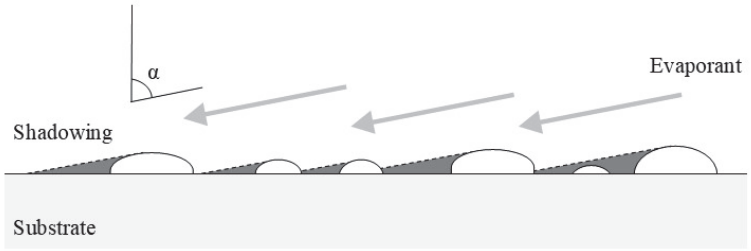

Figure 7.1: A diagram depicting the initial nucleation stage of a GLAD film and the subsequent self-shadowing.

These films will increase the surface area of the sensors considerably. The surface area of 1 g of film can be up to 68 m^2 [52]. The high aspect ratio

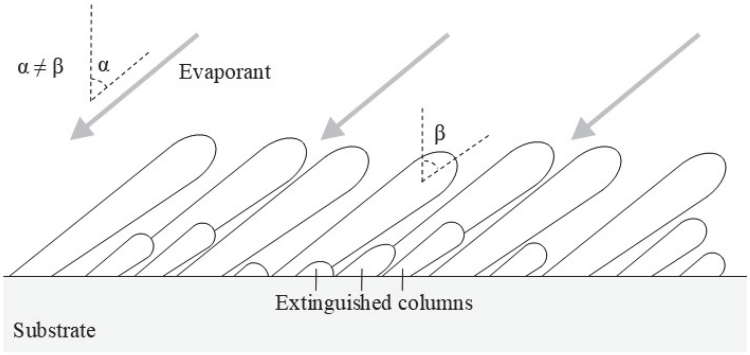

Figure 7.2: A diagram depicting the final structure of a GLAD film.

of these films allow for the functional surface area to be increased, without a significant increase in the mass of the sensor due to their low density. The available surface area increases faster than the added mass when compared to a conventional thin film. In addition, nearly any material that can be deposited using PVD techniques can be grown as a GLAD film [26]. Some exceptions include materials with low melting points, and materials that wet well to the substrate surface due to their low contact angle. As well, adatoms have practical limited mobility on the substrate. An adatom can only move a small distance for their given energy.

Adding GLAD films to increase the surface area of the resonator itself should increase the probability of adsorption onto the surface, improving the detection of these sensors. The researcher conducting this work should make several batches of devices, those with and without GLAD films to compare how they behave in different gaseous environments.

Augmenting sensors using highly porous glancing angle deposition (GLAD) films has been observed in recent published literature. The use of GLAD films to improve the limit of detection of gravimetric magnetomotive actuated cantilever is novel, and practical. In one example, Luo *et al.* [8] used porous GLAD films to yield a system response 3 × larger than dense ZnO thin film for the detection of nitric oxide gas [8]. With the injection of NO into the system from a nitrogen ambient, the resistance of the sensor increased [8]. Another

draw to using porous oxides for sensor functionalization is the reusability of the sensors. In Luo *et al.*, the sensors were able to be reused for the detection of NO gas above 10 ppb, across multiple tests.

In future work, it is hoped to show the efficacy of the addition of GLAD thin films to the surface of resonators in order to improve the sensitivity of these devices. The GLAD film would increase the surface area of the resonator, increasing the probability of analyte molecule adsorption. This could allow for scaling down device size even further and have higher-frequency operation. The higher frequency that a device operates at, and the smaller the device, the greater an effect an adsorbed mass will have, ultimately improving the limit of detection (LOD). Currently, little research exists on the efficacy of adding GLAD films to a resonating NEMS gravimetric sensor.

7.2.2 Statistical Modeling

As shown in Chapter 6, some of the devices worked better than others. Often, the larger length devices failed when compared to the shorter devices. It was also observed that quality factor could vary largely across a given chip. Statistical analysis of which devices worked better based on their lengths would make for a good project. This project would require manufacturing of a large volume of chips and analyzing most common failure modes via electrical analysis and SEM visual analysis. With the reliable process flow for fabrication proposed in this thesis, a researcher could start much father along in the development process, and obtain valuable data more quickly.

7.2.3 Metalization

Some more research could be done on the metallization layer material selection. Different metals will have different thermal stresses and mismatch with the underlying silicon due to the mismatch in the crystal lattice. Stress in the film can lead to deformation of the beam, introducing additional stress, leading to additional noise in the measurement. A current needs to be able to flow through the device, requiring a metal with decent electrical conductivity, but appropriate physical properties as well.

Gold has excellent electrical conductivity, leading to less thermal losses on the chip. Remember that the quality factor of the device is a general factor that accounts for all potential energy losses seen in the final measurement. Gold is fairly resistant to electromigration, however is expensive when prototyping chips. In addition, gold is a fairly soft metal [15]. The probes used were harder brass. The contact pins were spring loaded, to apply some pressure to the chip to ensure good contact for the devices in case of shifting or vibration. However, any time a pin made of harder material is brought into contact with the surface of the softer metal, damage will occur. Retesting of the devices is difficult as damage to the film could render the device potentially unusable in future tests. Gold could be a better option in a packaged chip, complete with permanent metal contacts. Gold is also very corrosion resistant, which may be of benefit for those working in corrosive environments. With the work to deposit GLAD onto the surface, different metalization layers should be explored as potential better alternatives than Al.

7.2.4 Packaging, Scalability, and LOD

Once a device has been fully functionalized and shown to work for the detection of a desired analyte, it needs to be packaged into a system. Packaging in microfabrication is generally the final step of processing. Packaging serves to provide a "finished product". It is desirable to be able to take a fully packaged chip and "plug-it-in" to a larger system for use. One step generally needed is wire bonding to the surface of the contact pads for permanent electrical connections to be able to connect to larger systems. For a chip such as the one shown in this work, one would need to not only include permanent electrical connections but a way to drive the chip. The Halbach array will need to be scaled down substantially for the sensor to be packaged into a system. To compensate for the potentially lower magnetic field, the sensors themselves will require more current to achieve a similar deflection force. The Halbach array is already fairly small (ID 30 mm), and the size chosen was partly to ease operator handling and installation as chips needed to be changed out between testing. A smaller assembly could be made that would be permanent with ease

of handling being less of a concern [44]. The high strength of these magnets will allow for a smaller Halbach array with a strong magnetic field inside for driving of the devices. That being said, practical limits exist for the sizes of the Halbach array to provide the needed magnetic field. The equation for the Lorentz force is shown again below.

$$\vec{F} = q(\vec{E} + \vec{v} \times \vec{B}) \tag{2.2}$$

As discussed in Chapter 1, the smaller the device, the greater of an effect an adsorbed mass will have on the frequency response. Scaling down the resonators will improve the LOD for these devices [7]. However, practical limitations exist as the resonant frequency may fall out of detectable ranges by the systems used. Some groups have shown promise in the use of large arrays of sensors to further reduce the limit of detections. The LOD of some gravimetric sensors has been found to be on the scale of 10^{-19} g. Quality factors range from sub 100, all the way to 1000's [9, 11, 16, 17, 19, 20, 47]. A large number of cantilevers increases the possible surface area. The responses of these devices are then averaged to give a more robust sensor response. Some groups have reported down to a 10 ppb measurement with these large arrays. A concern with these large arrays is reducing the draw power [19, 41].

7.3 Concluding Remarks

With the work demonstrated in this thesis for the optimization of magnetomotive gravimetric MEMs sensors, combined with the low-cost magnetomotive assembly and balancing circuit developed by the ENL, a researcher could more easily enter into functionalization research of these sensors. The work discussed in the future works section to deposit GLAD films on the surface to increase the surface area of the sensors is promising. With GLAD film functionalization completed, one could work on further scaling down the assembly, and/or creating an array of sensors to further reduce the LOD. Once that is done, one could look into packaging the sensors into a finished, useable product. This author looks forward to seeing the developments in the field of magnetomotive

gravimetric MEMs sensors.

References

[1] R. Pandithage, "Brief Introduction to Critical Point Drying," 2012. [Online]. Available: https://www.leica-microsystems.com/science-lab/life-science/brief-introduction-to-critical-point-drying/#:~:text=The%20procedure%20of%20critical%20point,the%20liquid%20to%20gaseous%20state.

[2] B. Finney and M. Jacobs, "Phase Diagram of CO_2 (carbon dioxide). X axis is temperature in kelvin; Y axis is pressure in bar." 2010. [Online]. Available: https://commons.wikimedia.org/wiki/File:Carbon_dioxide_pressure-temperature_phase_diagram.svg#filelinks

[3] H. A. Brausen and J. C. Sit, "A Bridge-Balancing Circuit for Balanced Measurement of Resonant Sensors," *IEEE Transactions on Instrumentation and Measurement*, vol. 69, no. 7, pp. 5002–5009, 2020.

[4] T. J. R. C. Koch, *Photolithography Basics of Microstructuring*, 1st ed., M. GmbH, Ed., Ulm, Germany, 2017.

[5] H. A. Brausen, "A Platform for Nanomaterial-Enhanced Gas Sensing using Magnetomotive MEMS," Master of Science in Microsystems and Nanodevices, University of Alberta, 2016.

[6] S. M. Heinrich and I. Dufour, "Fundamental Theory of Resonant MEMS Devices," *Resonant MEMS: Principles, Modeling, Implementation, and Applications*, pp. 1–28, 2015.

[7] C. P. Goyal, D. Goyal, N. S. Ramgir, M. Navaneethan, Y. Hayakawa, C. Muthamizhchelvan, H. Ikeda, and S. Ponnusamy, "Surface Modifica-

tion of ZnO Nanowires with CuO: A Tool to Realize Highly-Sensitive H2S Sensor," *Physics of the Solid State*, vol. 63, no. 3, pp. 460–467, 2021.

[8] P. Luo, M. Xie, J. Luo, H. Kan, and Q. Wei, "Nitric oxide sensors using nanospiral ZnO thin film deposited by GLAD for application to exhaled human breath," *RSC Advances*, vol. 10, no. 25, pp. 14 877–14 884, 2020.

[9] K. L. Ekinci, Y. T. Yang, X. M. Huang, and M. L. Roukes, "Balanced electronic detection of displacement in nanoelectromechanical systems," *Applied Physics Letters*, vol. 81, no. 12, pp. 2253–2255, 2002.

[10] S. A. Campbell, *Fabrication Engineering at the Micro- and Nanoscale*, 4th ed., A. S. Sedra, Ed. New York, NY: Oxford University Press, 2013.

[11] S. Fanget, S. Hentz, P. Puget, J. Arcamone, M. Matheron, E. Colinet, P. Andreucci, L. Duraffourg, E. Meyers, and M. L. Roukes, "Gas sensors based on gravimetric detection - A review," *Sensors and Actuators, B: Chemical*, vol. 160, no. 1, pp. 804–821, 2011. [Online]. Available: http://dx.doi.org/10.1016/j.snb.2011.08.066

[12] Y. Jin, D. Lee, S. Lee, W. Moon, and S. Jeon, "Gravimetric Analysis of CO 2 Adsorption on Activated Carbon at Various Pressures and Temperatures Using Piezoelectric Microcantilevers," *Analytical Chemistry*, pp. 7194–7197, 2011.

[13] D. E. Presnov, S. G. Kafanov, A. A. Dorofeev, I. V. Bozhev, and A. S. Trifonov, "High Quality Factor Mechanical Resonance in a Silicon Nanowire 1," *Pis'ma v Zhurnal Eksperimental'noi i Teoreticheskoi Fiziki*, vol. 108, no. 7, pp. 492–497, 2018.

[14] J. N. Westwood, "High Surface Area Nanoelectromechanical Systems via the Integration of Glancing Angle Deposition Thin Films," Master of Science in Microsystems and Nanodevices, University of Alberta, 2013.

[15] W. D. J. Callister and D. G. Rethwisch, *Materials Science and Engineering An Introduction*, 8th ed., J. W. . S. Inc., Ed., Hoboken, NJ, 2010.

[16] C.-h. Weng, G. Pillai, S.-s. Li, and S. Member, "A Thin-Film Piezoelectric-on-Silicon MEMS Oscillator for Mass Sensing Applications," *IEEE Sensors Journal*, vol. 20, no. 13, pp. 7001–7009, 2020.

[17] C.-H. Weng, G. Pillai, and S.-S. Li, "A thin-film piezoelectric-on-silicon mems oscillator for mass sensing applications," *IEEE Sensors Journal*, vol. 20, no. 13, pp. 7001–7009, 2020.

[18] I. Bargatin, E. B. Myers, J. Arlett, and E. Al, "Sensitive detection of nanomechanical motion using piezoresistive signal downmixing," *Applied Physics Letters*, vol. 133109, no. February 2005, pp. 1–4, 2007.

[19] N. Delorme, C. Le Blanc, A. Dezzani, M. Bély, A. Ferret, S. Laminette, J. Roudier, and E. Colinet, "A nems-array control ic for subattogram mass sensing applications in 28 nm cmos technology," *IEEE Journal of Solid-State Circuits*, vol. 51, no. 1, pp. 249–258, 2016.

[20] G. Gourlat, M. Sansa, P. Villard, G. Sicard, G. Jourdan, I. Ouerghi, G. Billiot, and S. Hentz, "15.6 a 30-to-80mhz simultaneous dual-mode heterodyne oscillator targeting nems array gravimetric sensing applications with a 300zg mass resolution," in *2017 IEEE International Solid-State Circuits Conference (ISSCC)*, 2017, pp. 266–267.

[21] Y. Fukuta, H. Fujita, and H. Toshiyoshi, "Vapor hydrofluoric acid sacrificial release technique for micro electro mechanical systems using labware," *Japanese Journal of Applied Physics, Part 1: Regular Papers and Short Notes and Review Papers*, vol. 42, no. 6 A, pp. 3690–3694, 2003.

[22] T.-v. Dinh, I.-y. Choi, Y.-s. Son, and J.-c. Kim, "Sensors and Actuators B : Chemical A review on non-dispersive infrared gas sensors : Improvement of sensor detection limit and interference correction," *Sensors & Actuators: B. Chemical*, vol. 231, pp. 529–538, 2016. [Online]. Available: http://dx.doi.org/10.1016/j.snb.2016.03.040

[23] M. S. Hanay, M. L. Roukes, L. Duraffourg, and C. Masselon, "Neutral particle mass spectrometry with nanomechanical systems," *Nature Communications*, pp. 2–6, 2015.

[24] F. Yu, S. Member, J. Wang, P. Xu, and X. Li, "A Tri-Beam Dog-Bone Resonant Sensor With High- Q in Liquid for Disposable Test-Strip Detection of Analyte Droplet," *Journal of Microelectromechanical Systems*, vol. 25, no. 2, pp. 244–251, 2016.

[25] M. M. Hawkeye, M. J. Brett, A. Tg, and M. J. Brett, "Glancing angle deposition : Fabrication , properties , and applications of micro- and nanostructured thin films Glancing angle deposition : Fabrication , properties , and applications of micro- and nanostructured thin films," vol. 1317, no. 2007, 2008.

[26] M. R. Kupsta and M. R. Kupsta, "University of Alberta Advanced Methods for GLAD Thin Films by Master of Science Electrical and Computer Engineering," 2010.

[27] S. Adeeb, "Introduction to Solid Mechanics." Edmonton, AB, Canada: https://engcourses-uofa.ca, 2021, ch. Plane Beam. [Online]. Available: https://engcourses-uofa.ca/books/introduction-to-solid-mechanics/plane-beam-approximations/euler-bernoulli-beam/

[28] T. J. R. C. Koch, "Further Processing of Silicon Wafers: SiO_2, Si_3N_4, Metallization, Epitaxy and Dicing," 2017. [Online]. Available: https://www.microchemicals.com/technical_information/silicon_wafer_sio2_si3n4_metallization_epitaxy_soi.pdf

[29] SOITEC, "Smartcut," 2020. [Online]. Available: https://www.soitec.com/en/products/smart-cut

[30] G. De Oliveira and A. Hryciw, "RAITH 150 II EBL System - NanoFAB SOP," 2021. [Online]. Available: https://confluence.nanofab.ualberta.ca/display/EQ/RAITH150+Two+EBL+System+SOP

[31] B. Cherkawski, "Piranha Cleaning," p. 5, 2022. [Online]. Available: https://confluence.nanofab.ualberta.ca/display/NFCORE/Piranha+Cleaning

[32] Z. Chemicals, "Zep520a-7 technical report," 2016.

[33] S. Bozic, "YES Oven (HMDS 1) An environment designed for success An environment designed for success," pp. 1–2, 2015. [Online]. Available: https://confluence.nanofab.ualberta.ca/display/EQ/YES+-+YES3TA+HMDS+Oven+-+SOP

[34] S. Munro, "Vapour HF Etcher (memsstar Orbis Alpha) nanoFAB SOP," 2017. [Online]. Available: https://confluence.nanofab.ualberta.ca/display/EQ/memsstar+Vapour+HF+Etcher+SOP

[35] J. G. Kaufman, "Properties of Pure Aluminum[1]," p. 0, nov 2018. [Online]. Available: https://doi.org/10.31399/asm.hb.v02a.a0006505

[36] K. S. D. Mary, S. R. Joseph, and R. J. Daniel, "Fabrication of surface micromachined molybdenum cantilever beams for PWM MEMS pressure sensor and issues that affect yield," *Microsystem Technologies*, vol. 25, no. 7, pp. 2535–2545, 2019. [Online]. Available: https://doi.org/10.1007/s00542-019-04388-1

[37] T. J. R. C. Koch, "Wet-Chemical Etching of Silicon and SiO_2," 2017. [Online]. Available: https://www.microchemicals.com/technical_information/silicon_etching.pdf

[38] K. Williams, K. Gupta, and M. Wasilik, "Etch rates for micromachining processing-part ii," *Journal of Microelectromechanical Systems*, vol. 12, no. 6, pp. 761–778, 2003.

[39] I. Transene Company, "Buffered Oxide Etchant (BOE) with Surfactant SDS," 2013. [Online]. Available: https://confluence.nanofab.ualberta.ca/pages/viewpage.action?pageId=7210194

[40] E. Collin, T. Moutonet, J. S. Heron, O. Bourgeois, Y. M. Bunkov, and H. Godfrin, "A tunable hybrid electro-magnetomotive NEMS device for

low temperature physics," *Journal of Low Temperature Physics*, vol. 162, no. 5-6, pp. 653–660, 2011.

[41] M. Moczała, A. Sierakowski, M. Babij, K. Kwoka, R. Dobrowolski, J. Radojewski, T. Piasecki, and T. Gotszalk, "Resolution improvement in electromagnetically actuated wheatstone bridge configuration micromechanical resonators," *Sensors and Actuators A: Physical*, vol. 284, pp. 181–185, 2018. [Online]. Available: https://www.sciencedirect.com/science/article/pii/S0924424718305569

[42] C. I. Scientifique, "EA73C," 2024. [Online]. Available: https://www.caylar.net/fr/ea73c_1015920.html

[43] H. O.-M. LTD, "PC based water cooled electromagnet," 2024. [Online]. Available: https://www.holmarc.com/PC_based_water_cooled_electromagnet.php

[44] e magnets, "Neodymium Halbach Arrays," 2024. [Online]. Available: https://e-magnetsuk.com/product/neodymium-halbach-arrays/

[45] I. M. T. I. (IMT), "Curie Temperatures of Magnets," 2022. [Online]. Available: https://www.imt-inc.com/curie-temperature-of-magnets

[46] S. Magnets, "Maximum Operating Temperature VS. Curie Temperature," 2023. [Online]. Available: https://www.stanfordmagnets.com/maximum-operating-temperature-vs-curie-temperature.html

[47] M. Moczała, M. Babij, W. Majstrzyk, A. Sierakowski, R. Dobrowolski, P. Janus, P. Grabiec, and T. Gotszalk, "Technology of thermally driven and magnetomotively detected mems microbridges," *Sensors and Actuators A: Physical*, vol. 240, pp. 17–22, 2016. [Online]. Available: https://www.sciencedirect.com/science/article/pii/S0924424716300413

[48] R. Coutu, I. Medvedev, and D. Petkie, "Terahertz Photoacoustic Spectroscopy," *Sensors*, pp. 1–12, 2016.

[49] T.-j. Peters and M. Tichem, "Fabrication and characterization of suspended beam structures for SiO 2 photonic MEMS," *Journal of Micromechanics and Microengineering*, vol. 25, no. 10, 2015.

[50] Z. Baghchehsaraei and J. Oberhammer, "Parameter Analysis of Millimeter-Wave Waveguide Switch Based on a MEMS-Recon fi gurable Surface," *IEEE Transactions on Microwave Theory and Techniques*, vol. 61, no. 12, pp. 4396–4406, 2013.

[51] M. Bicer, M. N. Esfahani, A. D. Yalcinkaya, and B. E. Alaca, "A deformation-based approach to tuning of magnetic micromechanical resonators," *Journal of Micromechanics and Microengineering*, vol. 28, no. 10, 2018.

[52] A. Physics, "Porosity engineering in glancing angle deposition thin films," vol. 768, pp. 763–768, 2005.